COSMOLOGICAL ANOMALIES SHED LIGHT ON THE DARK SECTOR

by

Tanvi Karwal

A dissertation submitted to The Johns Hopkins University in conformity with the requirements for the degree of Doctor of Philosophy.

Baltimore, Maryland

June, 2019

Abstract

Little is known about dark energy and dark matter; but their simple descriptions in the ΛCDM model of cosmology fit numerous datasets well. Recently however, tensions have emerged between the results of different datasets, as have certain unexpected results. These anomalies may indicate new physics beyond ΛCDM; a revision of how we describe the dark sector. My work uses cosmological anomalies to explore the dark sector.

My research resolves perhaps the most exciting tension in cosmology, the Hubble tension, with early dark energy (EDE). I developed two physical models for EDE and find that these models not only solve the Hubble tension, but also fit most cosmological datasets well. No other solution to the Hubble tension proposed thus far can do both - fully solve the tension while still fitting early and late-time measurements of the Universe.

The model that succeeds ΛCDM should solve not only the Hubble tension but

also other cosmological tensions such as the S_8 anomaly. My research investigates a decaying dark matter model to address both tensions simultaneously but finds the constraints from late-universe observations too stringent to permit a full resolution.

I am also building a phenomenological tool to model the dark sector in a widely-used cosmological code. This tool, generalised dark matter, is a powerful formalism capable of emulating the effects of a wide variety of dark matter and dark energy models, simplifying placing constraints on different fundamentally-motivated models. The formalism and two immediate applications of it are discussed.

My work also shows that a curious cosmic-ray (CR) measurement likely has an astrophysical explanation rather than one motivated by dark matter. More flux in CR positrons is observed at high energies than expected, indicating new sources for high-energy CR positrons. My work demonstrates that nearby pulsars could source these positrons and it develops a new analysis technique to distinguish dark matter and pulsar sources for CR data.

The aforementioned anomalies and many others have persisted in cosmology for years. It may be time to look beyond the standard model of cosmology for new physics and new descriptions of the dark sector.

ABSTRACT

Readers

Marc Kamionkowski (Primary Advisor)

Adam Riess

Petar Maksimovic

Sabine Stanley

Susan Kassin

Acknowledgments

Science is not accomplished in isolation and I am grateful for the encouragement and guidance I have received from many.

I am infinitely grateful to my advisor Marc Kamionkowski. Your advising is largely responsible for moulding me into the researcher I am today. Hopefully, we can agree that that is a compliment. Thank you for being kind and understanding, even when you have to remind me how old the Earth is. Besides striving to be as brilliant as you, I also aspire to be as unperturbed as you. I am extremely grateful for your support, presenting me with every opportunity for growth and of course, your endless anecdotes. I hope to return as a collaborator someday.

My closest collaborators Tristan Smith, Vivian Poulin and 'academic uncle' Ilias Cholis, I have learnt more from you than you tried to teach me. Thank you for trusting my scientific judgement as well as pointing out its fallacies. We have accomplished some spectacular science together and I look forward to more science to come.

ACKNOWLEDGMENTS

I am grateful also to others who mentored me, whether knowingly or not. Julian Muñoz, Patrick Breysse, Ibou Bah and Kim Boddy, you are magnanimous scientists and I deeply appreciate the time you spent on me when you had no obligation to. Kim, I want to grow up to be you.

Roller-coasters are more fun when you have people to scream with, and I am grateful for the many graduate students I shared this ride with. In particular, Dan Pfeffer, Kim Berghaus and Kirsten Hall, you are my cornerstones. Dan, I rely on you far more than I care to admit, you are a bouncy-castle of support. Kim, thank you for telling me to solve my problems. You have weird approaches to motivational speeches, but they work wonderfully. Kirsten, I found a soul-sister in you and I appreciate your calming and validating words, as well as your love of art and cake. You guys give me the warm-and-fuzzies. On a similar note, thank you Kelley Key for keeping all us graduate students in check and always having zombie-movie recommendations for me. I felt truly taken care of at this department, in large part thanks to you.

I must also thank Naitri Jadeja, mostly because she forced me to by interminably whining, but also because she kept me sane during the many years of graduate school.

Finally, I thank my walking birthplace Anita Karwal, the previous tenant and book-thief Janvi Karwal, and black-belt embarrasser Atul Karwal. You guys make me believe I can do anything.

Dedication

To my loving parents and sister.

I wrote a PhD thesis just to cure your insomnia.

Contents

List of Tables

List of Figures

Chapter 1

Introduction

Elegantly put, cosmology relates to "everything larger than a galaxy and smaller than a nucleus" [1]. While the Universe today is substantially larger than a single galaxy and its evolution is governed by large-scale physics, it was once packed into a very small space, its dynamics governed by particle physics. Hence the study of cosmology probes physics across many scales, allowing us to learn much about physics by studying the Universe. Angles to pursue cosmology include understanding the origin and evolution of the Universe, its composition and the behaviour of its constituents.

The Universe visibly consists of baryons (or normal matter) and radiation (photons, or light). From nuclear physics, among other sources, we know it also consists of neutrinos; very light and fast particles that weakly interact with normal matter and therefore cannot be perceived directly. So far, we have accounted for roughly 5% of the Universe today. Approximately another 25% is dark matter, whose effects are only observed gravitationally.

Galaxies and clusters of galaxies gravitate more strongly than what their baryonic matter can account for [2–4], meaning more matter exists in these objects but is simply not visible or is 'dark' [5, 6]. In the most basic picture, dark matter is something that has mass and is able to cluster, allowing the formation of these galaxies and clusters. Currently, the most successful theory of dark matter assumes it consists of particles with small thermal velocities, dubbed 'cold' dark matter (CDM) [7–9]. The remaining $\sim 70\%$ is even more mysterious. Something is causing the expansion of the Universe to accelerate, as indicated by observations of nearby galaxies [10,11]. The unknown source of this phenomena is called 'dark energy' [12,13]. Dark energy is simply, yet successfully postulated to be a cosmological constant Λ. The energy density of Λ in space remains constant even when space itself expands. So described, these components make up the ΛCDM universe, a universe which very closely resembles our own.

The flat ΛCDM model has become the concordance model of cosmology over the past few decades, successfully explaining numerous data-sets [9, 14–25]. The unknowns dark matter and dark energy (collectively, the dark sector) are very simply described in ΛCDM, with just one free parameter between them. This model is in excellent agreement with complex measurements like that of the cosmic microwave background (CMB), the oldest light in the Universe [16, 25]. It is also separately consistent with late-universe probes like supernova data [20].

Despite its triumphs, the ΛCDM model faces challenges ahead. The past two decades witnessed cosmology transform into a precision science. This enhanced precision has revealed certain inconsistencies of the concordance model. Although consistent with indi-

vidual data-sets, results of ΛCDM fits to different data-sets are discrepant [26]. Tensions arise when comparing the predictions of ΛCDM based on the early and late universes, the most notable of these being the 'Hubble tension' [20, 27–30]. A ΛCDM model when fit to the CMB underpredicts the local expansion rate H_0 today by $> 4\sigma$. Similar, CMB-based predictions of the matter density Ω_m and the amplitude σ_8 of matter fluctuations in linear theory overshoot the locally-measured values [31–36]. These tensions have persisted and worsened over the years, leading to the questions 'do these indicate new physics beyond ΛCDM?' and 'does this new physics reside in the dark sector?'. Cosmology has gone from a precision science to an anomalous science. New measurements may be indicating that ΛCDM is no longer a sufficient description of our Universe. My research will address several of these anomalies in cosmology and expand on the ΛCDM model, searching for new explanations of the dark sector.

This thesis is divided into the following chapters. In the first part, in Chapter 2, I present my research on solutions to the aforementioned Hubble tension. Through extensive work on resolving this tension [37–39], my research uncovered a viable solution in the form of a new cosmological model consistent with most available data. Details of the work conducted and avenues for continuing this work form the first part of this thesis. Next, I investigate a new cosmological model which attempts to simultaneously address the Hubble as well as the S_8 tension [40] through a modification of dark matter. This work is presented in Chapter 3. In Chapter 4, I present a flexible, phenomenological approach to the dark sector, the generalised dark matter framework. In this framework, the dark sector components are approximated as a fluid. The properties of the fluid can be varied to track the

effects of various different dark matter and dark energy candidates that arise from different particle physics, making this approach powerful. Finally, Chapter 5 is dedicated to my work addressing an astrophysical anomaly that may have cosmological implications. An excess of cosmic-ray positrons observed by satellite experiments can be accounted for by various models of dark matter particles annihilating in the Milky Way. However, a simpler explanation exists, relying on objects and physical processes known to exist, unlike interacting dark matter. This chapter delineates an astrophysical explanation for this phenomena, demonstrating that the addition of new physics is likely not the cause of this anomaly.

I begin with the Hubble tension in Chapter 2, which is perhaps the most intriguing tension in cosmology today [29]. The Hubble constant H_0 is the current rate of expansion of the Universe and can be derived by fitting a cosmological model like ΛCDM to observations of the CMB [25]. It can also be measured directly in the local universe. This is done by observing the redshift and apparent luminosity of objects of known luminosities, which allow determination of their velocities and distances respectively and hence the expansion rate [41]. This leads to a value $> 4\sigma$ higher than the ΛCDM prediction. Explanations that rely on unexplored systematics have not solved this tension [42–46], leading theorists to postulate solutions that rely on new physics [37, 39, 47, 48].

Initially, I approached this problem phenomenologically in Ref. [37] by adding a dark-energy-like component in the early universe. Theoretical arguments can be made about where in time a modification to cosmology would lead to a solution to the Hubble tension. I, however, expanded my search beyond these regions in redshift. I adopted a data-driven, phenomenological approach in order to simultaneously expose the regions of redshift that

were relevant to the problem, as well as test these arguments. Moreover, constraints placed on fundamentally-motivated models of dark energy and dark matter are specific to the particular theoretical model in question. On the other hand, multiple fundamental models can fit into phenomenological constraints, making this approach more powerful.

While the success of the EDE solution to the Hubble tension is discussed in more detail in Chapter 2, a quick explanation is as follows. The CMB is a smooth emission of microwaves at ~ 2.7K with small variations of order 10^{-5}. These variations correspond to regions of over and under densities in the early universe and are observed to have a preferential size of $r_s \sim 1^\circ$ on the sky [49]. This preferential scale was smaller when the CMB was emitted by the very young universe, but magnified to the 1° scale observed due to the expansion of the Universe, related to H_0. The EDE model increases the early universe expansion rate before the CMB was emitted. This, through complicated physical processes, decreases r_s when the CMB was emitted. However, this smaller r_s still needs to be magnified through expansion into the observed 1° size. The extra magnification required comes from an increase in H_0, easing the Hubble tension.

My work [37] showed that adding early dark energy (EDE) to the Universe at the background level was capable of alleviating the Hubble tension. This leads to the question, 'how do the perturbations of such an EDE affect observables?'. The terms 'background' and 'perturbations' in this context can be understood as follows. The density and velocity of all components of a ΛCDM universe differ over space and time. The variation of their spatially-averaged properties over time is their background evolution. Perturbations here simply refer to the variation of these properties over space and time relative to a smooth

background evolution, for example galaxies start out as spatial perturbation (primarily) of CDM and baryons. Similarly, the EDE will also develop perturbations in time and space dictated by its underlying physical model. Therefore, to answer this next question, a physical model for EDE which would lead to similar effect as in Ref. [37] was conceived in Ref. [38]. After a thorough investigation of this physical model, I tested its viability as a solution for the Hubble tension in Ref. [39] and found that it not only resolved the Hubble tension, but also provided a good fit to most cosmological observables. No other solution to the Hubble tension proposed thus far can do both - fully solve the tension while still providing a good fit to early and late time measurements of the Universe.

Ideally, the model that succeeds ΛCDM will not only address the Hubble tension, but also explain other cosmological anomalies. Therefore, I next searched for new physics in the dark sector that addresses both the Hubble as well as the σ_8 tensions in Chapter 3. One such solution invokes dark matter which decays into dark radiation [40]. The background evolution of decaying dark matter (DDM) is such that it is directly correlated with the Hubble parameter H_0 and inversely correlated with the matter density Ω_m. Hence, an increase in the effective rate of decay of dark matter leads to an increase in the predicted value of H_0 as well as a decrease in Ω_m, diminishing both tensions simultaneously. This work also adopted a phenomenological approach, modelling the effect on observables of decaying dark matter (DDM), but not the full details of the particle physics behind the decay. Chapter 3 presents my work with DDM, which, like many other proposed solutions to these tensions, finds that cosmological data places stringent constraints on these models, keeping them from fully resolving the Hubble tension.

Another cosmological anomaly is a tension at large angular scales in the CMB temperature autocorrelation (TT) spectrum. The ΛCDM model predicts more power at these scales in the spectrum, that is, more variation in the CMB temperature at those scales than observed by two experiments [50–52]. Moreover, the ΛCDM model is too rigid in its descriptions of dark energy and dark matter, as are most fundamentally-motivated cosmological models. Exploring each new fundamental model with cosmological data places constraints on only that particular description of the dark sector. I am hence building the generalised dark matter (GDM) formalism [53] in the widely-used cosmological code CLASS [54]. GDM is a flexible approach to dark matter and dark energy. It permits their properties to vary over time and can capture the effects of most dark matter and dark energy candidates [53], including the standard descriptions CDM and Λ. This flexibility is vital as cosmologists remain unsure about the natures of both dark matter and dark energy. This powerful tool I am developing will simplify expanding on the current standard cosmological model and allow us to investigate the properties of the dark sector in model-independent ways. The GDM formalism and its applications are presented in Chapter 4.

While the previous chapters explore new physics in the dark sector, new physics is not necessitated by all cosmological anomalies. Some may have explanations that reside in unexplored astrophysics masquerading as new physics. My research demonstrates this is likely the case with the cosmic-ray positron excess observed by a number of experiments [55, 56] in Chapter 5. More flux of high energy ($\gtrsim$ 1GeV) cosmic-ray positrons (e^+s) was detected than expected by conventional astrophysical models. These models predict e^+ flux assuming e^+s at higher energies are produced by spallation of heavier cosmic rays (CRs)

colliding with gas in the inter stellar medium (ISM). As such CRs are not produced at the source, they are called 'secondaries'. The excess of CR positrons observed is exciting because it indicated new sources for CRs, unaccounted for by the conventional models.

Numerous theorists have proposed new models of dark matter annihilating into normal matter particles as solutions to this excess [57–60]. However, a simpler solution exists which invokes no new physics [61, 62]. Galactic pulsars are capable of trapping and accelerating positrons to the energies the CR e^+ excess is observed at [63–66]. The difficulty in proving that the source of the excess is indeed pulsars is the great uncertainty in the astrophysics surrounding this explanation. Lacking a complete survey of pulsars in the galaxy, we do not know the locations, luminosities, ages, etc. of all pulsars that could contribute CRs. The exact physics governing the injection of CRs into the ISM by these pulsars is not fully understood either. Finally, a thorough understanding of the diffusion of CRs through the galaxy is important to the problem, as CRs undergo rapid energy losses as they travel from the source to us.

My approach to this problem was to simply span the full range of uncertainties in the astrophysical assumptions, producing multiple expected CR e^+ energy spectra for each combination of assumptions [61]. These could then be directly compared to the data to see whether CRs expected from pulsars could account for the e^+ excess. Overcoming the hurdle of uncertain astrophysics, I turned to the question of distinguishing a CR positron spectrum produced by pulsars from that produced by dark-matter sources. At high energies, the number of pulsars that can contribute CR positrons drops to a few. This results in spectral features in the e^+ energy spectra related to the individual contributing pulsars. Such

spectral features would be absent if annihilating dark matter sourced these positrons. My research developed a new technique for analysing CR data, which quantifies the existence of such features in CR energy spectra, differentiating pulsar and dark-matter sources [61].

Finally, I investigate what insight into the astrophysical uncertainties can be gained using CRs in Ref. [62]. By testing numerous combinations of astrophysical assumptions against CR data, from the goodness-of-fit of each combination, certain assumptions can be discarded or deemed unlikely. Then, if pulsars contribute the bulk of CR positrons at high energies, low energy losses for CRs diffusing through the galaxy are inconsistent. Moreover, rapid decline of pulsar luminosities (parametrised by the braking index κ) is disfavoured. However, pulsars with low braking indices which correspond to such rapid declines have been observed [67–69]. This seemingly incompatible result can instead be interpreted as support for the time-evolution of these braking indices, which has also been observed in some pulsars. To summarise, this anomalous measurement led to research with implications not only for the dark sector, but also for the astrophysics of CRs.

The tensions and curious results discussed above are by no means the only ones in cosmology. Much remains unknown about dark energy and dark matter. My research explores the dark sector through attempts to resolve these cosmological anomalies. I have contributed to solving the Hubble tension and understanding dark energy. My research has also led me to create a framework in a Boltzmann code to test numerous dark sector models. I have also developed a new approach to look for signals in CR data and used this data to gain insight into the astrophysics of pulsars and CRs. Through my research, I aim to make this anomalous age of cosmology a little less anomalous.

Chapter 2

The Hubble Tension

Current measurements of the cosmic microwave background (CMB) are in excellent agreement with the standard ΛCDM cosmological model [9]. Still, there is some tension between the value $H_0 = 67.4 \pm 0.5$ km s^{-1} Mpc^{-1} of the Hubble parameter obtained from the CMB [25] and those obtained from local measurements, $H_0 = 74.03 \pm 1.42$ km s^{-1} Mpc^{-1} (4.4σ tension) as inferred from supernovae and more [41], and $H_0 = 72.5^{+2.1}_{-2.3}$ km s^{-1} Mpc^{-1} as measured by H0LiCOW [70]. This discrepancy is not easily explained by any obvious systematic effect in either measurement [42,43,71,72], and so increasing attention is focusing on the possibility that this "Hubble tension" may be indicating new physics beyond the standard ΛCDM cosmological model [29, 73].

However, theoretical explanations for the Hubble tension are not easy to come by. The biggest challenge remains the very precisely determined angular scale of the acoustic peaks in the CMB power spectrum, which fix the ratio of the sound horizon at decoupling to

the distance to the CMB surface of last scatter. Possible late-time resolutions include a phantom-like dark energy (DE) component [47, 74], a vacuum phase transition [75–77], or interacting DE [78, 79]. However, these resolutions are tightly constrained [20, 30, 74, 79] by late-time observables, especially those from baryon acoustic oscillations (BAO) [17, 80, 81]. Model-independent parametrisations of the late-time expansion history are similarly constrained [27, 48, 82]. An early-time resolution, which reduces the sound horizon with additional radiation energy density [20, 83], is constrained by BAO and by the higher peaks in the CMB power spectrum [27, 79]. It is also possible to address the Hubble tension through a modification of gravity [84–90].

My research has concentrated largely on a recently proposed string-axiverse [91–94] scenario for dark energy [95] as a solution to this persistent and worsening tension [29]. This early-time resolution [37, 96] relies on an exotic early dark energy (EDE) that behaves like a cosmological constant before some critical redshift z_c but whose energy density then dilutes faster than radiation. This addresses the Hubble tension by increasing the early expansion rate while leaving the later evolution of the Universe unchanged.

This chapter is based heavily on Refs. [37–39] [1], papers with coauthors Vivian Poulin, Tristan Smith, Daniel Grin and Marc Kamionkowski.

[1] Ref. [37] was published in Physical Review D © 2016 American Physical Society, Ref. [38] was published in Physical Review D © 2018 American Physical Society and Ref. [39] was published in Physical Review Letters © 2018 American Physical Society.

2.1 Early Dark Energy at the Background Level

As a first step to investigating whether the Hubble tension might be explained by early dark energy (EDE), its impact on just the background evolution of the Universe is explored here. This EDE is of the type that might arise in some axiverse scenarios [95]. In this framework, dark energy is due to an axion-like field that is active today [94, 95]. However, there can be a large number of similar light fields that can be dynamically important at some point in the earlier history of the Universe and then decay away in influence.

Here we surmise that one of these axion-like fields becomes dynamical around the time of recombination, the time of emission of the CMB. More precisely, it behaves, as we will delineate more clearly below, like a cosmological constant at early times. However, at some critical redshift z_c, which is taken to be on order the redshift of recombination, its energy density then decays more rapidly than that of radiation. The cosmological-constant–like behaviour at early times increases the pre-recombination expansion rate and thus reduces the sound horizon at recombination. The resulting reduction in the angle subtended by the CMB acoustic peaks can then be compensated by an increase in the Hubble constant.

Although such an exotic early dark energy is capable of increasing the value of the Hubble parameter today, we find that a value of the optical depth τ to reionisation greater than its Planck-2016 2σ upper bound is required to fully resolve the Hubble tension [2]. We also find that the EDE is constrained to contribute at most $\sim 2\%$ of the total energy density of a ΛCDM universe around the time of recombination, and may only contribute $\gtrsim 5\%$ if

[2] This work was completed in 2016 and uses measurements available then to draw its conclusions. Hence, for this section, $H_0 = 66.93 \pm 0.62$ km s^{-1} Mpc^{-1} is the Planck Hubble measurement [97] and $H_0 = 73.24 \pm 1.74$ km s^{-1} Mpc^{-1} is the local measurement from SH0ES [20].

it decays earlier than a redshift of $\sim 10^5$.

The idea of an additional early-Universe contribution to the energy density has been considered before [98–100]. Although similar in spirit, those models differ from what we consider here. The conclusion reached in our work that EDE contributes no more than $\sim 2\%$ of the critical density around the time of recombination is consistent with the conclusions of earlier papers on other EDE models in which upper limits of $\sim 4-5\%$ were inferred. The increased early-Universe expansion rate considered here also resembles in spirit the explanation suggested in Refs. [20, 27, 100] for the Hubble-parameter tension in terms of an increased number of relativistic degrees of freedom.

In §2.1.1, I describe the EDE model, its evolution and its effect on the temperature auto-correlation power spectrum of the CMB (TT spectrum). In §2.1.2, I describe the Fisher-matrix analysis employed to constrain the model and the data used for this analysis. In §2.1.3, I obtain constraints on the EDE and determine how it changes the Hubble parameter. This is done for the optical depth at reionisation τ fixed at its current best-fit (§2.1.3), 2σ (§2.1.3) and 5σ (§2.1.3) values. Conclusions for this section are in §2.1.4.

2.1.1 Model

The form of the EDE considered here is motivated by the axion-like fields discussed in Ref. [95]. There it was argued that an axion-like field driving accelerated expansion today might be one of ~ 100 such fields in the string axiverse, each of which has some small chance to drive accelerated expansion at some point in the history of the Universe. The scenario suggests that there may be other axion-like fields that may have behaved earlier in

the history of the Universe like a cosmological constant but then decayed away in influence.

This work uses a phenomenological model inspired by Ref. [95]. The energy density $\rho_{\rm ede}$ of the EDE takes the form,

$$\frac{\rho_{\rm ede}(a)}{\rho_c} = \frac{\Omega_{\rm ede}(1+a_c^6)}{a^6+a_c^6}, \tag{2.1}$$

where ρ_c is the critical density today, $\Omega_{\rm ede}$ is the fractional energy density of the EDE today and $a_c = 1/(1+z_c)$ is the critical value of the scale factor at which the EDE shifts from early-time behaviour to late-time behaviour.

The pressure the EDE exerts is

$$p_{\rm ede}(a) = \rho_{\rm ede}\frac{a^6-a_c^6}{a^6+a_c^6}. \tag{2.2}$$

It can be seen that at redshifts $z \gg z_c$, we have $a^6 \ll a_c^6$ and therefore $p_{ede} \simeq -\rho_{ede}$. That is, the EDE behaves like a cosmological constant at early times, similar to a slowly rolling axion field. On the other hand, at redshifts $z \ll z_c$, $a^6 \gg a_c^6$ and $p_{ede} \simeq \rho_{ede}$, emulating a free scalar field, with the hardest possible equation of state allowed by causality.

Fig. 2.1 shows how the energy density of the EDE evolves over cosmic history. Matter, radiation and the cosmological constant are also shown for comparison. Changing $\Omega_{\rm ede}$ shifts the curve of the EDE up or down. Changing z_c changes the redshift at which the EDE switches from behaving like a cosmological constant to decaying away faster than radiation.

It is assumed here that the EDE only changes the homogeneous background evolution

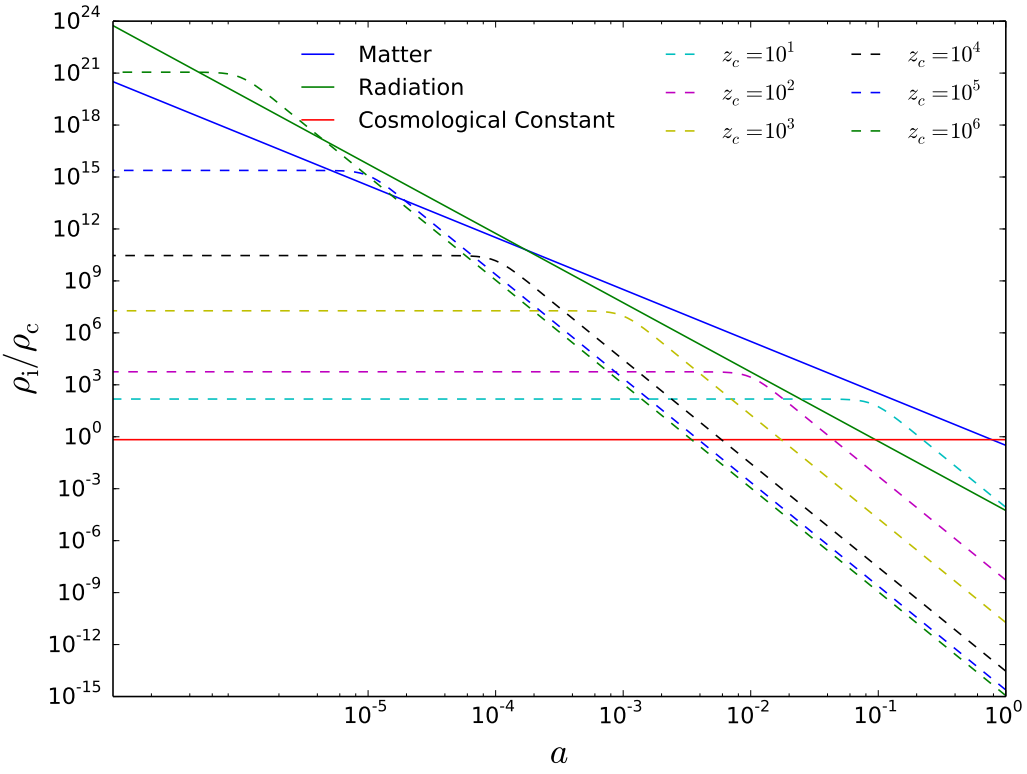

Figure 2.1: The evolutions of the energy densities of EDE (dashed lines) for several critical redshifts z_c, matter (solid blue), radiation (solid green), and the cosmological constant (solid red). For each z_c, $\Omega_{\rm ede}$ is set at its 3σ upper limit derived from the Planck temperature power spectrum assuming τ is fixed to the current Planck best-fit value. The energy densities are all shown relative to the critical density ρ_c today, as a function of the scale factor a.

of the universe. This work did not consider a physical model of how perturbations change as a result of adding this phenomenological model to ΛCDM. Here, the energy density and pressure of the EDE is simply added to the Friedmann equation in the background sector of the public code Cosmic Linear Anisotropy Solving System (CLASS) [54]. Inclusion of scalar-field perturbations can, in some cases, considerably alter the perturbation spectrum [101]. The effects of perturbations in realistic, physical models for EDE are addressed in subsequent work [38].

On adding such an EDE with non-zero $\Omega_{\rm ede}$ to ΛCDM, the predicted TT angular power spectrum will shift. It can be shifted back to better fit the data by shifting the other parameters of the ΛCDM model. The shifts induced by various z_c and $\Omega_{\rm ede}$ on the TT spectrum are shown in Fig. 2.2.

For this analysis, the critical redshift range $10 \leq z_c \leq 10^6$ is explored. Critical redshifts smaller than approximately 500 shift the angular size θ_* of the sound horizon at recombination to larger values for $\Omega_{\rm ede} > 0$. If θ_* were increased in this way, then the current expansion rate H_0 would have to be decreased to shift θ_* back to its measured value. EDEs with $z_c \lesssim 500$ therefore move the Hubble parameter further away from its local value, exacerbating the discrepancy between the Planck and local values. Some such critical redshifts are included in our analysis, limiting the z_c range to 10 on the lower end. On the higher end, the analysis is limited to $z_c \leq 10^6$, as EDEs with higher critical redshifts have little effect on CMB power spectra.

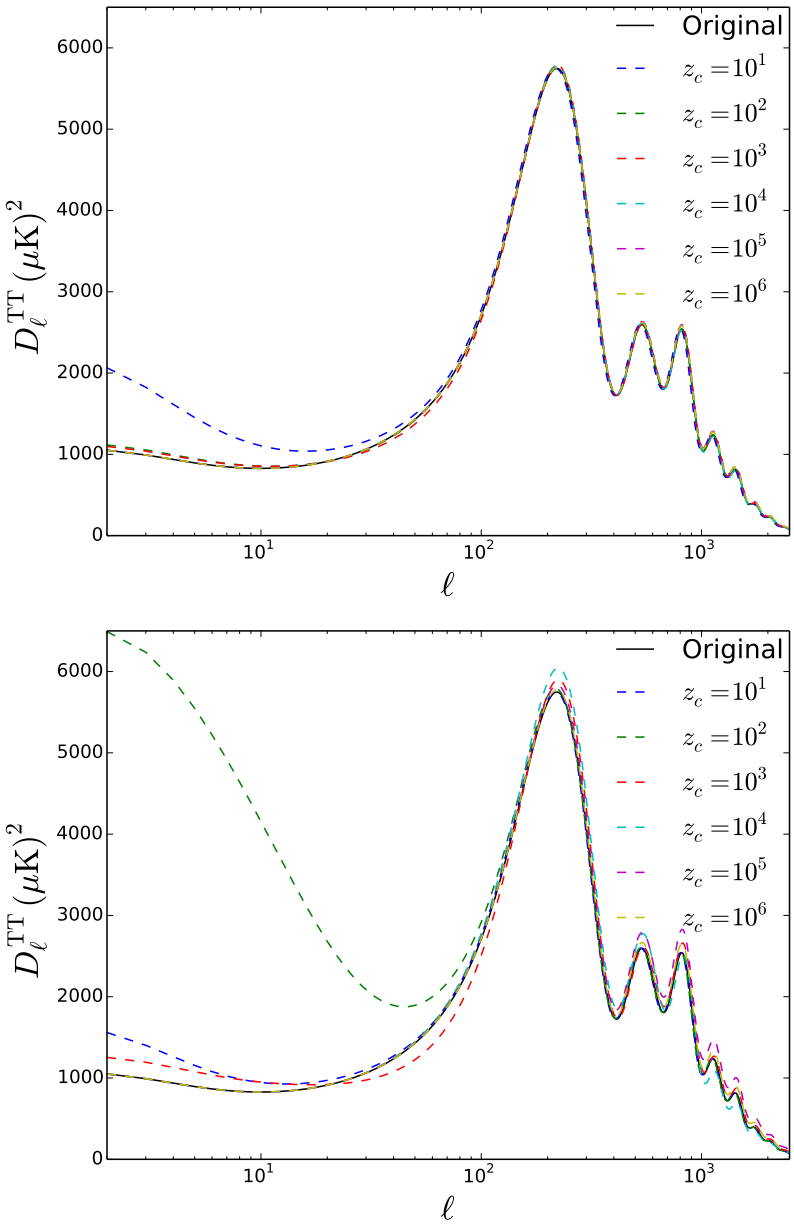

Figure 2.2: The shifts caused in the TT power spectrum due to the addition of EDE are shown for various z_c and $\tau = 0.0596$. The other cosmological parameters are fixed at the values, shown in Table I, that provide the best fit to the TT power spectrum. Clearly the critical redshift of the EDE is important in determining how the EDE shifts the TT spectrum. *Top:* the value of $\Omega_{\rm ede}$ chosen for each z_c is the 3σ upper limit of its best fit. *Bottom:* $\Omega_{\rm ede}$ is chosen such that it moves θ_* by 1%. $\Omega_{\rm ede}$ is approximately two orders of magnitude greater for the lower plot.

2.1.2 Method

My aim here is to determine the largest value of the fractional early dark energy density $\Omega_{\rm ede}$ consistent with Planck measurements of the temperature power spectrum [3], after marginalizing over the other cosmological parameters that are fit to the data. (While doing so, we also investigate whether a nonzero $\Omega_{\rm ede}$ is preferred by the data, but find a null result.) Given the speculative nature of the model, here we do a rough initial analysis, following that outlined in Refs. [102–105], in which the log-likelihood is approximated by a quadratic dependence on the parameters. The loss of precision of this approach, relative to the full Monte Carlo analysis, is made up for by clarity and simplicity. The upper bounds we derive, though, should be understood as approximations rather than precise results.

Given the complexities involved in the current Planck polarization data, only the temperature power spectrum is used here. Since the primary impact of the polarization data (especially that at low multipole moments ℓ) is to fix the reionisation optical depth τ [106], τ is removed from the Fisher analysis and instead fixed to different values that fall within (and, for illustration, also outside) the current Planck error limits. As results show, the best-fit cosmological parameters inferred from the temperature power spectrum are in rough agreement (within 2σ) of those reported by the complete Planck analysis (including polarization). Therefore, it is assumed that the cosmological-parameter shifts inferred below from the introduction of exotic energy reflect reasonably well those that would be obtained from a complete analysis.

[3] Observations obtained with Planck (http://www.esa.int/Planck), an ESA science mission with instruments and contributions directly funded by ESA Member States, NASA, and Canada.

Fisher Matrices

In order to constrain $\Omega_{\rm ede}$ for various z_c's, a Fisher-matrix analysis using the Planck TT angular power spectrum $D_\ell^{\rm TT,obs}$ in a manner similar to that outlined in Ref. [102–105] is conducted. The analysis varies $H_0 = 100h$ km s^{-1} Mpc^{-1}, the fractional density $\omega_{\rm b} = \Omega_{\rm b}h^2$ of baryons today, the fractional density $\omega_{\rm c} = \Omega_{\rm c}h^2$ of cold dark matter today, the amplitude $\ln(10^{10}A_{\rm s})$ of the primordial power spectrum, and the scalar spectral index $n_{\rm s}$. These 5 parameters are henceforth referred to in our Fisher analysis as the "cosmological parameters". Added to these is the current EDE energy density $\Omega_{\rm ede}$ for a given z_c as a sixth parameter in the Fisher analysis.

The residues $R(\ell)$ of the observed and best-fit spectra are parametrised as

$$\begin{aligned} R(\ell) &= D_\ell^{\rm TT,obs} - D_\ell^{\rm TT,best-fit} \\ &= \sum_{i=1}^{N_p} \delta A_i g_i^{\rm TT}(\ell). \end{aligned} \tag{2.3}$$

Here N_p is the total number of parameters A_i, and

$$g_i(\ell) = \frac{\partial D_\ell}{\partial A_i}. \tag{2.4}$$

where the spectrum identifier TT was dropped. The partial derivatives $g_i(\ell)$ of the spectrum with respect to the cosmological parameters were determined by shifting the parameters by 1% about their best-fit values and running the CLASS code to create the TT power

spectrum for each shift. Therefore, $\Delta A_i = 0.01 A_i$ and the derivatives become:

$$g_i(\ell) = \frac{D_\ell(A_i + \Delta A_i) - D_\ell(A_i - \Delta A_i)}{2\Delta A_i}. \tag{2.5}$$

The choice of changing all parameters by 1% is only somewhat arbitrary. This change is small enough that we are still in the linear regime, which validates the Fisher analysis and use of finite differences to numerically differentiate. Moreover, a 1% shift is large enough to ensure that the partial derivatives do not suffer significant numerical errors. These partial derivatives are shown in the top panel of Fig. 2.3.

For the EDE, the partials were determined as

$$g_{\Omega_{\rm ede}}(\ell) = \frac{D_\ell(\Delta\Omega_{\rm ede}) - D_\ell(\Omega_{\rm ede} = 0)}{\Delta\Omega_{\rm ede}}, \tag{2.6}$$

where $\Delta\Omega_{\rm ede}$ is the value of $\Omega_{\rm ede}$ that moved the angular size θ_* of the sound horizon at the redshift of the CMB by 1%. This value was found by recursively running CLASS for each z_c until a $\Delta\Omega_{\rm ede}$ was found that moved θ_* by 1% in either direction. The partial derivatives of $D_\ell^{\rm best-fit}$ with respect to $\Omega_{\rm ede}$ for various z_c's are shown in the bottom panel of Fig. 2.3.

The Fisher matrix F_{ij} is then given by

$$F_{ij} = \langle g_i, g_j \rangle, \tag{2.7}$$

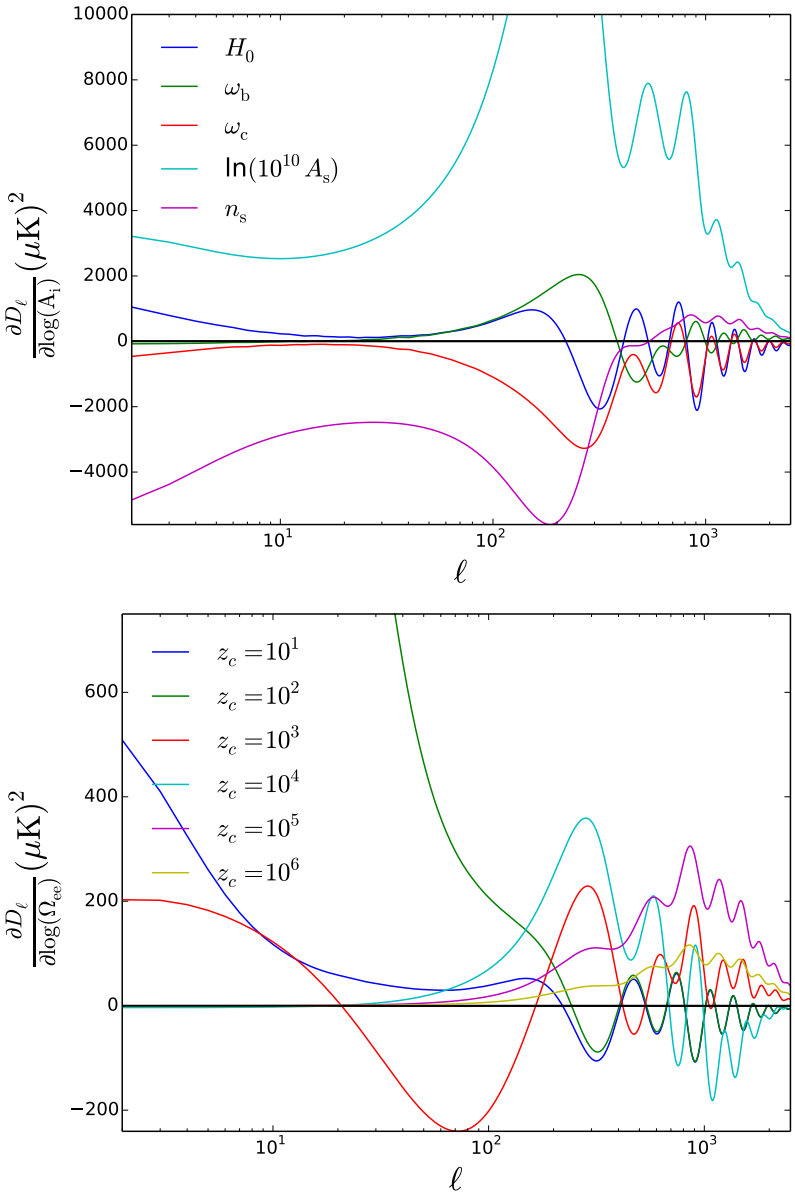

Figure 2.3: *Top:* Partial derivatives of the TT spectrum with respect to the cosmological parameters, H_0 (dark blue), ω_b (green), ω_c (red), $\ln(10^{10} A_s)$ (light blue) and n_s (pink). These were derived at the best-fit values obtained by setting $\tau = \tau_{Pl}$, shown in Table 2.1. *Bottom:* Partial derivatives of the TT spectrum with respect to Ω_{ede} are shown here for various values of z_c. Here, Ω_{ee} is to be interpreted as Ω_{ede} .

where $\langle , \rangle$ denotes the inner product

$$\langle g_i, g_j \rangle \equiv \sum_l \frac{g_i(\ell) g_j(\ell)}{(\sigma_{D_\ell})^2}, \tag{2.8}$$

and σ_{D_ℓ} is the error on $D_\ell^{\rm obs}$. Hence, the analysis is limited by the error on the observed D_ℓ's.

The inverse Fisher matrix is then [107]

$$(F^{-1})_{ij} = r_{ij} \sigma_i \sigma_j, \tag{2.9}$$

where r_{ij} is the correlation coefficient between the parameters A_i and A_j, and σ_i and σ_j are their respective errors.

Planck Data

In their 2016 paper, Planck reports best-fit values for the TT + TE + EE + SIMLow (SimLow is based on low ℓ EE data) spectra combined [97]. To begin with, these values are used for the cosmological parameters and for τ, labelled Planck-16. However, as only the Planck TT power spectrum is used for this analysis, the best-fit values for just the TT spectrum will be shifted from Planck-16 by some small amount. Therefore, first a Fisher analysis is done using just the TT spectrum and the cosmological parameters in order to find this new best fit.

The minimum-variance unbiased estimators are determined as

$$\delta A_i = \sum_j (F^{-1})_{ij} \langle R(\ell), g_j(\ell) \rangle, \tag{2.10}$$

where δA_i quantifies the shift, relative to Planck-16, in the parameter A_i that will fit just the TT data better. Next, it is checked that the shifts in the parameters are all small compared with their 1σ errors and furthermore that the shift in

$$\chi^2 = \sum_\ell \frac{R^2(\ell)}{(\sigma_{D_\ell})^2} = \langle R(\ell), R(\ell) \rangle \tag{2.11}$$

is insignificant. Therefore, it is ensured that

$$\sigma_i \frac{\partial \chi^2}{\partial A_i} = -2\sigma_i \langle R(\ell), g_i(\ell) \rangle \ll 1. \tag{2.12}$$

Doing so, we can now begin the investigation of the effects of EDE with a baseline ΛCDM model that provides the best fit to the TT data used and is consistent, within errors, with the best-fit CMB values obtained from the full Planck-16 analysis. The values adopted for the cosmological parameters + τ for the subsequent analysis are shown in Table 2.1.

As errors on higher D_ℓ's are correlated [108], binned data is used for $\ell \geq 30$. The bin size is 30 for all but the last bin which spans $2490 \leq \ell \leq 2508$. The correlation between errors on D_ℓ's from different bins is then diminished. In all, the range $2 \leq \ell \leq 2508$ is used for the analysis.

	Planck-16	$\tau = \tau_{\rm Pl}$	$\tau = \tau_{\rm Pl} + 2\sigma_{\tau,\rm Pl}$	$\tau = \tau_{\rm Pl} + 5\sigma_{\tau,\rm Pl}$
$100h$	66.93 ± 0.62	67.99749	68.28782	68.77709
$\omega_{\rm b}$	0.02218 ± 0.00015	0.02240	0.02244	0.02251
$\omega_{\rm c}$	0.1205 ± 0.0014	0.11970	0.11906	0.11799
τ	0.0596 ± 0.0089	0.0596	0.0774	0.1041
$ln10^{10}A_{\rm s}$	3.056 ± 0.018	3.05576	3.08972	3.14024
$n_{\rm s}$	0.9619 ± 0.0045	0.96453	0.96599	0.96862
$\chi^2_{\rm red}$	0.9271	0.7652	0.7471	0.7322

Table 2.1: The values of the cosmological parameters and reionisation optical depth τ used as the best-fit values with no EDE are shown alongside the Planck values. Also shown are the reduced χ^2 values for the TT power spectrum for these values.

2.1.3 Constraints on the EDE

Adding the EDE will shift all parameters by some amount, which can be expressed in terms of χ^2 and the errors on the parameters as

$$\delta A_i = -\frac{1}{2}\sum_j r_{ij}\sigma_i\sigma_j\frac{\partial\chi^2}{\partial A_j}. \tag{2.13}$$

The quantity $\sigma_j(\partial\chi^2/\partial A_j)$ is small at the best-fit value for the cosmological parameters and the correlation coefficients are such that $|r_{ij}| \leq 1$. This makes the shift in any parameter δA_i due to any of the cosmological parameters much smaller than the error σ_i on A_i. Therefore, all significant shifts are due to the EDE,

$$\delta A_i \simeq -\frac{1}{2}(F^{-1})_{i,\Omega_{\rm ede}}\frac{\partial\chi^2}{\partial\Omega_{\rm ede}}. \tag{2.14}$$

For the EDE, this shift looks like

$$\delta\Omega_{\rm ede} \simeq -\frac{1}{2}(F^{-1})_{\Omega_{\rm ede},\Omega_{\rm ede}}\frac{\partial\chi^2}{\partial\Omega_{\rm ede}}. \tag{2.15}$$

Therefore, the shift in parameter A_i induced by a change $\Delta\Omega_{\rm ede}$ from its baseline value $\Omega_{\rm ede} = 0$ is

$$\delta A_i(z_c) \simeq \frac{(F^{-1})_{i,\Omega_{\rm ede}}}{(F^{-1})_{\Omega_{\rm ede},\Omega_{\rm ede}}}\delta\Omega_{\rm ede}, \tag{2.16}$$

where δA_i's are now a function of the critical redshift z_c.

Below the following is done for several values of τ: (1) First the values of the five other cosmological parameters that provide the best fit to the TT data we use are determined; (2) $\Omega_{\rm ede}$ is added as a sixth parameter to the Fisher analysis and the following determined (a) the best-fit value of $\Omega_{\rm ede}$; (b) the 1σ error to $\Omega_{\rm ede}$; and (c) the shifts induced by $\Omega_{\rm ede}$ to the cosmological parameters, recording specifically the shift in H_0. Results are a function of $10 \lesssim z_c \lesssim 10^6$. (3) In each case, check whether the introduction of $\Omega_{\rm ede}$ improves the fit to the TT data by a statistically significant amount. In no case is there evidence that the TT data prefers a non-zero value of $\Omega_{\rm ede}$ and thus in each case only upper limits to $\Omega_{\rm ede}$ are derived.

Fixing $\tau = \tau_{\rm Pl}$

First the Planck central value $\tau = 0.0596$ is considered. The constraints to $\Omega_{\rm ede}$ are then shown in Fig. 2.4 as a function of the critical redshift z_c. Also shown there is the 1σ error to $\Omega_{\rm ede}$. The best-fit value of $\Omega_{\rm ede}$ is (unphysically) negative for some z_c, but for no value of z_c does the preferred value depart from the null result by a statistically-significant amount. This remains true for all our constraints on $\Omega_{\rm ede}$ for various values of τ.

For $\tau = 0.0596$, the largest allowable EDE-induced increase in the best-fit value of the

Hubble parameter is 0.22 km s^{-1} Mpc^{-1}, at a critical redshift $z_c \simeq 10000$. This is a small fraction of the Planck 1σ error (roughly 0.6 km s^{-1} Mpc^{-1}) to H_0, so does not do much in the way of relieving the CMB/local-measurement tension. The introduction of $\Omega_{\rm ede}$ to the Fisher analysis increases the error to H_0, to roughly 1.2 km s^{-1} Mpc^{-1}, and this may go some way toward alleviating the tension.

Fixing $\tau = \tau_{\rm Pl} + 2\sigma_{\tau,\rm Pl}$

Next τ is fixed at its Planck-16 2σ upper limit. The TT spectrum prefers a larger value of τ [9]. Therefore, the reduced χ^2 is slightly smaller in this case, and smaller still when we fix τ at its 5σ Planck-16 value, as seen from Table 2.1.

The constraints on $\Omega_{\rm ede}$ are shown in Fig. 2.5. The errors on $\Omega_{\rm ede}$ are essentially the same between the analyses at various values of τ. The blue line in Fig. 2.5 hence offers a visual reference to comparing constrains on $\Omega_{\rm ede}$ for various τ.

The change brought about in the Hubble parameter for $\tau = 0.0774$ is shown in Fig. 2.5. The best-fit value of H_0 increases at most by 0.36 km s^{-1} Mpc^{-1} ($z_c = 1259$), its 1σ value increasing at most by 1.6 km s^{-1} Mpc^{-1} ($z_c = 1585$). The total increase in the Hubble parameter for $\tau = 0.0774$ is twofold. Firstly, the EDE is capable of inducing a greater positive shift in H_0 as compared to $\tau = \tau_{\rm Pl}$. Secondly, for higher τ, a larger best-fit value of H_0 without any EDE is preferred, as can be seen from Table 1. Consequently, although the Hubble tension is not resolved, H_0 is pushed closer to its local measurement.

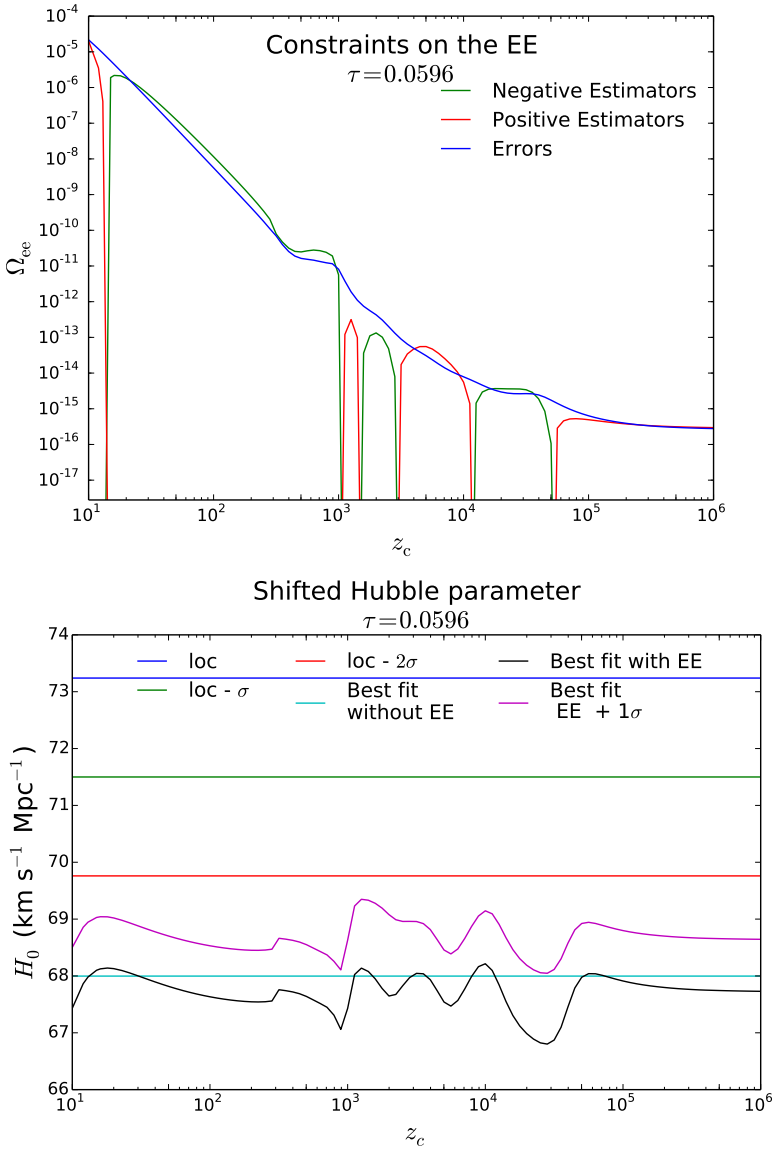

Figure 2.4: *Top:* The best-fit values and errors on $\Omega_{\rm ede}$. The optical depth τ was fixed at the best-fit Planck-16 value to obtain these constrains. *Bottom:* The best-fit values of the Hubble parameter H_0 and its 1σ upper limit obtained by including EDEs in the fit to the Planck temperature power spectrum. Also shown is the central value obtained from local measurements in [20] as well as the values that are 1σ and 2σ lower than the best fit. As before, $\Omega_{\rm ee} = \Omega_{\rm ede}$.

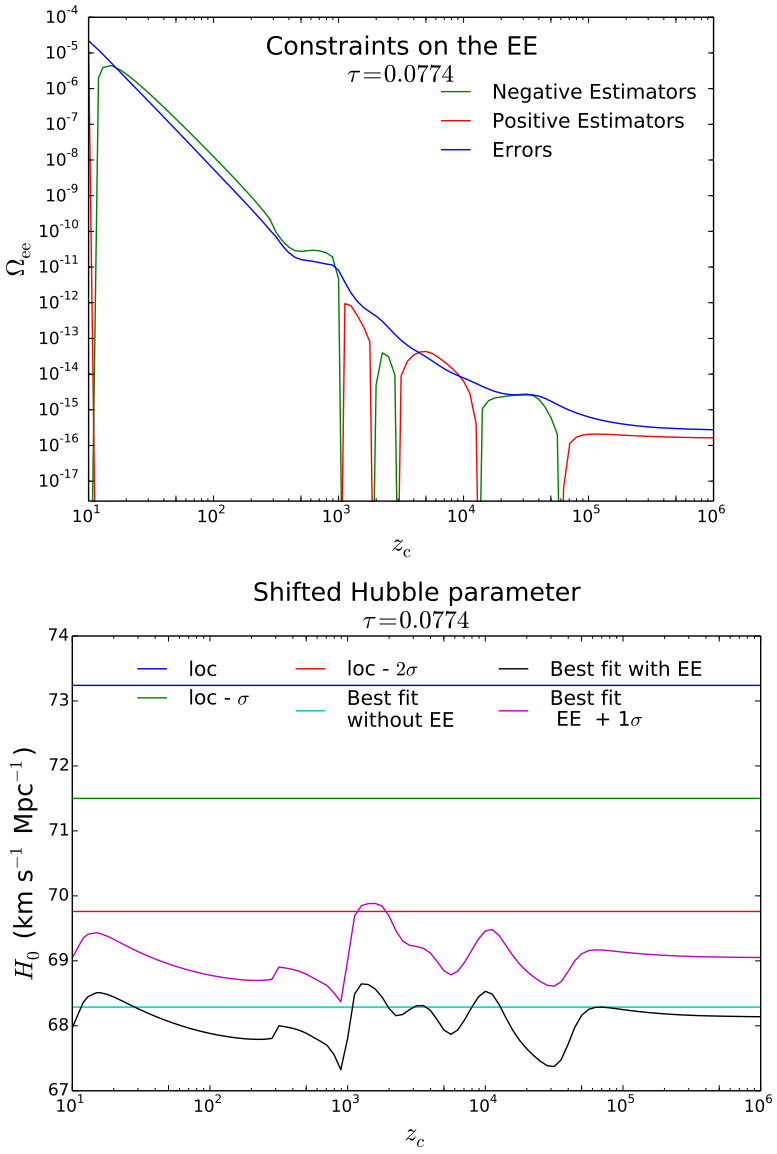

Figure 2.5: *Top:* The best-fit values and errors on $\Omega_{\rm ede}$ are shown for various critical redshifts of the EDE. We fix τ at $\tau_{\rm Pl} + 2\sigma_{\tau,{\rm Pl}}$. As before, $\Omega_{\rm ee} = \Omega_{\rm ede}$. *Bottom:* The best-fit and best-fit + 1σ values for H_0 (in km s^{-1} Mpc^{-1}) are shown along with its local measurement at various σ.

Fixing $\tau = \tau_{\rm Pl} + 5\sigma_{\tau,{\rm Pl}}$

The results from fixing τ at its Planck-16 and 2σ values hint that perhaps a higher value of τ will allow the EDE to fully resolve the Hubble tension. Therefore, this subsection explores what happens if τ for some reason departs by 5σ from its best-fit value. The best-fit values adopted in this subsection are shown in Table 2.1.

The constraints obtained on $\Omega_{\rm ede}$ are shown in Fig. 2.6. The change in the Hubble parameter is shown in Fig. 2.6.

Although fixing τ at 5σ does not entirely eliminate the discrepancy, H_0 is increased by a greater amount as compared to Fig. 2.5. For some z_c, it is increased to within the $2\sigma_{\rm loc}$ range of the locally measured Hubble parameter $H_{0,{\rm loc}}$. The greatest increase in the best-fit value of H_0 is 0.88 km s^{-1} Mpc^{-1} ($z_c = 1585$), in its 1σ value is 2.22 km s^{-1} Mpc^{-1} ($z_c = 1779$).

1σ likelihood ellipses for H_0 and $\Omega_{\rm ede}$ are plot in Fig. 2.7. For local extrema in the shifts in H_0, a higher correlation between H_0 and $\Omega_{\rm ede}$ can be seen in the ellipses. One the other hand, for critical redshifts that leave H_0 unchanged, there is little correlation between H_0 and $\Omega_{\rm ede}$. The Planck-16 values are always within $\sim 2\sigma$ ellipses and all the $\Omega_{\rm ede}$ estimators are consistent with the null result.

2.1.4 Conclusions

This work considers a simple early-dark-energy energy density that provides a small perturbation to standard ΛCDM. The EDE behaves like a cosmological constant until some

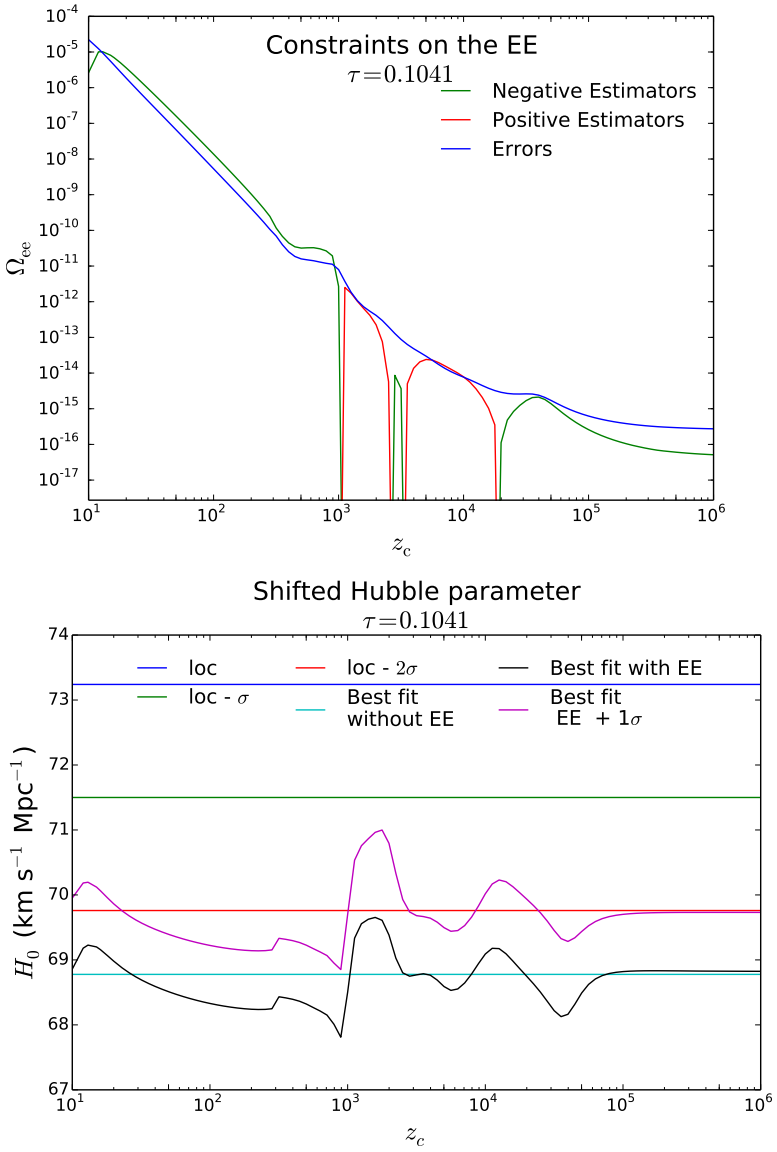

Figure 2.6: *Top:* The best-fit values and errors on $\Omega_{\rm ede}$ ($=\Omega_{\rm ee}$) for various z_c are shown for τ fixed at $\tau_{\rm Pl}+5\sigma_{\tau,{\rm Pl}}$. *Bottom:* The best-fit vales of H_0 (in km s^{-1} Mpc^{-1}) are shown with their 1σ errors. The local measurement is also shown at various σ.

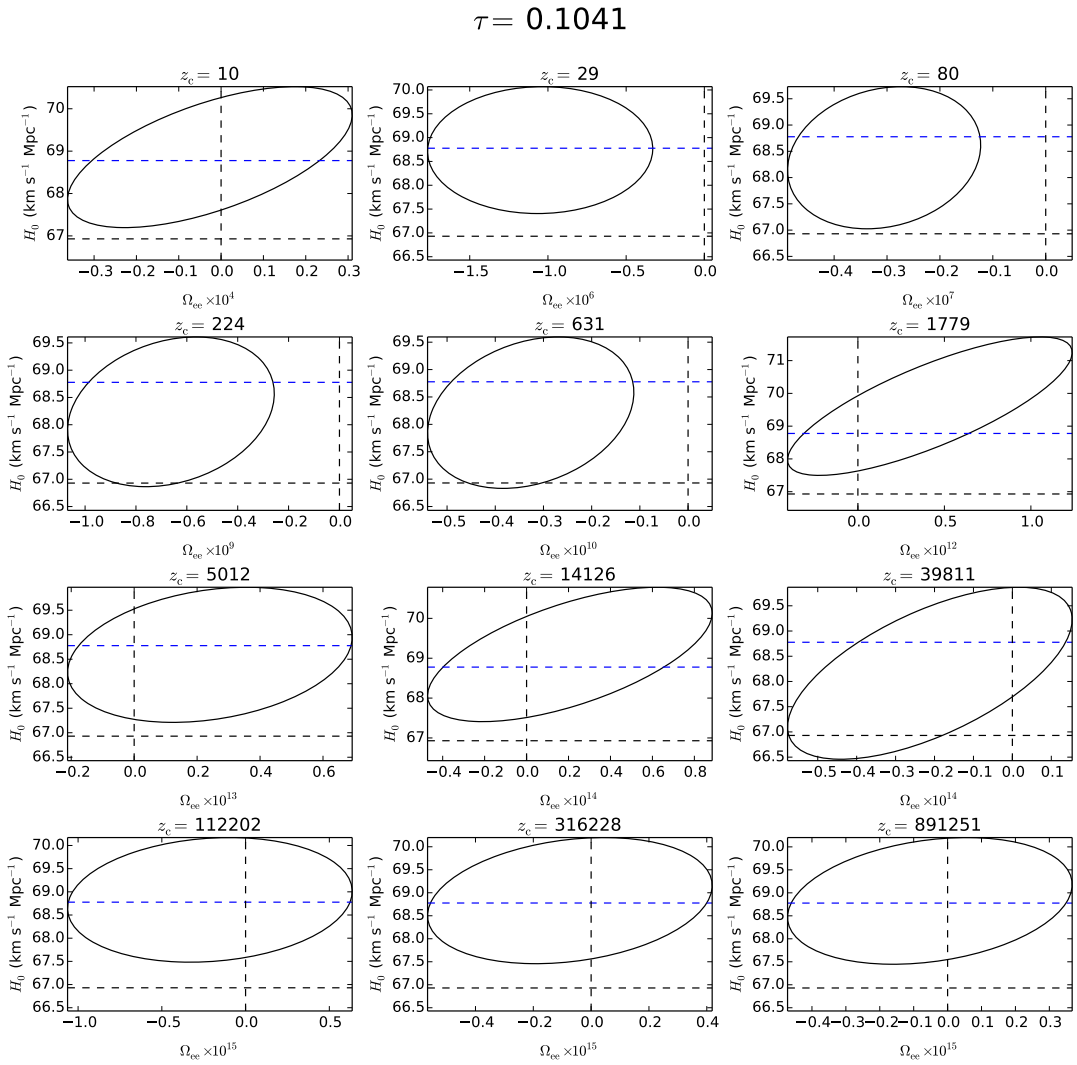

Figure 2.7: 1σ likelihood contours for the Hubble parameter against $\Omega_{\rm ede}$ for various critical redshifts, covering the range of critical redshifts probed. Here, $\tau = \tau_{\rm Pl} + 5\sigma_{\tau,{\rm Pl}}$. In each plot, the Planck-16 values for both parameters are marked by the horizontal and vertical dashed black lines. The dashed blue lines mark the value for the best-fit Hubble parameter for just the TT spectrum without EDEs. Negative values of $\Omega_{\rm ede}$ are unphysical but allowed in the analysis. Estimators of $\Omega_{\rm ede}$ are consistent with zero within $\sim 2\sigma$. As for other plots, interpret $\Omega_{\rm ee}$ as $\Omega_{\rm ede}$.

critical redshift z_c, then decays away as a^{-6}. We investigate whether such an EDE can alleviate the Hubble tension and find constraints on the maximum fractional energy density $\Omega_{\rm ede}$ today, that this field can have by doing a Fisher analysis on the Planck TT power spectrum.

Our analysis finds that the value of τ places a strong constraint on the preferred value of $\Omega_{\rm ede}$ as well as the extent to which it can mitigate the Hubble tension. A larger value of τ leads, with EDE, to a larger best-fit value of H_0.

In order for the best-fit value of H_0 for a ΛCMD + EDE universe to coincide with the local measurement, a value of τ greater than its 5σ Planck-16 value is required. (Such a large value of τ is consistent with that obtained by the WMAP 9-year results, $\tau_{\rm WMAP} = 0.088 \pm 0.014$ [49].) Fixing τ at its Planck-16 best-fit and 2σ values, the tension is not altogether resolved, however, H_0 is shifted up closer to its local value. This is largely due to the error on H_0 increasing on the addition of the EDE. Increasing τ and allowing for such an EDE is indeed capable of alleviating the Hubble tension.

The Hubble tension between local measurements and the Planck data has been studied before by Ref. [20, 27, 36, 47, 85, 109–112]. Altering the effective number of neutrino species $N_{\rm eff}$ [20] and allowing the equation of state parameter of dark energy w to vary with time [36] have been investigated as solutions to the Hubble tension (although variable w may introduce more tensions, eg. with BAO [36]). The correlation between H_0 and $N_{\rm eff}$ as well as that between H_0 and variable w is stronger than that between H_0 and the EDE and they may be better candidates for diminishing the Hubble tension.

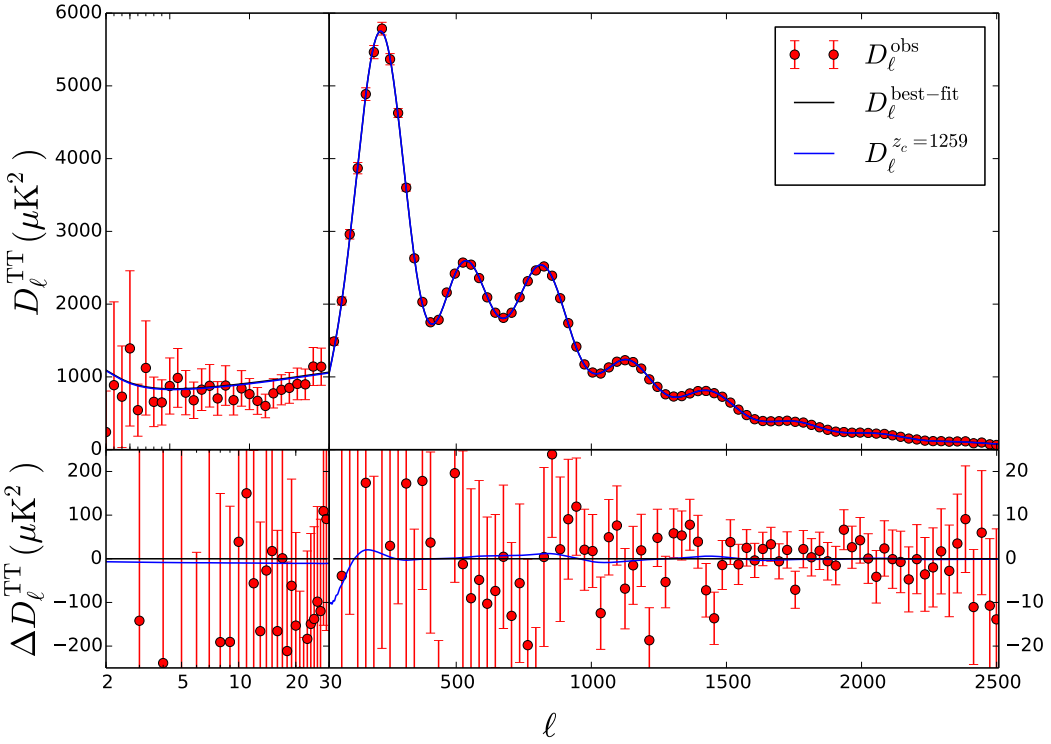

Figure 2.8: The two best fits (blue and black) for the Planck temperature angular power spectrum for $\tau = \tau_{\rm Pl} + 2\sigma_{\tau,{\rm Pl}}$, and the Planck data (red). In black is the best fit without any EDE. In blue is the best fit including an EDE with $z_c = 1259$. This is the EDE that increases the best-fit Hubble parameter the most. In the lower panel, we subtract $D_\ell^{\rm best-fit}$ from all three spectra and plot the residues. The bottom left and bottom right panels are scaled differently such that the residues may be more easily distinguishable.

Furthermore, Ref. [20,42,109] suggest unresolved systematics in Planck data may be the cause of the tension. In particular, Ref. [42] suggests that Planck multipoles $\ell \geq 1000$ may suffer systematic errors. Excluding $\ell \geq 1000$ data not only significantly reduces the Hubble tension, but would also allow more room for early dark energy. However, Ref. [43] finds inconsistencies between high and low multipoles in Planck data statistically insignificant.

Adding the EDE to ΛCDM, the cosmological parameters shift to accommodate the

EDE. The reduced χ^2 for the TT spectrum at their new best fit is not significantly changed. All changes in $\chi^2_{\rm red}$ are approximately an order smaller than the error on it. Fig. 2.8 shows the best-fit spectra without any EDE and that with the EDE which increases the best-fit vale of H_0 the most, for $\tau = 0.0774$. From the residues in the lower panel shown therein, it can be seen that the addition of the EDE leaves the TT spectrum, and hence the reduced χ^2s, largely unaltered. Therefore, current data does not favour with statistical significance the addition of the EDE to ΛCDM.

This EDE was motivated from axion-like fields that may explain dark energy [95]. The EDE considered here contributes its most to the total energy density of the Universe close to its critical redshift, forming its greatest fraction of the total energy density of the Universe. Fig. 2.9 plots this fraction $\eta = \rho_{\rm ede}(z_c)/\rho_{\Lambda{\rm CDM}}(z_c)$ of the total energy density of a pure ΛCDM universe that EDE can from, as a function of redshift, according to our constraints on $\Omega_{\rm ede}$. For extremely high redshifts, the TT spectrum allows dark energy to have a larger energy density than that in a ΛCDM universe as long as it quickly redshifts away. This can also be seen from Fig. 2.1, where the EDE with the greatest critical redshift has a higher energy density than radiation just before it decays. Closer to recombination, the greatest contribution of early dark energy is constraint to be $\lesssim 2\%$ of the total energy density in a ΛCDM universe. This result is consistent with constraints on other early dark energy models obtained through Monte Carlo analyses [98–100] that found upper limits of 4-5%.

The constraints presented here on $\Omega_{\rm ede}$ can be improved by more computationally heavy approaches such as including polarization data in the analysis or by doing a full MCMC on the 6-dimensional parameter space for each z_c considered. However, our simpler approach

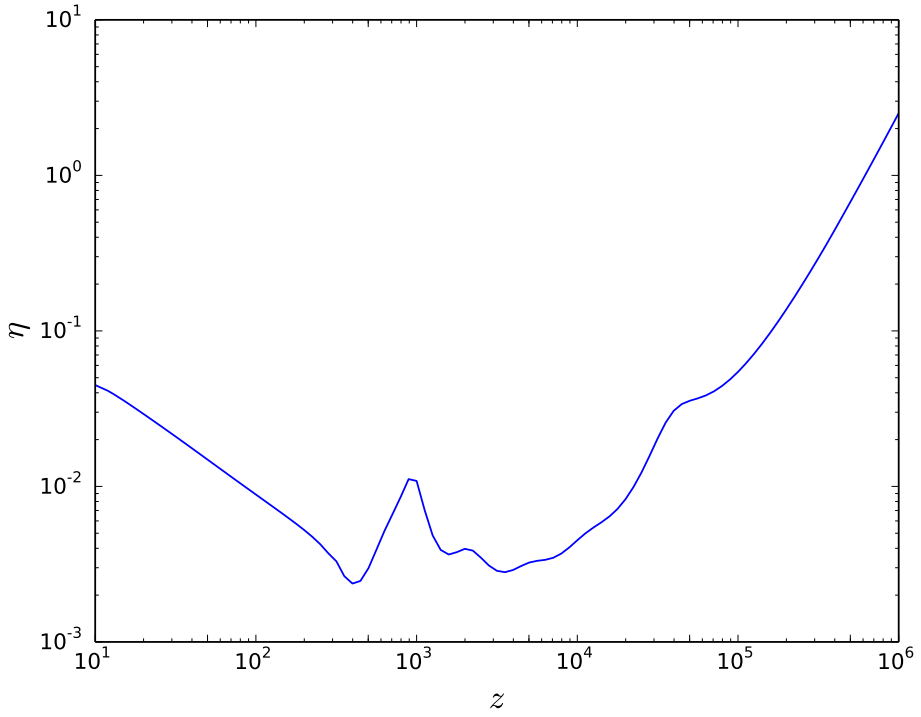

Figure 2.9: The EDE at its critical redshift $\rho_{\rm ede}(z_c)$ is plot as a fraction of the total energy density $\rho_{\Lambda{\rm CMD}}(z_c)$ of a pure ΛCDM universe for a range of redshifts. This fraction is within an order-unity factor of the greatest contribution of the EDE to the energy density of the Universe. This plot was made for $\tau = \tau_{\rm Pl}$ and allowing $\Omega_{\rm ede} = \sigma_{\Omega_{\rm ede}}$.

allows us to constrain an early dark energy model on a level consistent with a full MCMC analysis, and show that it is capable of increasing the value of the Hubble parameter. We conclude that adding an EDE, such as the one considered here, to ΛCDM may form a part of the solution to the Hubble tension if a higher optical depth to reionisation is allowed. If the Hubble tension persists with a 1% measurement of the local value of H_0, then it may be useful to revisit the early-dark-energy model considered here.

2.2 Ultra-Light Axion-like Fields as Early Dark Energy

Ultra light axion-like (ULA) fields arise generically in string theory [93, 113]. They may be cosmologically relevant, contributing to the cold Dark Matter (CDM) *and* DE in our universe (see [113] and references therein). My previous work [37] relied on a similar model to solve the Hubble tension, calling on the presence of an early dark energy (EDE) phase. As a physical model for EDE is required to consistently incorporate the effects of perturbations in the EDE, I next study ULAs as a candidate for EDE and a solution to the Hubble tension.

This section explores the observational implications of a cosmological scalar field with a potential of the form $V_n(\phi) \propto [1 - \cos(\phi/f)]^n$ that becomes dynamical at a range of times, which arises non-perturbatively and breaks the approximate ULA shift symmetry. The standard axion potential is obtained in the $n = 1$ case, while higher-n potentials may be generated by higher-order instanton corrections [114]. Here ϕ denotes the field value and f the ULA decay constant. These fields become dynamical as the Hubble parameter decreases, eventually settling down at the minima of their potentials. Up to the point when the fields become dynamical (i.e. during the period of 'slow-roll' evolution) their equations of state are dark-energy like: $w_{\rm ede} \simeq -1$, hence constituting early dark energy.

Soon after the field becomes dynamical, it starts to oscillate and, when averaged over the oscillation period, has an equation of state equal to $w_{\rm ede} \simeq (n-1)/(n+1)$ for a potential of the form $V_n(\phi) \propto \phi^{2n}$ [115]. As the field oscillates, its energy density dilutes as cold dark matter (CDM) for $n = 1$, for $n = 2$ it dilutes as radiation and for $n = 3$ it dilutes faster

than radiation. With a statistical ensemble of such fields (i.e. the 'axiverse'), the universe may have gone through several periods of 'anomalous' expansion. This general scenario may provide a way to connect the physics of cosmic inflation to our current period of accelerated expansion [95] as well as alleviate the coincidence problem [37, 95, 116–118]. It may also reduce the Hubble constant tension [37] and explain the anomalously low baryon temperature inferred by the EDGES experiment [119].

Recently, the Experiment to Detect the Global EoR (Epoch of Reionisation) Signature (EDGES) claimed measurement of 21-cm absorption at $z \sim 20$ [120], a signal of the spin-flip transition in neutral hydrogen from a time before the Universe was populated with stars which reionised all gas. This measurement implies an exceptionally low 21cm brightness temperature, inconsistent with ΛCDM predictions. If this measurement withstands experimental scrutiny [121], it could indicate that the expansion history at high redshifts could differ from standard assumptions. These observations could be explained through the cosmological effects of a collection of scalar fields, as envisioned in the 'string-axiverse' scenario [91, 93, 121, 122] explored in my previous work [37]. These fields would also affect a variety of cosmological observables, such as CMB and matter power-spectra [123, 124].

This section briefly presents the ULA model and as well as a fluid approximation to the full dynamics. The fluid approximation parametrises the ULA dynamics for arbitrary n in terms of the redshift when the field becomes dynamical, z_c, and the fractional energy density in the axion field at z_c, $f_{z_c} \equiv \Omega_{\rm ede}(z_c)/\Omega_{\rm tot}(z_c)$. The perturbations in the ULA are included in this investigation, building on past work [37]. These perturbations are approximated by a time-averaged fluid component with a time and scale dependent effective

sound speed [113, 123, 125–129] within the 'generalized dark matter' parametrisation [53].

Using *Planck*, measurements of the baryon acoustic oscillations (BAO) and the Joint Light-Curve Analysis (JLA) data [130], we place constraints on ULAs for the $n = 1, 2$ and 3 models. Using a Markov Chain Monte Carlo (MCMC) analysis, we are able to fully explore degeneracies between the ULA parameters and the standard cosmological parameters. We derive constraints on f_{z_c} as a function of z_c for all three models. We find in particular that f_{z_c} becomes partially degenerate with dark energy for all three potentials once $1 + z_c < 10$. When $10 \lesssim 1+z_c \lesssim 3\times10^4$, we find that f_{z_c} is constrained to be $\lesssim 0.004$ for matter-dilution and $f_{z_c} \lesssim 0.02$ for the other two potentials. The constraints then relax with increasing z_c, but we demonstrate that current measurements of the CMB [4] require that f_{z_c} be less than unity as early as $z_c = 10^{10}$. Remarkably, we find that the details of the ULA dynamics could distinguish its effects from other cosmological components, even if the ULA time-averaged equation of state is equal to zero (CDM-like) or 1/3 (radiation-like). Details of these are present in the full text of the publication [38].

Section 2.2.1 reviews the basics of the cosmological dynamics of ULAs by laying out the equations for the homogeneous field dynamics and introducing the dynamics of the perturbed field. The fluid approximation is also presented here. Equipped with this formalism, §2.2.1 describes the rich dynamics of ULA perturbations. The CMB and matter power-spectra that arise in our scenario are calculated using a modified version of the `CLASS` Boltzmann code[5] [54, 131–133]. The MontePython[6] [134] MCMC package is used to ob-

[4] Naturally, alternative probes such as BBN can constrain the parameter space further at such times.

[5] `http://class-code.net`

[6] `http://baudren.github.io/montepython.html`

tain constraints on our scenario. My main contribution to this work was exploring the implications for cosmological tensions in §2.2.3, and minor contributions included aiding in analysis of the MCMC output. Finally, conclusions are drawn in §2.2.4.

2.2.1 The cosmological dynamics of ULAs

Background dynamics

The background dynamics of a ULA have a simple description. The field is initially pinned at some value due to Hubble friction. Once the expansion rate drops below some critical value (related to the mass of the ULA), the field is free to evolve to the minimum of the potential. It then oscillates around the bottom of its potential such that its energy density is diluted due to the subsequent expansion.

The homogeneous Klein-Gordon (KG) equation of motion for the field is given by

$$\ddot{\phi} + 3H\dot{\phi} + \frac{dV_n(\phi)}{d\phi} = 0. \tag{2.17}$$

The ULA potential is given by

$$V_n(\phi) = \Lambda^4(1 - \cos\phi/f)^n, \tag{2.18}$$

where f is the energy scale at which the global $U(1)$ related to axions is spontaneously

broken. The ULA homogeneous energy-density and pressure are

$$\rho_{\rm ede} = \frac{1}{2}\dot{\phi}^2 + V_n(\phi), \tag{2.19}$$

$$P_{\rm ede} = \frac{1}{2}\dot{\phi}^2 - V_n(\phi). \tag{2.20}$$

The Hubble equation can be written

$$H = H_0 E(a) = H_0\sqrt{\Omega_m(a) + \Omega_r(a) + \Omega_\Lambda + \Omega_{\rm ede}(a)}, \tag{2.21}$$

where $\Omega_X \equiv \rho_X/\rho_{\rm crit}$ and $\rho_{\rm crit} = 3H_0^2 M_P^2$, where $M_P \equiv (8\pi G)^{-1/2}$ is the reduced Planck mass. Numerically solving these oscillatory equations is computationally expensive. They can however, be approximated by a fluid with energy density that is initially constant due to Hubble friction (the 'early dark energy' phase) and then dilutes away as [53, 115]

$$\Omega_{\rm ede}(z) = \frac{2\Omega_{\rm ede}(z_c)}{[(1+z_c)/(1+z)]^{3(w_n+1)} + 1}, \tag{2.22}$$

where

$$w_n \equiv \frac{n-1}{n+1}. \tag{2.23}$$

Such a has an associated equation of state $w = P_{\rm ede}/\rho_{\rm ede}$ given by

$$w_{\rm ede}(z) = \frac{1+w_n}{1+[(1+z)/(1+z_c)]^{3(1+w_n)}} - 1, \tag{2.24}$$

which asymptotically approaches -1 as $a \to 0$ and w_n for $z \ll z_c$. For details of the

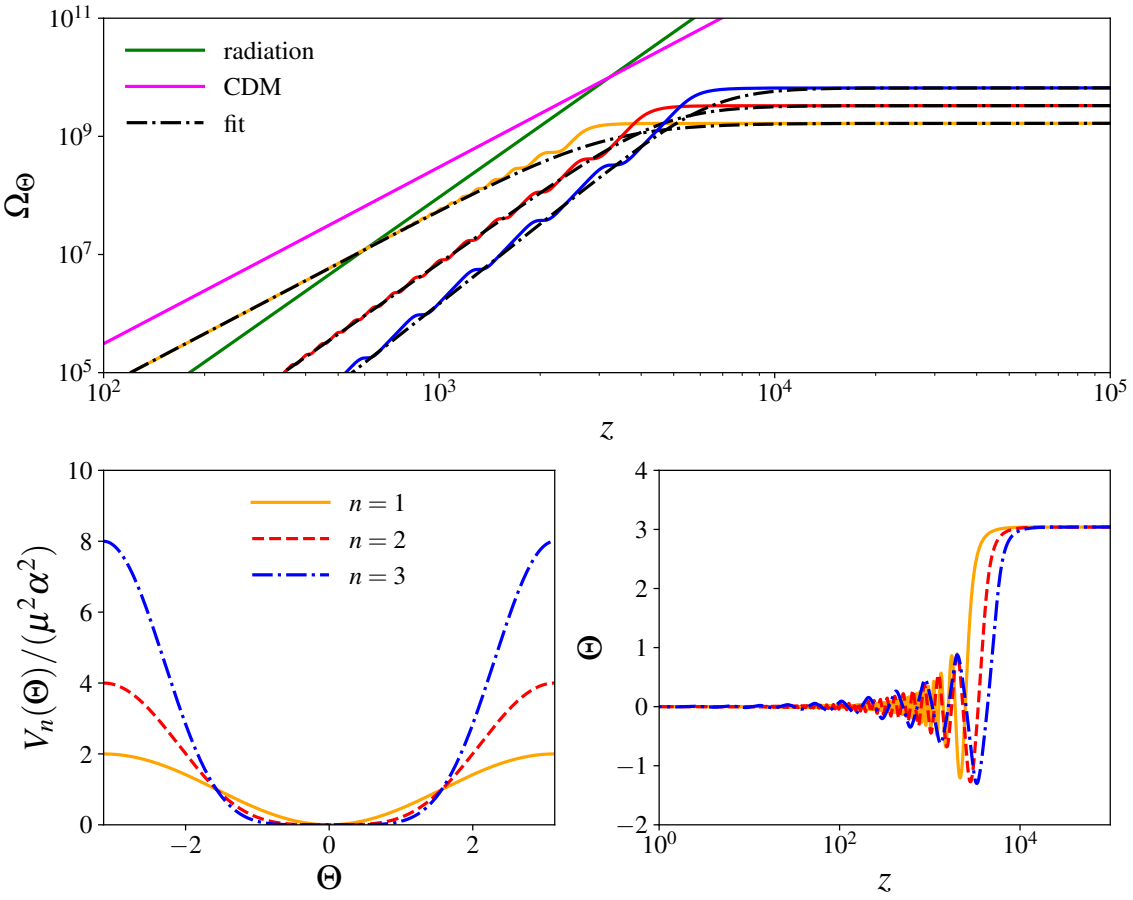

Figure 2.10: The evolution of the background field with $\mu = m/H_0 = 10^6$, $\alpha = f/M_P = 0.05$, and $\Theta_i = \phi_i/f = \pi - 0.1$ for the three forms of the axion potential explored in this work.

derivation of the fluid approximation, see Ref. [38].

Fig. 2.10 shows a comparison between the exact axion energy density and our parametrisation. This shows that when $n = 1$, the homogeneous axion energy density dilutes like matter once the field is dynamical. On the other hand it dilutes like radiation when $n = 2$. When $n \geq 3$, dilution is faster than radiation

Perturbed dynamics in the fluid formalism

Linear perturbations to the axion field will develop and evolve according to the perturbed Klein-Gordon equation. However, these equations are computationally expensive to solve and would not allow us to scan over the parameters of the ULA theory and the standard cosmological parameters. Since the oscillations of the scalar field generally occur with periods much shorter than a Hubble time, much of the dynamics can be captured by averaging over the oscillations and dealing with fluid equations [115]. The equations governing the evolution of density and bulk velocity perturbations can be written in terms of fluid variables in the synchronous gauge as [53]

$$\begin{aligned}\dot{\delta}_{\rm ede} &= -(1+w_{\rm ede})\left(\theta_{\rm ede}+\frac{\dot{h}}{2}\right)-3(c_s^2-w_{\rm ede})\mathcal{H}\delta_{\rm ede} \\ &\quad -9(1+w_{\rm ede})(c_s^2-c_{\rm a}^2)\mathcal{H}\frac{\theta_{\rm ede}}{k^2}\,, \qquad (2.25)\\ \dot{\theta}_{\rm ede} &= -(1-3c_s^2)\mathcal{H}\theta_{\rm ede}+\frac{c_s^2k^2}{1+w_{\rm ede}}\delta_{\rm ede}\,, \qquad (2.26)\end{aligned}$$

where the dot refers to a derivative with respect to conformal time. From the background dynamics, $w_{\rm ede}$ is known. Note that the effective sound speed $c_s^2 \equiv \delta p/\delta\rho$, is possibly different from unity for an ULA, and the adiabatic sound speed

$$c_{\rm a}^2 \equiv \frac{\dot{P}_{\rm ede}}{\dot{\rho}_{\rm ede}} = w_{\rm ede} - \frac{\dot{w}_{\rm ede}}{3(1+w_{\rm ede})\mathcal{H}}\,. \qquad (2.27)$$

In the approximation for $w_{\rm ede}$ given by Eq. (2.24), the adiabatic sound-speed during

the EDE period is given by

$$c_{\rm a}^2 = -\frac{3n+1}{n+1}, \tag{2.28}$$

it then evolves to $w_{\rm ede}$ once the field starts oscillating. We have checked that given that both the exact and parametrised $c_{\rm a}^2$ are negative and of order unity, our parametrisation gives a good approximation to the exact evolution of the perturbations.

Finally, we must determine c_s^2. During the EDE phase $c_s^2 = 1$ for a slowly rolling scalar field, but deviates strongly from 1 once the field starts oscillating. We find that for a ULA potential which takes the form $V \propto \phi^{2n}$ around the minimum:

$$c_s^2 = \frac{2a^2(n-1)\varpi^2 + k^2}{2a^2(n+1)\varpi^2 + k^2}, \tag{2.29}$$

with the oscillation angular frequency $\varpi \propto a^{-3w_n}$. We discuss the dynamics of perturbations in §2.2.1. Before entering into these details, we relate our parametrisation to the ULA theory parameters.

Initial conditions of perturbations

We solve for the ULA dynamics using the GDM equations of motion [53], which require the specification of the ULA equation-of-state $w_{\rm ede}$, the adiabatic sound speed $c_{\rm a}^2$, and effective sound speed c_s^2. During slow roll, generic scalar fields have that $w_{\rm ede} \simeq -1$, $c_{\rm a}^2 \simeq -7/3$, and $c_s^2 = 1$. Since $w_{\rm ede} \simeq -1$ the linear perturbation equations written in terms of the velocity perturbation $\theta_{\rm ede}$ are unstable. To deal with this we solve the evolution of

the perturbations in terms of the heat-flux, $u_{\rm ede} \equiv (1+w_{\rm ede})\theta_{\rm ede}$ [123].

$$\begin{aligned}\dot{\delta}_{\rm ede} &= -\left[u_{\rm ede} + (1+w_{\rm ede})\frac{\dot{h}}{2}\right] - 3(c_s^2 - w_{\rm ede})\mathcal{H}\delta_{\rm ede} \\ &\quad -9(c_s^2 - c_{\rm a}^2)\mathcal{H}\frac{u_{\rm ede}}{k^2}\,, \qquad (2.30)\\ \dot{u}_{\rm ede} &= -(1-3c_s^2)\mathcal{H}u_{\rm ede} + 3\mathcal{H}(w_{\rm ede} - c_{\rm a}^2)u_{\rm ede} \\ &\quad +c_s^2 k^2 \delta_{\rm ede}\,. \qquad (2.31)\end{aligned}$$

In practice, when $z > z_c$, we set $w_{\rm ede} \simeq -1$, $c_s^2 = 1$ and $c_{\rm a}^2$ is given by Eq. (2.28). During the oscillatory phase, when $z < z_c$, c_s^2 is given by the time and scale-dependent effective sound speed in Eq. (2.29), $c_{\rm a}^2$ is given by Eq. (2.27) with $w_{\rm ede}$ given by Eq. (2.24). Abrupt changes in these quantities can lead to the generation of transients in numerical solutions. We have verified that these had no significant effects on the predicted power spectra used to constrain this model.

In the ULA scenario considered here, the ULA component is always subdominant on superhorizon scales and at early times. In that case, the ULA perturbations fall inside the gravitational potential wells created by the radiation component, such that there is a generic attractor solution [135]

$$\begin{aligned}\delta_{\rm ede} &= -\frac{C}{2}(1+w_{\rm ede})\frac{4-3c_s^2}{4-6w_{\rm ede}+3c_s^2}(k\tau)^2, \qquad (2.32)\\ u_{\rm ede} &= -\frac{C}{2}(1+w_{\rm ede})\frac{c_s^2}{4-6w_{\rm ede}+3c_s^2}(k\tau)^3 k, \qquad (2.33)\end{aligned}$$

where C is the initial amplitude and τ is the conformal time. Note that we take $\delta_{\rm ede} =$

$u_{\rm ede} = 0$ initially since these quantities are quickly driven to the attractor solution [135].

2.2.2 Current constraints to ULAs

Using current measurements of the CMB and other probes of large-scale structure, we place constraints on the energy density of ULAs as a function of the time when they become dynamical. Although the CMB decouples around $z \sim 1000$, each multipole carries with it information about the evolution of the universe around the time the scales that form it entered the causal horizon. This, in principle, makes the CMB sensitive to cosmological dynamics as long ago as $z \sim 10^5 - 10^6$ [37, 117].

To perform this analysis we consider a series of fixed values for z_c at which we constrain the energy density in the ULA. We run Monte Carlo Markov chains using the public code MONTE PYTHON [134]. We assume flat priors on $\{\omega_b, \theta_s, A_s, n_s, \tau_{\rm reio}, \omega_{\rm cdm}\}$ and a logarithmic prior on $\Omega_{\rm ede}$. We scan over 9 points in $1 + z_c$ logarithmically distributed between 1 and 10^8. We also vary n to be equal to $(1, 2, 3)$. We make use of *Planck* high-l and low-l TT,TE,EE and lensing likelihood. We include the anisotropic BAO data at $z = 0.2 - 0.75$ from the BOSS DR12 data release [81] and isotropic BAO data at $z = 0.105$ [17] and $z = 0.15$ [80]. We include the Joint Likelihood Analysis (JLA) of supernovae, which includes measurements of the luminosity distance of SN1a up to redshift $z \sim 1$ [130].

The constraints on the density of ULAs today as a function of their dilution redshift $1 + z_c$ are shown in Fig. 2.11.

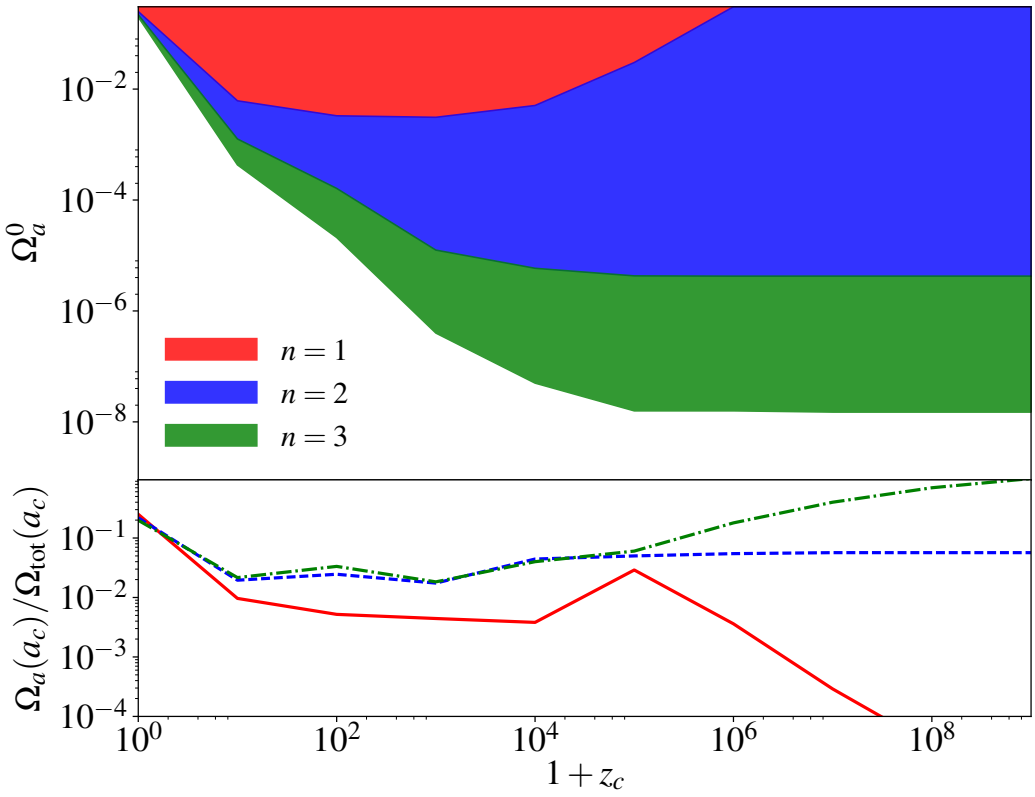

Figure 2.11: *Top panel* – Constraints on the density of the ULA today as a function of its dilution time $1+z_c$. *Bottom panel* – Constraints on the fraction of the total energy content in the form of a ULA at $a_c \equiv (1+z_c)^{-1}$. Here $\Omega_a = \Omega_{\rm ede}$ and $\Omega_a^0 = \Omega_{\rm ede,0}$.

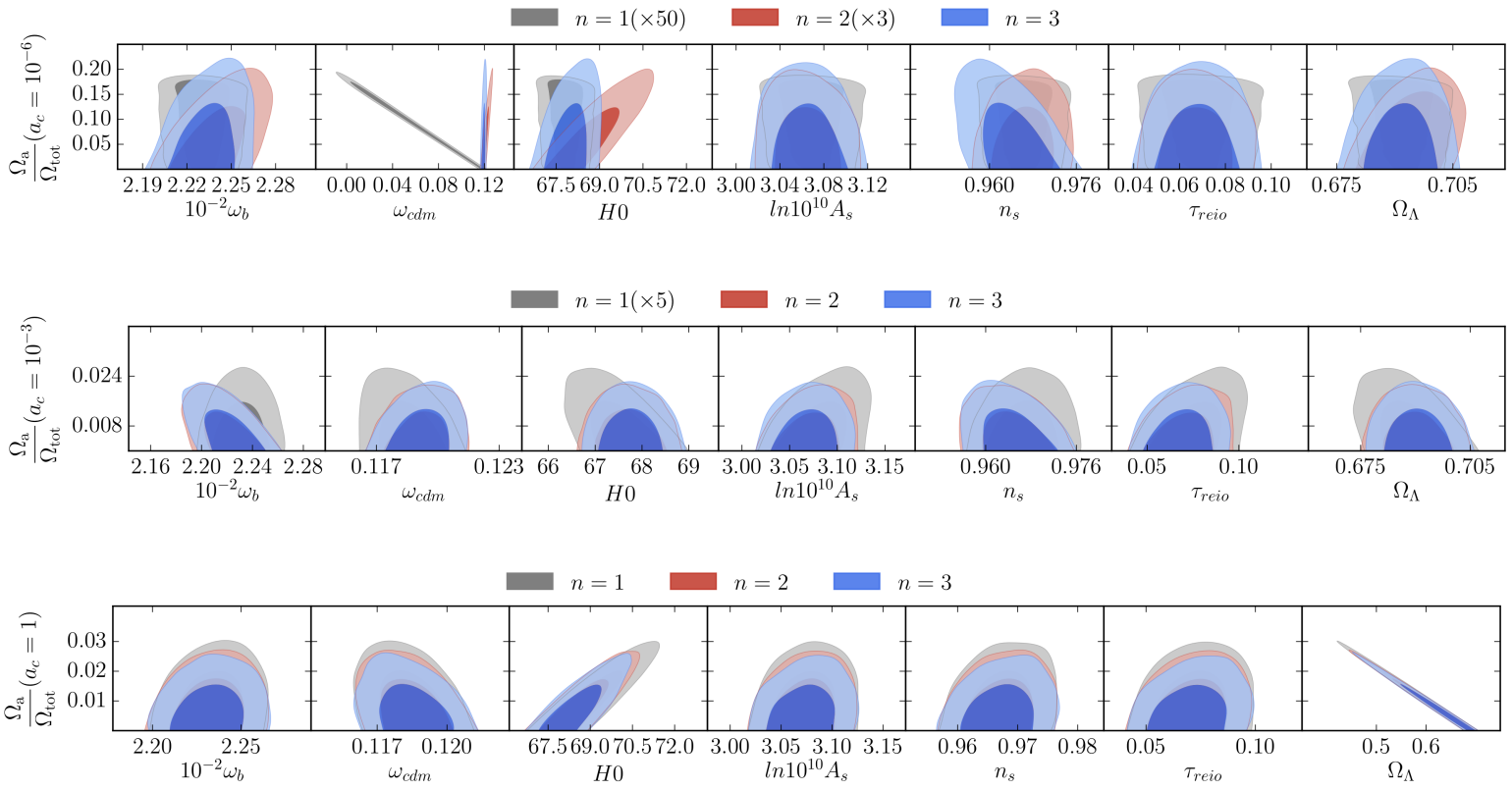

Figure 2.12: Posterior distributions of the density of ULAs today vs the other ΛCDM parameters for $1 + z_c = 1$ (bottom panel), 10^3 (middle panel) and 10^6 (top panel). Here, Ω_a is to be interpreted as $\Omega_{\rm ede}$.

2.2.3 Implications for cosmological tensions

Although most cosmological observables are individually consistent with a ΛCDM cosmology, tensions exist between the predictions of various data sets, such as the Hubble tension [20, 22]. Furthermore, the recent measurement of the sky-averaged 21-cm signal by EDGES is inconsistent with predictions of ΛCDM [120], although the interpretation of the signal is still being explored [121]. In this section, we examine the effect of ULAs on these two tensions.

The Hubble tension

One of the most prominent and persistent tensions in cosmology is the Hubble tension [27, 29]. The current expansion rate of the universe as predicted by the ΛCDM model when fit to the CMB disagrees with local measurements at greater than 3σ [7] [20]. Planck determines H_0 to be 66.93 ± 0.62 km s^{-1} Mpc^{-1}, while the SH0ES (Supernova H0 for the Equation of State Collaboration) collaboration measures a value of 73.24 ± 1.74 km s^{-1} Mpc^{-1} [20]. Numerous explanations have been proposed and studied in the literature [20, 37, 47, 75, 79, 112, 136–139].

In this section, we investigate whether ULAs can alleviate the tension and what regions in the $\Omega_{\rm ede} - z_c$ plane are best suited to do so, similar to Ref. [37]. We use the Friedmann equation to compute H_0 today, given fiducial values for the other cosmological parameters, and the indicated values for z_c and $\Omega_{\rm ede}$. We keep θ_s fixed and let `CLASS` solve for the value of H_0. The results are shown in Fig. 2.13.

[7] The most recent H_0 measurement available when this work was completed was Ref. [20]. The tension has worsened today and exists at a $> 4\sigma$ level [41]

For $n = 1$, we find that no value of $\Omega_{\rm ede,0}$ for values of $1 + z_c \in [10^0, 10^6]$ diminished the H_0 tension. With reference to Fig. 2.12, for $z_c \gg z_{\rm eq}$, the fluid (which approximates ULAs) effectively behaves like CDM for all times that the CMB is sensitive to. The fluid is fully degenerate with CDM, and $\omega_{\rm cdm}$ and $\Omega_{\rm ede}$ are negatively correlated. That is, the CMB cannot distinguish between the fluid and CDM. An increase in the energy density of EDE today will be accompanied by a decrease in the energy density of CDM and there is no change to the value of the Hubble parameter. At the other end, for $z_c \simeq 0$, the fluid is strongly degenerate with Λ. This degeneracy is weaker than that with $\omega_{\rm cdm}$ at $z_c \gg z_{\rm eq}$, because the equation of state parameter of the fluid is not exactly -1, but slightly larger as the EDE field is beginning to roll. Again, an increase in $\Omega_{\rm ede}$ is accompanied with a decrease in Ω_Λ and the value of H_0 remains unaltered. The tension is, however, somewhat alleviated as the fluid is degenerate with H_0 and leads to a larger error on H_0. For intermediate redshifts $z_c \lesssim z_{\rm eq}$, the fluid reduces the value of H_0, exacerbating the tension. The angular diameter distance $D_A(z_*)$ to the CMB fixes the value of $\Omega_m h^2$ and therefore, effectively increasing Ω_m leads to a reduction in h. Hence at best, the $n = 1$ scenario leaves H_0 unaltered, at worst, exacerbates the tension.

The $n = 2$ scenario fares better, as seen from Fig. 2.13. For $z_c < z_*$, it fares similarly to the $n = 1$ case. It is strongly degenerate with Ω_Λ for $z_c \simeq 0$. For $0 < z_c \ll z_*$, the fluid exacerbates the tension. Again, this is due to its effect on $D_A(z_*)$ - it adds to the expansion rate at late times and H_0 must decrease to compensate and preserve $D_A(z_*)$. For $z_c \simeq 10^3$, $\Omega_{\rm ede}$ and H_0 are uncorrelated. As we are already in matter domination by $z = 10^3$, a fluid that behaves like Λ before and radiation after recombination will impact expansion history

only over a finite redshift range around z_c. As the angular diameter distance $D_A(z_*)$ to recombination gets most of its contribution from lower redshifts, its value and therefore H_0 remain largely unchanged. For $z_c > z_*$, the $n = 2$ scenario is degenerate with $N_{\rm eff}$, as it effectively adds more radiation to the Universe. Hence the impact of the fluid on H_0 is similar to that of $N_{\rm eff}$: it increases H_0 and diminishes the tension [20]. We note however, that the $n = 2$ EDE scenario leads to a more significant easing of this tension than a relativistic species with arbitrary sound speed and viscosity, which can only relax the tension at the 2.4σ level [48].

Finally, for the $n = 3$ scenario, for $z_c \lesssim z_*$, the impact of the fluid is similar to the $n = 2$ case. As mentioned before, the $n = 3$ case only impacts expansion history over a small range in redshift centred around z_c. For $z_c > z_*$ and $\Omega_{\rm ede,0}$ larger than our current constraints, the pre-recombination expansion rate is increased. This decreases the radius r_s of the sound horizon at recombination and H_0 increases to compensate and preserve θ_s. Hence, the ULA EDE is capable of increasing H_0 as seen in Fig. 2.13.

The CMB becomes insensitive to physics above $z \sim 10^6$ as noted by [37,117]. Therefore, for a given $\Omega_{\rm ede,0}$, even as z_c increases above 10^6, the energy density of the EDE for $z \lesssim 10^6$ remains unchanged, as does the Hubble parameter. We hence only show the change to the Hubble parameter due to the addition of ULAs up to $1 + z_c = 10^6$.

To summarize, we find that in order for ULAs to diminish the Hubble tension, we require $n = 2$ or 3 and $z_* < z_c \lesssim 10^6$. While it may seem worrisome that a full solution to the H_0 tension requires $\Omega_{\rm ede}$ larger than our constraints from Fig. 2.11, this exercise

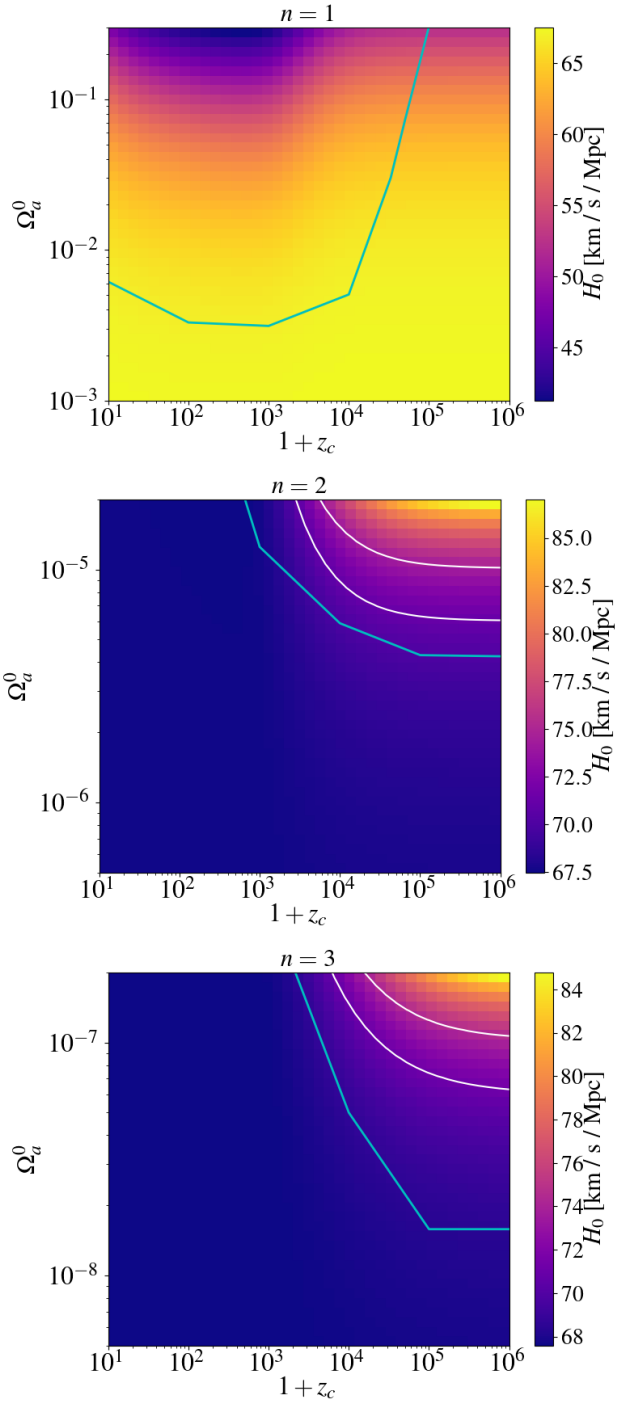

Figure 2.13: Hubble parameter H_0 for various values of $\Omega_{\rm ede,0} (= \Omega_a^0)$ and z_c, for the $n = 1$ (top panel), $n = 2$ (middle panel) and $n = 3$ case (bottom panel). The cyan line represents the constraints shown in Fig. 2.11. The white contours show the 1σ contour on the H_0 value measured by SH0ES [20].

did not exploit all available data or parameter space. In this section, the cosmological parameters are maximised over, that is, fixed at their maximum likelihood values while just the ULA EDE parameters and H_0 are varied. However, shifting one of the cosmological parameters within its 1σ contour could allow more wiggle room for H_0. Therefore, to probe all available parameter space with all available data, (1) the SH0ES measurement could be included in the analysis and (2) all parameters (cosmological and ULA) should be allowed to vary simultaneously and be marginalised over. This is done in Ref. [39] and summarised in §2.3.

EDGES exotic 21 cm measurement

EDGES recently measured the sky-averaged 21cm brightness temperature [120] around the redshift range $z = 15 - 20$ to be roughly 2.5 times smaller (3.8σ) than that predicted by ΛCDM. [8] Two main classes of solution have been suggested to explain this measurement: either the temperature of the photons against which the 21-cm temperature of the gas is measured is brighter than that of the CMB [140–142] or the baryon temperature T_b is cooler than expected based on ΛCDM [119,120,143,144]. In the latter scenario, the EDGES measurement indicates that the baryon temperature T_b at $z = 20$ is smaller than 7K at 99% C.L.

In Ref. [119], the implications of EDGES were explored for the EDE model proposed in my previous work [37], equivalent in this context to the limit $n \to \infty$ for ULA EDE, including only the effect of EDE on the homogeneous evolution of densities and temperatures. Here

[8] The interpretation of this this measurement is still under discussion [121].

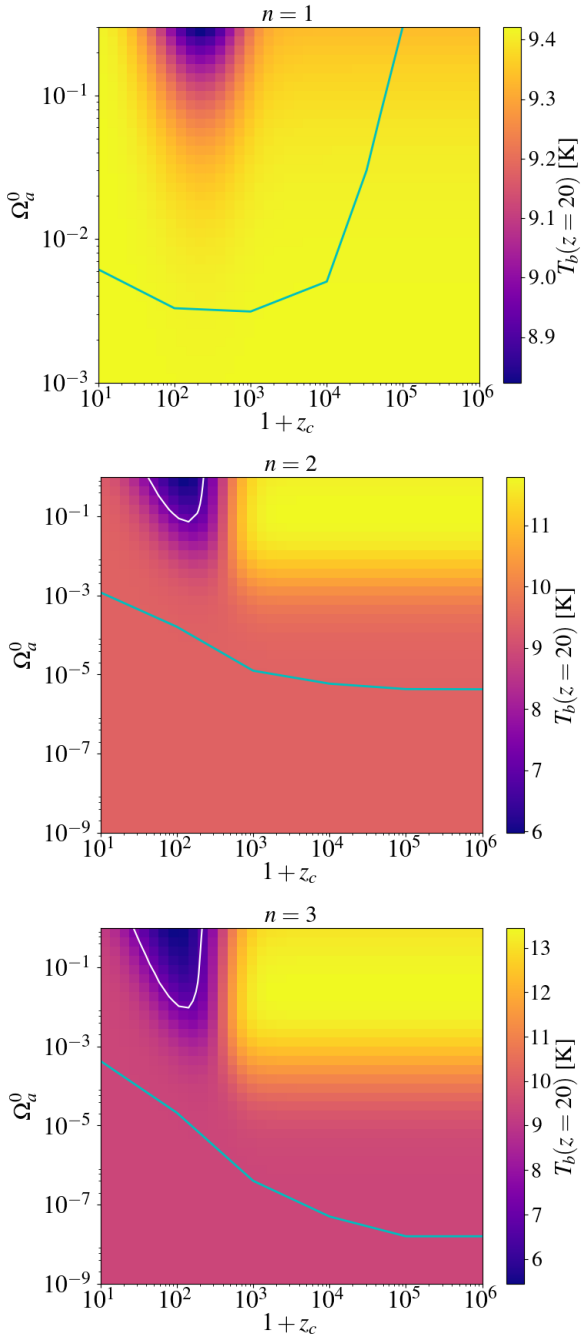

Figure 2.14: Baryon temperature at $z = 20$ (close to the minimum of the absorption trough measured by EDGES [120]) as a function of the ULA density today $\Omega_{\rm ede,0} (= \Omega_a^0)$ and critical redshift z_c. The top panel presents the $n = 1$ case, the middle panel the $n = 2$ case and the bottom panel the $n = 3$ case. The white line shows $T_b = 7$ K, i.e. the 99% upper-limit on the temperature measured by EDGES. The cyan line shows the *Planck* 95% C.L. limit derived in this work. All models of interest are excluded by our analysis.

we perform a similar analysis for $n = 1$, 2, and 3, including perturbations in a ULA fluid.

In the absence of any additional sources, the baryon gas temperature is driven by the balance between Compton heating and Hubble cooling

$$\frac{dT_b}{dz} = \frac{T_b(z) - T_{CMB}(z)}{(1+z)H(z)t_C(z)} + \frac{2T_b(z)}{(1+z)}\,. \tag{2.34}$$

where $t_C(z)$ is the Compton-heating timescale. The key idea used in Ref. [119] is, if the expansion rate before $z \sim 20$ is increased, the gas temperature decouples from the CMB temperature earlier, giving the gas more time to adiabatically cool. Within ΛCDM, baryons decouple around $z \sim 150$. To reach the 99% C.L. upper limit on the level of absorption measured by EDGES at $z \sim 20$, the decoupling would need to happen around $z \sim 210$. The presence of ULA EDE that would dominate the expansion rate over a short period of time can potentially lead to a decoupling satisfying this condition.

We show in Fig. 2.14 the baryon temperature at $z = 20$ (close to the minimum of the absorption trough measured by EDGES [120]) as a function of the ULA density today $\Omega_{\rm ede,0}$ and critical redshift z_c, for each value of n. To produce this figure, we fixed all ΛCDM parameters including the Hubble rate H_0 to values compatible with *Planck* 2015 data [9]. Interestingly, we confirm that there exists a region of parameter space, centered around $z_c \sim 100$ where the EDGES signal can be explained, in the $n = 2$ and $n = 3$ case. Our constraints on the ULA density from *Planck* data however strongly exclude all

[9] In `CLASS`, these equations can be solved using either *Recfast* [145,146] or *HyRec* [147] and Eq. (2.34). Our choice of keeping H_0 fixed is motivated by the fact that adjusting θ_s requires strongly unphysical values of the Hubble rate (sometimes smaller than 0.01 km/s/Mpc) for which both *Recfast* and *HyRec* have difficulties to solve the cosmological recombination history. This also allows for a direct comparison with Ref. [119] where the same approach was used.

of these models, in agreement with Ref. [119]. Although this result was also obtained by maximising over other parameters, marginalising over other parameters does not provide a solution either.

2.2.4 Conclusions

This work studies ultra-light axion-like particles with a fluid approximation. Equipped with this fluid formalism, we have compared the phenomenological consequences of axion-like potentials with $n = 1$ which dilutes as cold dark matter (CDM), $n = 2$ which dilutes as radiation, and $n = 3$ which dilutes faster than radiation. We were thus able to explore any degeneracy the ULAs may have with known cosmological components, in particular CDM and neutrinos, and quantify the sensitivity of the data to a ULA component that decays even faster than radiation. We have constrained the abundance of ULAs as a function of z_c using current cosmological data sets with an MCMC analysis, in order to fully explore degeneracies between the ULA parameters and the standard cosmological parameters.

Next, we studied the implications of our constraints for cosmological tensions. On the one hand, the explanation of the EDGES signal is excluded by more than three orders of magnitude. On the other, we have shown that fields with $n = 2$ and $n = 3$ can significantly ease the Hubble tension, as previously found for $n \to \infty$. Contrary to expectation, the $n = 2$ scenario is favoured over $n = 3$ even if the latter dilutes faster. This was done by only maximising over other cosmological parameters, calling for a more involved analysis of ULA EDE as a solution to the Hubble tension by marginalising over other parameters.

2.3 A Resolution of the Hubble Tension with Early Dark Energy

Two physical model for EDE are presented and tested as solutions to the Hubble tension; one that involves an oscillating scalar field and another with a slowly-rolling scalar field. These models allow us to perform a complete analysis of the growth of perturbations and of CMB fluctuations. We then perform a thorough search of the parameter space for the scalar-field model parameters, along with the classical cosmological parameters. Doing so, we find regions of the combined parameter space where the CMB likelihoods match (and even slightly improve upon) those in the best-fit ΛCDM model with values of H_0 consistent with those from local measurements. Moreover, our cosmological model is in good agreement with constraints from BAO [17,80,81] and the Pantheon supernovae dataset [148]. The fact that both an oscillating and slowly-rolling scalar field can resolve the Hubble tension indicates further that the success of the resolution does not depend on the detailed mechanism that underlies it. Our resolution requires a $\sim 5\%$ contribution from EDE to the total energy density at redshift $z \simeq 5000$ that then dilutes later. Interestingly, hints for such an increased expansion rate and/or reduced sound horizon had been previously identified [72, 149].

Our first model for EDE is nominally a scalar field φ with a potential $V(\varphi) \propto (1 - \cos[\varphi/f])^n$ [95]. At early times, the field is frozen and acts as a cosmological constant, but when the Hubble parameter drops below some value, at a critical redshift $z_c = a_c^{-1} - 1$, the field begins to oscillate and then behaves as a fluid with an equation of state $w_n = (n-1)/(n+1)$. In practice, numerical evolution of the scalar-field equations of motion

becomes extremely difficult once the oscillations become rapid compared with the expansion rate, and so our numerical work is accomplished with an effective-fluid approach [38] that has been tailored specifically for this potential. Still, as that work (and discussion below) indicates, our conclusions do not depend on the details of the potential and would work just as well with, e.g., a simpler φ^{2n} potential. Our second model is a field that slowly rolls down a potential that is linear in φ at early times and asymptotes to zero at late times. Numerical evolution of the scalar-field equations of motion confirm that the resolutions we find here with the effective-fluid approach are valid for that model as well.

In the effective-fluid approximation, the EDE energy density evolves as [38]

$$\Omega_{\rm ede}(a) = \frac{2\Omega_{\rm ede}(a_c)}{(a/a_c)^{3(w_n+1)}+1}, \tag{2.35}$$

which has an associated equation-of-state parameter

$$w_{\rm ede}(z) \;\; = \;\; \frac{1+w_n}{1+(a_c/a)^{3(1+w_n)}} - 1. \tag{2.36}$$

It asymptotically approaches -1 as $a \to 0$ and w_n for $a \gg a_c$, showing that the energy density is constant at early times and dilutes as $a^{-3(1+w_n)}$ once the field is dynamical [150]. The homogeneous EDE energy density dilutes like matter for $n = 1$, like radiation for $n = 2$ and faster than radiation whenever $n \geq 3$. For $n \to \infty$, on reaching the minimum of the potential, $w_\infty = 1$ (i.e. the scalar field is fully dominated by its kinetic energy) and the energy density dilutes as a^{-6}.

The equations governing the evolution of the perturbations to the effective density $\delta_{\rm ede}$ and heat flux $u_{\rm ede} \equiv (1 + w_{\rm ede})\theta_{\rm ede}$, where $\theta_{\rm ede}$ is the bulk velocity perturbation, can be written as discussed in Refs. [38,53,123]. Solving these equations requires the specification of the EDE equation-of-state $w_{\rm ede}(z)$, the adiabatic sound speed $c_{\rm a}^2 \equiv \dot{P}_{\rm ede}/\dot{\rho}_{\rm ede}$ and effective sound speed $c_s^2 \equiv \delta p_\varphi/\delta\rho_\varphi$ (defined in the rest-frame of the field). During slow roll and assuming $\dot{\varphi}_i = 0$, generic scalar fields have $w_{\rm ede} \simeq -1$, $c_{\rm a}^2 \simeq -7/3$, and $c_s^2 = 1$ [38, 123]. When the field becomes dynamical, $w_{\rm ede}$ and $c_{\rm a}^2$ can be calculated from the background parametrization. The exact behavior of c_s^2 depends on the particular shape of the potential as described in Ref. [38]. We also note that, just as with the background dynamics, this parametrization describes the case of the slow-roll model by taking the limit $n \to \infty$ and setting $c_s^2 = 1$ [53].

We run a Markov Chain Monte Carlo (MCMC) using the public code MontePython-v3[10] [134,151] and a modified version of the CLASS-code [54,131]. We perform the analysis with a Metropolis-Hasting algorithm, assuming flat priors on the ΛCDMand EDE parameters $\{\omega_b, \omega_{\rm cdm}, \theta_s, A_s, n_s, \tau_{\rm reio}, \Omega_{\rm ede,0}, {\rm Log}_{10}(a_c), \phi_i\}$. In addition, we run separate MCMCs to compare $n = (2, 3, \infty)$. Following the *Planck* collaboration, we model free-streaming neutrinos as two massless species and one massive with $\Sigma m_\nu = 0.06$ eV [152]. Our data sets include the latest SH0ES measurement of the present-day Hubble rate $H_0 = 73.52 \pm 1.62$ km/s/Mpc [83] [11] *Planck* high-ℓ and low-ℓ TT,TE,EE and lensing likelihood [153]. We also include BAO measurements from 6dFGS at $z = 0.106$ [17], from the MGS galaxy sample of SDSS at $z = 0.15$ [80], and from the CMASS and LOWZ galaxy samples of BOSS DR12

[10] `https://github.com/brinckmann/montepython_public`

[11] The most precise local measurement of the Hubble constant available at the time this work was completed was Ref. [83], different from that in §2.1 and §2.2.

at $z = 0.38$, 0.51, and 0.61 [81]. Note that the BOSS DR12 measurements also include measurements of the growth function $f\sigma_8(z)$. Additionally, we use the Pantheon [12] supernovae dataset [148], which includes measurements of the luminosity distances of 1048 SNe Ia in the redshift range $0.01 < z < 2.3$. Moreover, there are many nuisance parameters that we analyze together with the cosmological ones using a Choleski decomposition [154]. We consider chains to be converged using the Gelman-Rubin [155] criterion $R - 1 < 0.1$.

In Fig. 2.15, we show the marginalized 1D and 2D posterior distributions of H_0, $\omega_{\rm cdm}$, $f_{\rm EDE}(a_c)$ and $\mathrm{Log}_{10}(a_c)$ in ΛCDM and in the EDE cosmology with $n = 2$, 3 and $n \to \infty$, where $f_{\rm EDE}(a_c) \equiv \Omega_{\rm ede}(a_c)/\Omega_{\rm tot}(a_c)$. We report the best-fit χ^2 for each experiment in Table 2.2, while the reconstructed mean, best fit and 1σ confidence interval of the cosmological parameters are given in Table 2.3. We find that the best-fit χ^2 in the EDE cosmology is reduced by -9 to -14 compared to ΛCDM using the same collection of data-sets. This reduction in the χ^2 is not only driven by an improved fit of SH0ES data, but also by an improved fit of CMB data compared to a ΛCDM fit to all data-sets. Interestingly, in the global fit, the EDE fits *Planck* data slightly better than ΛCDM fitted on *Planck only* [13]. This is in stark contrast with the case of extra-relativistic degrees of freedom, for which the χ^2 of CMB and BAO data degrades (as shown on the last column of Table 2.2 and also found by Refs. [27, 47, 48]).

One of the most interesting aspects of the EDE resolution of the Hubble tension is that the posterior distributions show that the field must become dynamical around matter-

[12] `https://github.com/dscolnic/Pantheon`

[13] The fit of ΛCDM on *Planck* only yields $\chi^2_{Planck} \simeq 12951.5$ for the exact same precision parameters as the one used in the EDE fits and convergence criterion $R - 1 < 0.008$. It can vary slightly from the one quoted in *Planck* tables [22].

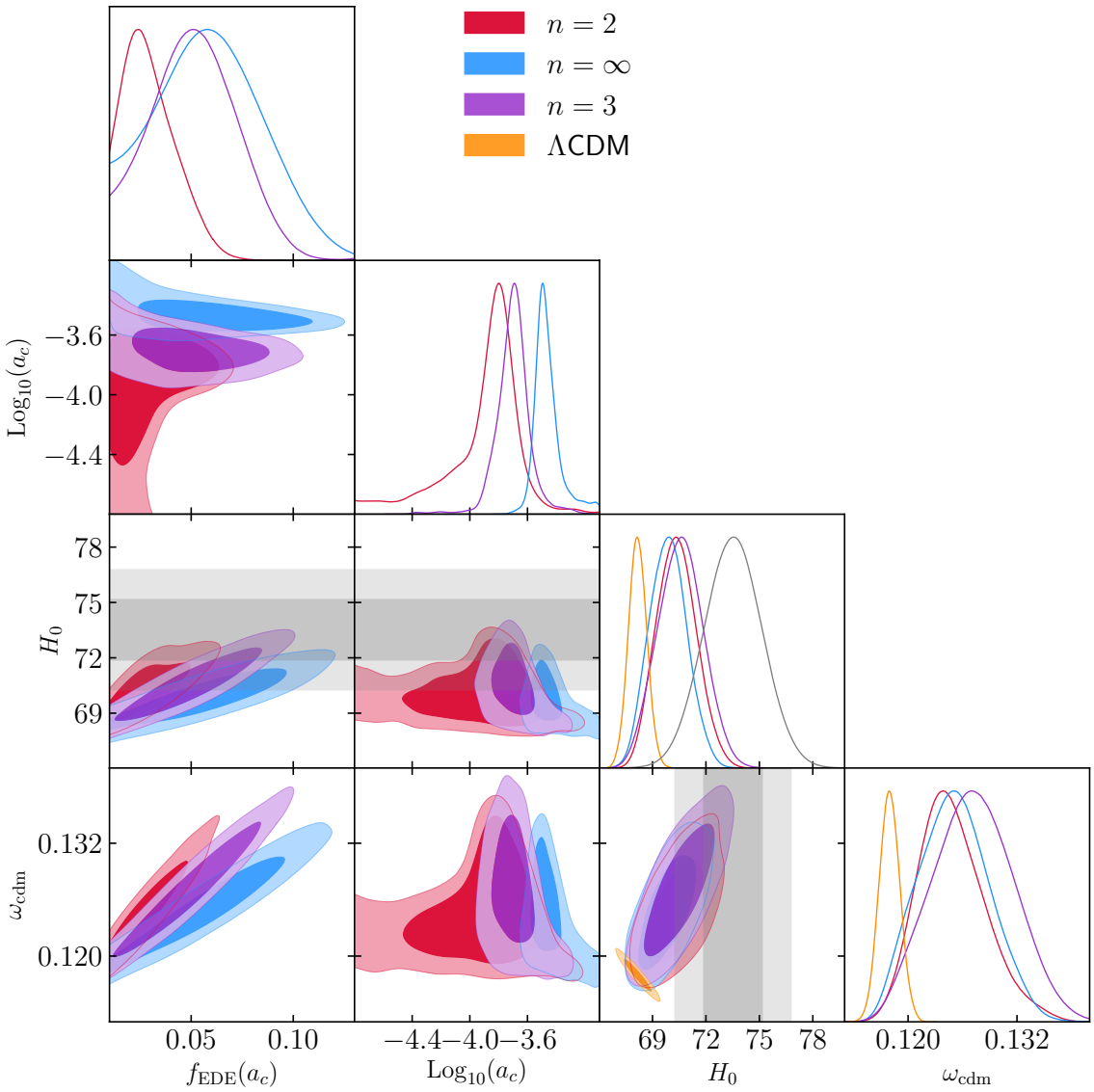

Figure 2.15: Comparison between the marginalized 1D and 2D posterior distributions of H_0, ω_{cdm}, $f_{\mathrm{EDE}}(a_c)$ and $\mathrm{Log}_{10}(a_c)$ in the EDE cosmology with $n = 2$, $n = 3$ and $n = \infty$. The best fit value of H_0 in ΛCDM is shown in orange; the one from SH0ES is shown in grey.

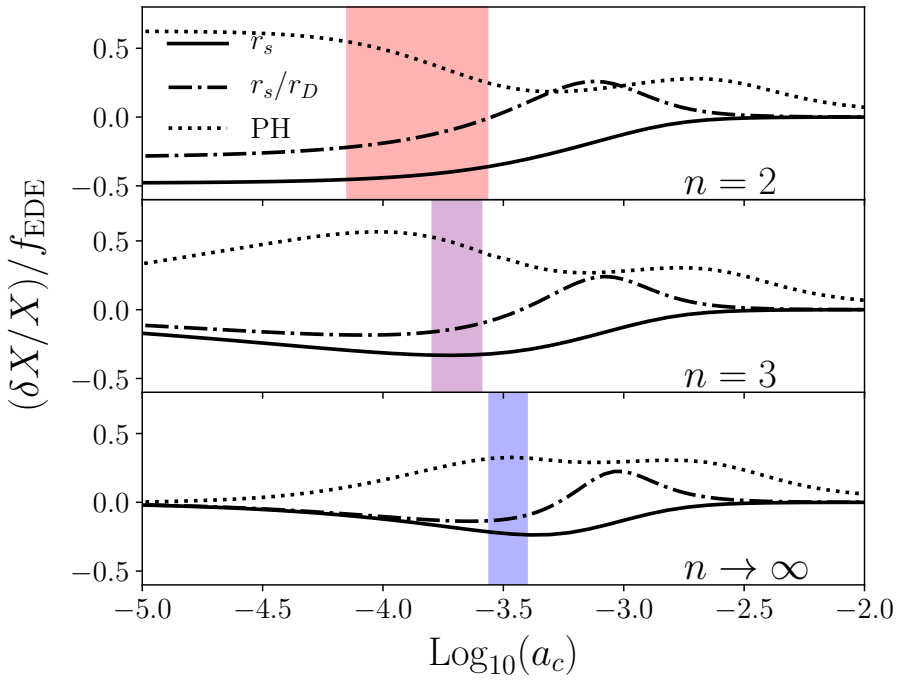

Figure 2.16: The variation of the scales that are 'fixed' by the CMB data with respect to $f_{\rm EDE}(a_c)$ as a function of a_c with all other cosmological parameters fixed at their *Planck* best-fit values [25]. The colored bands indicate the marginalized 1σ range of a_c for each EDE model considered here.

radiation equality. Within the context of ΛCDM, a simplified picture of the CMB power spectrum can be described by three angular scales: $\ell_{\rm eq}$ (the projected Hubble horizon at matter-radiation equality), ℓ_s (the projected photon-baryon sound-horizon at decoupling), and ℓ_D (the projected Silk damping scale at decoupling) [156]. These angular scales are given by the ratio of a physical scale at decoupling with the angular diameter distance to the surface of last scattering: $\ell_X = \pi D_A(z_*)/r_X(z_*)$. Additionally, the overall amplitudes of the CMB peaks (in particular, the first one) are accurately measured by *Planck*. It is straightforward to show that PH $\propto \omega_{\rm cdm}^{-0.5}$, $\ell_{\rm eq} \propto \omega_{\rm cdm}^{0.5} h^{-0.2}$, $\ell_s \propto \omega_{\rm cdm}^{-0.16} h^{-0.2}$, $\ell_s/\ell_D = r_s/r_D \propto \omega_{\rm cdm}^{0.03}$, where PH stands for the height of the first peak and we assume that the heights of the even and odd peaks fixes ω_b. In ΛCDM, the measured peak height determines $\omega_{\rm cdm}$, allowing an inference of h through $\ell_{\rm eq}$, ℓ_s, and ℓ_D. Alternatively, using the determination of H_0 from SH0ES, one would deduce values of $\ell_{\rm eq}$, ℓ_s, and ℓ_D too small compared to their measured values. As shown by several recent studies [27, 28, 72], this can be re-cast as a mismatch between the sound horizon deduced from *Planck* data, and that reconstructed from the standard distance ladder. The value of r_s measured by Planck is higher by ~ 10 Mpc compared to that directly deduced from the distance ladder.

The role of the EDE is to decrease r_s, while keeping the angular scales and peak heights fixed via small shifts in other cosmological parameters. For each value of n, we show the fractional change in r_s, r_s/r_D and PH with $f_{\rm EDE}(a_c)$ as a function of a_c in Fig. 2.16. The 1σ errors on a_c, reconstructed from our analysis, are also shown. Unsurprisingly we find that the value of a_c is driven to be close to the maximal fractional change in r_s (solid line). Additionally, one can see that such an EDE leads to a shift in the ratio r_s/r_D (dash-dotted

line) and increase in peak height (dotted line). From the above scaling relations it is clear that the increase in the peak height can be compensated by an increase in $\omega_{\rm cdm}$, giving the positive correlation between $f_{\rm EDE}(a_c)$ and $\omega_{\rm cdm}$ visible in the 2D-posterior distribution shown in Fig. 2.15. Moreover, the dynamics of the EDE compensate for such a change in $\omega_{\rm cdm}$, leaving the imprint of $\ell_{\rm eq}$ on the power spectra relatively unchanged. An increase in $\omega_{\rm cdm}$ leaves r_s/r_D roughly unaffected but this ratio cannot be kept fully fixed. This brings us to our main conclusion: the favoured EDE model is the one that, while maximizing the decrease in r_s, minimizes [14] the change in r_s/r_D. Using these scaling laws, for $n = 3$ a resolution of the Hubble tension will roughly require $\delta\omega_{\rm cdm} \simeq 0.01$ and $f_{\rm EDE}(a_c) \simeq 0.1$ at $\mathrm{Log}_{10}(a_c) \simeq -3.7$. Strikingly, this crude estimate agrees well with the best-fit values in Table 2.3. This analysis also explains why $n = 3$ is favored over the $n = 2$ and $n \to \infty$ case. Moreover, we can understand why the EDE cosmology is a "better" resolution of the Hubble tension than increasing the effective number $N_{\rm eff}$ of neutrino degrees of freedom: the effects of an additional radiation energy density can be read off of Fig. 2.16 for the $n = 2$ case at $\mathrm{Log}_{10}(a_c) \ll -4.5$. In that case, the EDE simply behaves like additional radiation at all relevant times. One can see that r_s/r_D is significantly affected, leading to additional tension with the data, as previously noted in Ref. [157].

We find that it is essential to consistently include perturbations in the EDE fluid. Neglecting perturbations is inconsistent with the requirement of overall energy conservation and therefore leads to unphysical features in the CMB power spectra which restrict the success of the resolution. This, in part, explains why my former study [37] did not find a

[14] In practice, a relatively small shift in r_s/r_D is allowed as long as a small shift in n_s can compensate for it, leading to a mild shift in the best-fit value of n_s (see Table 2.3).

good fit to the CMB for $f_{\rm EDE}(a_c \simeq 10^{-3.5}) \sim 5\%$.

In Fig. 2.17, we show the residuals of the CMB TT (top panel) and EE (bottom panel) power spectra calculated in the best-fit EDE model with respect to our best-fit ΛCDM (i.e. fit on all datasets). One can see that the EDE leads to residual oscillations particularly visible at small scales in the EE power-spectrum, which represent an interesting target for next-generation experiments such as the Simons Observatory [152], CMB-S4 [158] or CoRE [159]. Additionally, the pattern around the first peak ($\ell \sim 30 - 500$) in the EE spectrum might be detectable in the future by large-scales E-mode measurements such as CLASS [160] or LiteBird [161]. Finally, the changes in r_s, n_s, and A_s leave signatures in the matter power spectrum that can potentially be probed by surveys such as KiDS, DES and Euclid. This can also be seen in the parameter $S_8 \equiv \sigma_8(\Omega_m/0.3)^{0.5}$, which is shifted by about 1σ upwards from its ΛCDM value. This slightly increases the so-called "S_8 tension" (e.g. [26]) and therefore deserves more attention in future work. As a first check, we have performed additional runs including SDSS DR7 [162] and KiDS [163] likelihoods, and found that our conclusions are unaffected.

This work shows that an EDE that begins to dilute faster than matter at a redshift $z_c \gtrsim 3000$ can explain the increasingly significant (now 4.4σ) tension between H_0 inferred from the CMB [25] and Cepheid variables/supernovae at low redshifts [83]. Using *Planck*, BAO measurements, the Pantheon supernovae data, the local SH0ES measurement of H_0 and a MCMC analysis, we found that a field accounting for $\sim 5\%$ of the total energy density around $z \sim 5000$ and diluting faster than radiation afterwards can solve the Hubble tension without upsetting the fit to other data sets. We found that in the EDE cosmology the

best-fit χ^2 is reduced by -9 to -14 (with a slight preference for $n = 3$) compared to ΛCDM using the same data-sets. Moreover, the ΛCDM fit to just the *Planck* data is as good as the combined fit to all of the data sets in the EDE cosmology. This is in stark contrast with the popular increased-$N_{\rm eff}$ resolution.

The oscillating field EDE may naturally arise in the 'string-axiverse' scenario [91, 93, 95, 122, 164]. The standard axion potential is obtained for $n = 1$, while higher-n potentials may be generated by higher-order instanton corrections [114]. The EDE resolution of the Hubble tension, along with the current accelerated expansion and the evidence for early-Universe inflation (and perhaps the accelerated expansion postulated [38, 119] to account for EDGES [120]) may suggest that the Universe undergoes episodic periods of anomolous expansion, as suggested in Refs. [37, 95, 116–118, 165].

A future cosmic-variance-limited experiment around $\ell \sim 30 - 500$ and above $\ell \sim 1500$ could probe the specific residual oscillations in the CMB power spectra associated with the EDE dynamics, while the shifts in A_s, n_s, r_s, and $k_{\rm eq}$ will be probed by future LSS surveys.

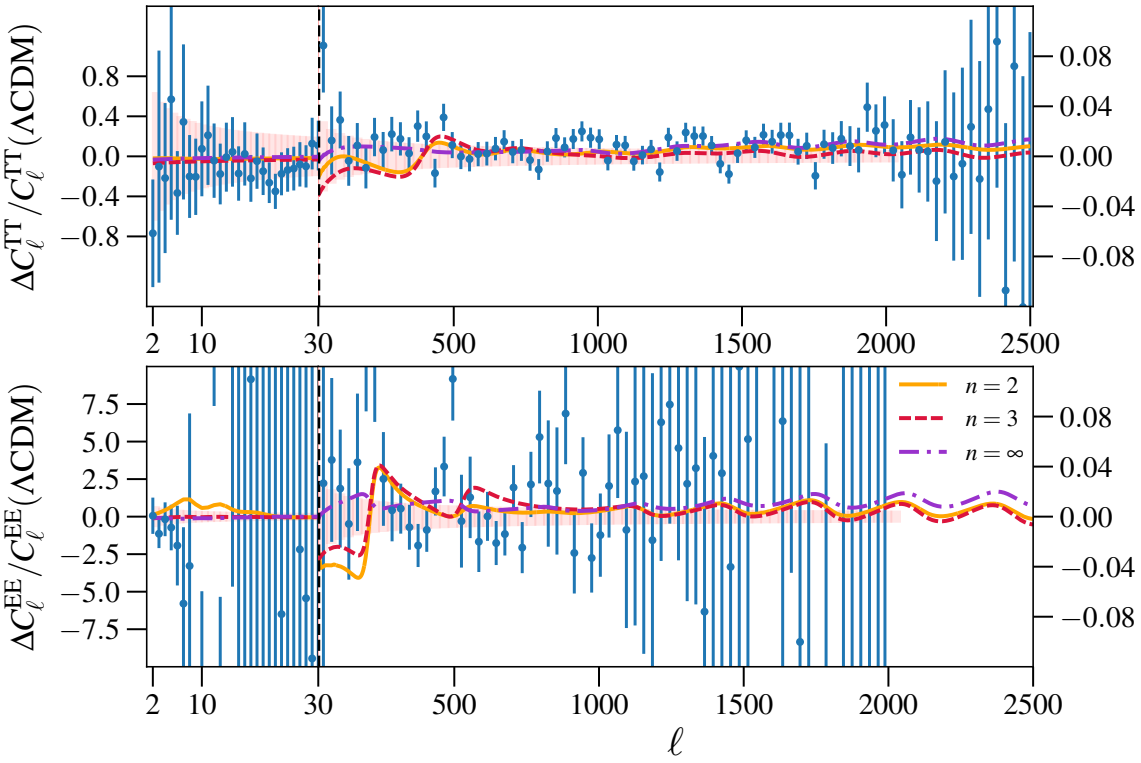

Figure 2.17: Residuals of the CMB TT (top panel) and EE (bottom panel) power spectra calculated in the best-fit EDE model with respect to ΛCDM, obtained from our MCMC analyses. Blue points show residuals of *Planck* data, while orange bands show the binned Cosmic Variance with the same bins and weights as *Planck*.

Datasets	ΛCDM	$n = 2$	$n = 3$	$n = \infty$	$N_{\rm eff}$
Planck high-ℓ	2449.5	2448.4	2445.9	2445.4	2451.9
Planck low-ℓ	10494.7	10494.2	10492.8	10493.8	10493.8
Planck lensing	9.2	9.4	9.6	11.7	9.8
BAO-low z	1.7	2.1	2.1	1.8	2.7
BAO-high z	1.8	1.9	1.9	1.9	2.0
Pantheon	1027.1	1027.3	1026.9	1026.9	1027.1
SH0ES	11.1	2.3	1.4	4.6	3.9
Total $\chi^2_{\rm min}$	13995.1	13985.6	13980.6	13986.0	13991.2
$\Delta\chi^2_{\rm min}$	0	-9.5	-14.5	-9.1	-3.9
$\Delta \log B^{15}$	0	-0.51	+2.51	+2.41	-0.44

Table 2.2: The best-fit χ^2 per experiment for the standard ΛCDM model, the EDE cosmologies and ΛCDM+$N_{\rm eff}$. The BAO-low z and high z datasets correspond to $z \sim 0.1 - 0.15$ and $z \sim 0.4 - 0.6$, respectively. For comparison, using the same CLASS precision parameters and MontePython, a ΛCDM fit to *Planck* data only yields $\chi^2_{{\rm high}-\ell} \simeq 2446.2$, $\chi^2_{{\rm low}-\ell} \simeq 10495.9$ and $\chi^2_{\rm lensing} \simeq 9.4$ with $R - 1 < 0.008$.

Parameter	ΛCDM	$n = 2$	$n = 3$	$n = \infty$
$100\ \theta_s$	$1.04198\ (1.04213) \pm 0.0003$	$1.04175\ (1.0414)^{+0.00046}_{-0.00064}$	$1.04138\ (1.0414) \pm 0.0004$	$1.04159\ (1.04149) \pm 0.00035$
$100\ \omega_b$	$2.238\ (2.239) \pm 0.014$	$2.244\ (2.228)^{+0.019}_{-0.022}$	$2.255\ (0.258) \pm 0.022$	$2.257\ (2.277) \pm 0.024$
$\omega_{\rm cdm}$	$0.1179\ (0.1177) \pm 0.0012$	$0.1248\ (0.1281)^{+0.003}_{-0.0041}$	$0.1272\ (0.1299)_{\pm}0.0045$	$0.1248\ (0.1249) \pm 0.0041$
$10^9 A_s$	$2.176\ (2.14) \pm 0.051$	$2.185\ (2.230) \pm 0.056$	$2.176\ (2.177) \pm 0.054$	$2.151\ (2.177) \pm 0.051$
n_s	$0.9686\ (0.9687) \pm 0.0044$	$0.9768\ (0.9828)^{+0.0065}_{-0.0072}$	$0.9812\ (0.9880) \pm 0.0080$	$0.9764\ (0.9795) \pm 0.0073$
$\tau_{\rm reio}$	$0.075\ (0.068) \pm 0.013$	$0.075\ (0.083) \pm 0.013$	$0.068\ (0.068) \pm 0.013$	$0.062\ (0.066) \pm 0.014$
$\mathrm{Log}_{10}(a_c)$	–	$-4.136\ (-3.728)^{+0.57}_{-0.013}$	$-3.737\ (-3.696)^{+0.110}_{-0.094}$	$-3.449\ (-3.509)^{+0.047}_{-0.11}$
$f_{\rm EDE}(a_c)$	–	$0.028\ (0.044)^{+0.011}_{-0.016}$	$0.050\ (0.058)^{+0.024}_{-0.019}$	$0.054\ (0.057)^{+0.031}_{-0.027}$
$r_s(z_{\rm rec})$	$145.05\ (145.1) \pm 0.26$	$141.4\ (139.8)^{+2}_{-1.5}$	$140.3\ (138.9)^{+1.9}_{-2.3}$	$141.6\ (141.3)^{+1.8}_{-2.1}$
S_8	$0.824\ (0.814) \pm 0.012$	$0.826\ (0.836) \pm 0.014$	$0.838\ (0.842) \pm 0.015$	$0.836\ (0.839) \pm 0.015$
H_0	$68.18\ (68.33) \pm 0.54$	$70.3\ (71.1) \pm 1.2$	$70.6\ (71.6) \pm 1.3$	$69.9\ (70) \pm 1.1$

Table 2.3: The mean (best-fit) $\pm 1\sigma$ error of the cosmological parameters reconstructed from our combined analysis in each model.

Chapter 3

Combining Cosmological Tensions

The simple ΛCDM concordance model has been immensely successful in describing numerous cosmological observables at different epochs [20, 166]. Nontheless, when fit to measurements of the early universe, the ΛCDM model finds results inconsistent with observations of the late universe [30]. These include the persistent Hubble tension [29] as well as the milder S_8 tension [31].

The current state-of-the-art experiment Planck which measures the cosmic microwave background (CMB) radiation, assumes a flat ΛCDM model to extract cosmological parameter values and finds the local expansion rate H_0 to be 67.37 ± 0.54 km/s/Mpc [25]. On the other hand, the SH0ES collaboration finds the larger value $H_0 = 73.52 \pm 1.62$ km/s/Mpc [83, henceforth R18] through model-independent measurements of the local universe, at $\gtrsim 3.5\sigma$ tension with the Planck value. [1] This tension between the early and late

[1] At the time this work was completed, the most precise local measurement of H_0 was from Ref. [83].

universe exists even without Planck CMB data or the SH0ES distance ladder [30]. Another direct measurement of $H_0 = 72.5^{+2.1}_{-2.3}$ km/s/Mpc [70] from the H0LiCOW collaboration based on lensing time delays is in moderate tension with Planck, while a constraint from Big Bang nucleosynthesis (BBN) combined with baryon acoustic oscillation (BAO) data of $H_0 = 66.98 \pm 1.18$ km/s/Mpc [30] is inconsistent with SH0ES.

There is also evidence of $\gtrsim 2\sigma$ tension between the constraints from Planck on the matter density Ω_m and the amplitude σ_8 of matter fluctuations in linear theory and those from local measurements [31, 32]. Planck derives $S_8 = \sigma_8(\Omega_m/0.3)^{0.5} = 0.832 \pm 0.013$ whereas local measurements find the smaller values: $S_8^{\rm SZ} = \sigma_8(\Omega_m/0.27)^{0.3} = 0.78 \pm 0.01$ from Sunyaev-Zeldovich cluster counts [33], $S_8 = 0.783^{+0.021}_{-0.025}$ from DES [34] and $S_8 = 0.745 \pm 0.039$ from KiDS-450 [35] weak-lensing surveys. The CFHTLenS weak-lensing survey also finds support for disagreement with Planck CMB predictions [167].

Although systematic causes for these discrepancies cannot entirely be ruled out, numerous potential systematics have been investigated and exonerated over the years while the tensions have persisted and worsened [25, 32, 42–46, 71]. Hence, we must consider the alternative - that the model-dependent results from the early universe are inconsistent with the model-independent measurements of the late universe because the ΛCDM model of cosmology is incorrect.

There have been numerous attempts at resolving these discrepancies via non-standard cosmological models [37,39,47,168,169, and references therein], however, most such attempts at solving the Hubble tension worsen the S_8 tension and vice-versa. Solutions to the Hubble

tension either reduce the size r_s of the sound horizon with an early-universe modification [27, 28, 72], or increase the angular diameter distance D_A to the CMB with new physics in the post-recombination universe. Then, to keep the locations of the peaks in the CMB fixed, H_0 increases, diminishing the tension. On the other hand, a solution to the S_8 tension would require either late-universe physics that leads to a suppression of the linear matter power spectrum or a decrease in the CMB-predicted value of Ω_m.

In this work, we tackle both requirements with a decaying dark matter (DDM) model which has a decay rate proportional to the Hubble rate. In this scenario, a fraction of dark matter density decays into dark radiation per Hubble time [170], with the effect being amplified close to the onset of matter domination. This leads to an increase in the expansion rate relative to ΛCDM around recombination, resulting in a decrease in r_s. Fits to the CMB then predict a higher H_0, alleviating the Hubble tension. Moreover, observables like the CMB fix the amount of dark matter in the early universe. Then, due to decay into dark radiation, there is less dark matter today, lowering Ω_m and leading to smaller S_8 values. This model can hence simultaneously diminish both the Hubble and the S_8 tensions. Testing against various cosmological datasets, we find that this DDM model can provide a better fit to some datasets and simultaneously alleviate the two aforementioned tensions, but not fully resolve them. We also find that at most, a fraction $f_{\rm dm} \lesssim 0.003$ of dark matter can decay into dark radiation in the light of recent Planck, supernova and BAO data, and an external prior on H_0 from R18. This chapter is organised as follows. A brief description of the model is given in Section 3.1, along with its effect on observables. In Section 3.2, we provide a detailed description of our analysis. Our results are presented in Section 3.3 and

discussed in Section 3.4 where we also conclude.

This chapter is based heavily on recent work [40] accomplished with co-authors Kanhaiya Pandey and Subinoy Das.

3.1 Decaying dark matter model

Motivation for exploring a DDM resolution to the Hubble tension comes from considering the effective radiation degrees of freedom $N_{\rm eff}$ [20, 25, 48]. Increasing the amount of radiation in the early universe such that $\Delta N_{\rm eff} \sim 0.4 - 1$ has been shown to diminish the Hubble tension [20]. This extra radiation must be 'dark' as the presence of an extra photon-like component is strongly constrained by both BBN and the CMB [22]. A fourth, massive, sterile neutrino could provide such extra dark radiation however, the existence of such a particle is constrained by oscillation experiments [171].

The scenario explored here follows the model proposed by Ref. [170]. It involves dark radiation interacting within the dark sector, in particular, a particle (beyond the framework of the standard model) decaying into an extra dark radiation component. All the dark radiation in this scenario is a product of dark matter decay and forms a small fraction of the total dark matter density. The decay rate Γ determines this fraction $f_{\rm dm}$ of dark matter energy density that decays into dark radiation. This fraction remains nearly constant over time after matter-radiation equality. If $f_{\rm dm}$ is large, it can alter the expansion rate as shown in Fig. 3.1, which we demonstrate leads to a higher predicted H_0. Moreover, the decay naturally reduces the amount of dark matter in galaxies and clusters leading

to smaller predicted values of S_8. A brief description of the background dynamics of the model, contribution of dark radiation to $N_{\rm eff}$ and effect on observables is discussed in the following subsections.

3.1.1 Background dynamics

A general coupling between dark matter and dark radiation can be described by the energy balance equations [172]

$$\dot{\rho}_{\rm dm} + 3H\rho_{\rm dm} = -Q \tag{3.1}$$

$$\dot{\rho}_{\rm dr} + 3H(1+w_{\rm dr})\rho_{\rm dr} = Q \tag{3.2}$$

where $\rho_{\rm dm}$ and $\rho_{\rm dr}$ are the dark matter and dark radiation energy densities and $H = \dot{a}/a$ is the Hubble rate, where a is the scale factor and overdots denote derivatives with respect to conformal time. We also assume dark radiation has an equation of state $w_{\rm dr} = P_{\rm dr}/\rho_{\rm dr} = 1/3$. A positive rate of energy transfer Q denotes the direction of energy transfer from dark matter to dark radiation. Non-zero values of Q imply that dark matter no longer redshifts exactly as a^{-3} nor dark radiation as a^{-4}. We adopt the covariant form of the energy-momentum transfer 4-vector introduced in [172]

$$Q = \Gamma\rho_{\rm dm}, \tag{3.3}$$

where the exact form of the interaction rate Γ depends on the details of the particle physics of the decay process.

Many forms of Γ have been studied in the literature [168, 173–176]. Here, we explore the simple case where $\Gamma = \alpha H$, where α is a constant and H is the Hubble rate. Although we do not model the particle physics resulting in $\Gamma \propto H$, we refer the reader to two fundamental particle physics motivations for such an interaction. As discussed in Section 5 of Ref. [170], if dark matter is a coherently oscillating scalar field and decays into light fermions similar to the reheating mechanism, it can give rise to our DDM set up. It may also arise in the model proposed by Ref. [177], where a fraction of dark matter converts to dark radiation through late kinetic decoupling and Sommerfeld-enhanced dark matter annihilation. The mass ranges for dark matter particles in each of these models differ greatly. As our analysis here is phenomenological, our constraints are independent of the mass of the dark matter particle undergoing decay. Interpreting these results in the framework of a particular fundamental model can translate our constraints to particle mass and interaction cross-section.

For $\Gamma = \alpha H$, the background evolution is readily solved

$$\rho_{\rm dm} = \rho_{\rm dm,0} a^{-(3+\alpha_{\rm dr})} \tag{3.4}$$

$$\rho_{\rm dr} = \rho_{\rm dr,0} a^{-3(1+w_{\rm dr})} + \frac{\alpha_{\rm dr}}{\alpha_{\rm dr} - 3w_{\rm dr}} \rho_{\rm dm,0} a^{-3} (a^{-3w_{\rm dr}} - a^{-\alpha_{\rm dr}}), \tag{3.5}$$

where the subscript 0 denotes values today. For $w_{\rm dr} = 1/3$, (3.5) can be further simplified to

$$\rho_{\rm dr} = \beta a^{-4} + \frac{\alpha_{\rm dr}}{1 - \alpha_{\rm dr}} \rho_{\rm dm,0} a^{-(3+\alpha_{\rm dr})}, \tag{3.6}$$

where β is a constant. The first term in (3.6) behaves like a standard radiation density

while the second behaves like a fluid with an equation of state $\alpha_{\rm dr}/3$. For weak couplings between dark matter and dark radiation, $\alpha_{\rm dr} \ll 1$, which leads to $\beta \sim \rho_{\rm dr,0}$. Assuming no dark radiation exists initially, we set $\beta = 0$ and only retain the second term in our analysis. With this assumption, we obtain the fraction $f_{\rm dm}$ of dark matter that decays into dark radiation

$$f_{\rm dm} = \frac{\rho_{\rm dr}}{\rho_{\rm dm}} \to \frac{\alpha_{\rm dr}}{3w_{\rm dr} - \alpha_{\rm dr}} = \frac{\alpha_{\rm dr}}{1 - \alpha_{\rm dr}} \simeq \alpha_{\rm dr}. \tag{3.7}$$

Therefore, $f_{\rm dm}$ is constant over time and the density of dark radiation $\rho_{\rm dr} \simeq \alpha_{\rm dr}\rho_{\rm dm}$. Our model is then parameterised by a single parameter $\alpha_{\rm dr}$.

For a detailed description of the perturbations in our model, we refer the reader to Ref. [170, 178].

3.1.2 Calculation of $\Delta N_{\rm eff}$

In standard cosmology, the energy density $\rho_{\rm rad}$ of relativistic species in terms of the photon energy density ρ_γ is

$$\rho_{\rm rad} = \left[1 + \frac{7}{8} N_{\rm eff} \left(\frac{4}{11}\right)^{4/3}\right] \rho_\gamma. \tag{3.8}$$

This includes standard model (SM) neutrinos (for which $N_{\nu,\rm eff} = 3.046$) [179], and characterizes any free-streaming radiation beyond the SM expectation. Then, any departure from the SM can be accounted for through $\Delta N_{\rm eff}$, where $N_{\rm eff} = N_{\nu,\rm eff} + \Delta N_{\rm eff}$. In our case,

$\Delta N_{\rm eff,dr}$ can be expressed in terms of $\alpha_{\rm dr}$ [170] as

$$\frac{7}{8}\Delta N_{\rm eff,dr}\left(\frac{4}{11}\right)^{4/3}\frac{\rho_{\gamma,0}}{a^4} = \frac{1}{1-\alpha_{\rm dr}}\rho_{\rm dm,0}a^{-(3+\alpha_{\rm dr})} - \rho_{\rm dm,0}a^{-3}, \tag{3.9}$$

making it a derived parameter in our analysis.

3.1.3 Effects on observables

The main effect of the DDM model is an alteration of the expansion history of the Universe. In Fig. 3.1, we show how decaying dark matter affects the CMB, the matter power spectrum and the expansion rate. All parameters were fixed at their Planck 2015 ΛCDM best-fit values, including the energy density $\Omega_{\rm dm,0}$ of dark matter today, and we show the effect of varying just $\alpha_{\rm dr}$. Then, for $\alpha_{\rm dr} > 0$, there was more dark matter in the early universe which decayed to match the dark matter energy density today. This shifts matter-radiation equality to earlier times, reduces the ratio $\Omega_{\rm b}/\Omega_{\rm dm}$ of baryons to dark matter in the early universe and elongates the matter-dominated epoch of the Universe.

The bottom-right panel of Fig. 3.1 can then be understood as follows. At early times, the Universe is radiation-dominated and the Hubble rate H is given by

$$3H^2M_{\rm Pl}^2 = \left[1+\frac{7}{8}N_{\nu,\rm eff}\left(\frac{4}{11}\right)^{4/3}\right]\rho_\gamma + \frac{1}{1-\alpha_{\rm dr}}\rho_{\rm dm,0}a^{-(3+\alpha_{\rm dr})} + \rho_{\rm b,0}a^{-3}. \tag{3.10}$$

Here, M_{Pl} is the reduced Planck mass and $\rho_{\rm b,0}$ is the baryon density today. The dark radiation added by the DDM model is always subdominant, and the very early universe resembles a ΛCDM universe. As we approach matter domination, due to the extra dark

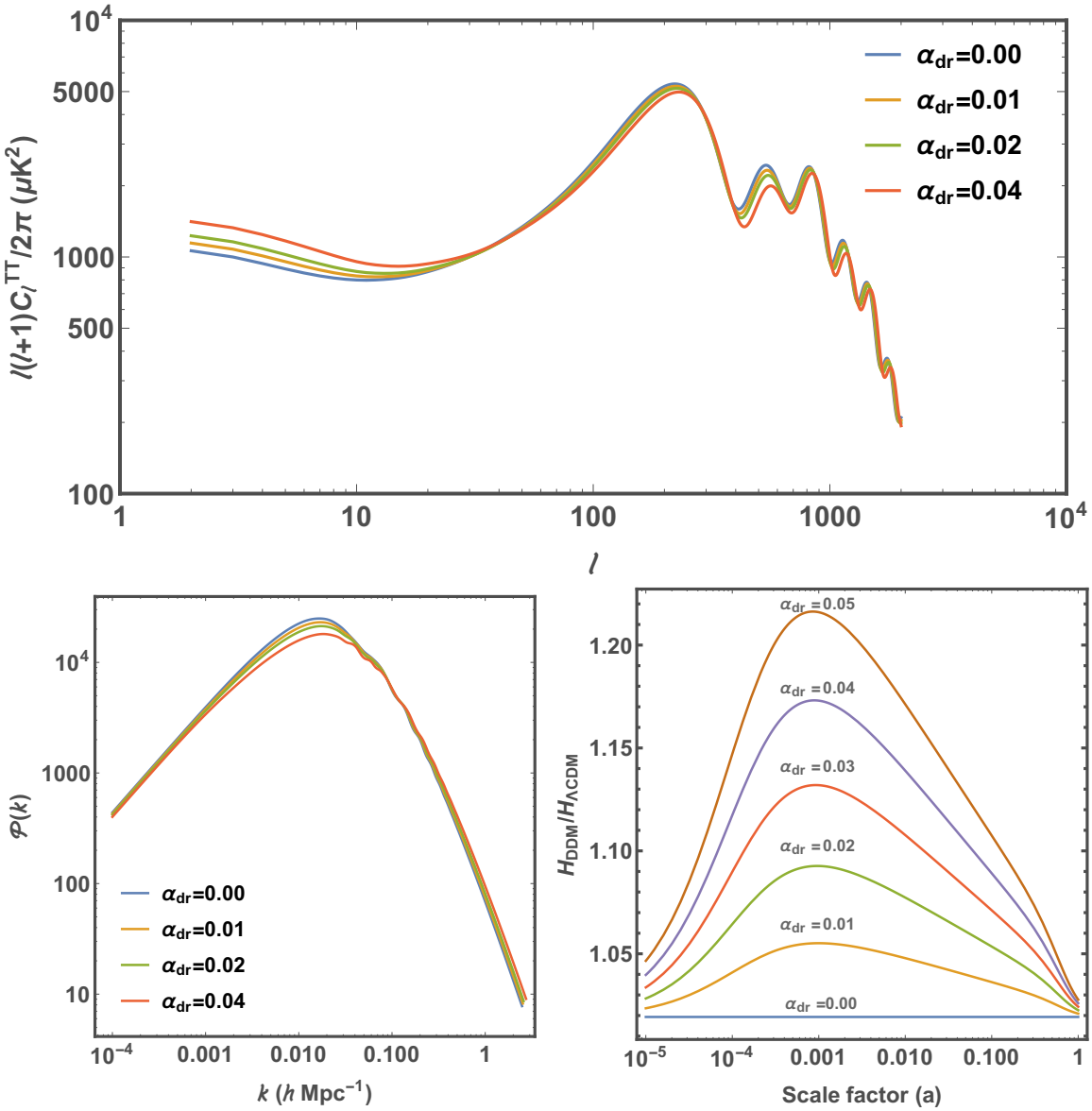

Figure 3.1: Shown here are the effects of DDM on various observables. These plots were produced using a modified version of CAMB, fixing all ΛCDM parameters, including $\Omega_{\mathrm{dm},0}$ and varying just α_{dr}. The blue line with $\alpha_{\mathrm{dr}} = 0$ represents a ΛCDM cosmology. *Top*: effect of non-zero α_{dr} on the CMB TT power spectrum; *Left*: effect on the matter power spectrum; *Right*: the DDM expansion rate relative to ΛCDM.

matter in the Universe, the expansion rate increases, reaching a peak deviation close to $z \sim 10^3$. Finally, as the extra dark matter decays into dark radiation which quickly redshifts away, the expansion rate relaxes back into agreement with ΛCDM. This effect is more pronounced as $\alpha_{\rm dr}$ increases. Overall, the expansion rate is increased in the DDM scenario relative to ΛCDM, the maximum increase occuring close to recombination. This combined with extra dark matter in the early universe shifts matter-radiation equality as well as recombination to earlier. If recombination occurs earlier, sound waves in the early universe have less time to travel, decreasing the sound horizon r_s. The Hubble parameter can then increase to compensate allowing the DDM model to diminish the Hubble tension.

These effects can also be inferred from the top panel of Fig. 3.1 showing the change in the CMB TT power spectrum. An increase in the amount of dark matter in the early universe suppresses power in all CMB peaks, as the enhancement due to acoustic driving is reduced. A smaller sound horizon shifts peak locations to smaller scales, or larger multipoles ℓ. The effect of the reduced ratio $\Omega_{\rm b}/\Omega_{\rm dm}$ is most apparent in the second peak. The heights of odd and even CMB peaks determine $\Omega_{\rm b}/\Omega_{\rm dm}$, with a smaller ratio implying a larger difference in peak heights [180]. Finally, power at large scales ($\ell \lesssim 30$) is enhanced because dark matter decaying into dark radiation causes gravitational potential wells to decay, boosting the late integrated Sachs-Wolfe (ISW) effect.

Similar effects can also be seen in the matter power spectrum shown in the bottom-left panel of Fig. 3.1. The location of the peak in the matter power spectrum is dictated by the size of the Universe at matter-radiation equality, which the DDM model shifts to smaller sizes, or larger wavenumbers $k_{\rm eq}$ [181]. The enhancement of power at small scales is a result

of the decrease in $\Omega_{\rm b}/\Omega_{\rm dm}$, which leads to less photon drag and boosts structure formation. On the other hand, large-scale modes enter the horizon in the late universe which has less dark matter than the early universe, but is still expanding faster than ΛCDM as seen form Fig. 3.1. This suppresses structure formation and therefore power at large scales. In particular, at scales $\sim$ 8Mpc, power is considerably suppressed, alleviating the S_8 tension. This suppression can also be attributed to DDM causing gravitational potential wells to decay, becoming shallower in the late universe. Moreover, as DDM dilutes as $a^{-(3+\alpha)}$, it is no longer pressureless and this pressure resists the growth of gravitational potential wells.

3.2 Methodology

To investigate this DDM model, we use a modified version of the publicly available Boltzmann code `CAMB` [182]. The modified version is based on the dynamics described in [170]; We vary the 6 standard ΛCDM parameters: the baryon density $\omega_{\rm b}$ today, the dark matter density $\omega_{\rm dm}$ today, the angular size $\theta_{\rm MC}$ of the sound horizon at recombination, the optical depth τ to reionisation, the scalar spectral index $n_{\rm s}$, and the amplitude $A_{\rm s}$ of the primordial power spectrum. To this, we add the DDM parameter $\alpha_{\rm dr}$. We then use the publicly available Markov chain Monte Carlo code `CosmoMC` [183] to explore our 7-dimensional parameter space with the following assumptions. We assume a flat universe with $\Omega_k = 0$, a constant dark energy equation of state, $w_{\rm de} = -1$ and fix the running of the scalar spectral index $dn_{\rm s}/d\ln k = 0$. We adopt standard values for the sum of neutrino masses $\Sigma m_\nu = 0.06$ eV and the SM $N_{\nu,\rm eff} = 3.046$. The entire DDM model is described by the sole parameter $\alpha_{\rm dr}$. The dark radiation energy density $\Omega_{\rm dr}$ and $\Delta N_{\rm eff,dr}$ are derived

parameters which can be expressed in terms of $\alpha_{\rm dr}$. Table 3.1 shows the priors for the 7 varied parameters.

We fit to various early and late-universe data sets in certain combinations. Our data include:

- **Planck :** The CMB temperature and polarization angular power spectra (high-ℓ TT + low-ℓ TEB) released by Planck 2015 [22, 153]
- **JLA :** Luminosity distance of supernovae Type Ia coming from 'joint light-curve analysis' using SNLS (Supernova Legacy Survey) and SDSS (Sloan Digital Sky Survey) catalogs [130]
- **BAO :** The 'Baryonic Acoustic Oscillation' data from DR12-BAO [81], SDSS-6DF [17] and SDSS-MGS [80]
- **R18 :** An external gaussian prior on $H_0 = 73.52 \pm 1.62$ km/s/Mpc [83].

We fit to the combinations Planck, Planck+R18 and Planck+JLA+BAO+R18. We adhere to the Gelman-Rubin convergence criteria of $R - 1 < 0.01$ and discard the first 30% of our chains as burn-in.

3.3 Results

Figures 3.2-3.4 compare our posteriors for the ΛCDM (blue) and DDM (red) models for various data sets. Along with posteriors for $\Omega_b h^2$, $\Omega_{dm} h^2$ and $\alpha_{\rm dr}$, we also show posteriors for the derived parameters H_0 and S_8. The green bands represent local measurements of

Parameter	ΛCDM	DDM
$\Omega_b h^2$	[0.005 , 0.1]	[0.005 , 0.1]
$\Omega_{dm} h^2$	[0.001 , 0.99]	[0.001 , 0.99]
$100\theta_{MC}$	[0.5 , 10]	[0.5 , 10]
τ	[0.01 , 0.8]	[0.01 , 0.8]
n_s	[0.8 , 1.2]	[0.8 , 1.2]
$\ln(10^{10} A_s)$	[2.0 , 4.0]	[2.0 , 4.0]
$\alpha_{\rm dr}$	–	[0.00 , 0.05]

Table 3.1: Priors on the cosmological parameters we vary in our MCMC analyses

H_0 and S_8. From these figures, the correlation of H_0 with $\alpha_{\rm dr}$ and the anticorrelation of S_8 with $\alpha_{\rm dr}$ are apparent. An increase in $\alpha_{\rm dr}$ results in a greater H_0 and a smaller S_8. This is the exact effect required to solve the H_0 and S_8 tensions simultaneously. These correlations are most evident in the posteriors of Planck+R18 in Fig. 3.3. The inclusion of BAO data diminishes these correlations as seen in Fig. 3.4.

As seen from Fig. 3.2, Planck data places an upper bound on $\alpha_{\rm dr}$ (≤ 0.003). However, the addition of an external prior on H_0 from R18 leads to a small preference for non-zero $\alpha_{\rm dr}$ ($\approx 0.005 \pm 0.003$) at the $\sim 1.5\sigma$ level. With Planck+R18, the Hubble tension is reduced to $\sim 1.5\sigma$ and the S_8 tension to $\sim 0.3\sigma$. The addition of BAO data weakens these resolutions, as seen form Table 3.2. For Planck+JLA+BAO+R18, the H_0 and S_8 tensions remain at $\sim 2.5\sigma$ and $\sim 1.5\sigma$ levels respectively. For all dataset combinations explored, we remain consistent with ΛCDM within 1σ for all ΛCDM parameters.

Table 3.3 shows the best-fit χ^2 values for the ΛCDM and DDM models. The DDM model leads to a slight improvement in fit, largely due to fitting the R18 measurement better than ΛCDM.

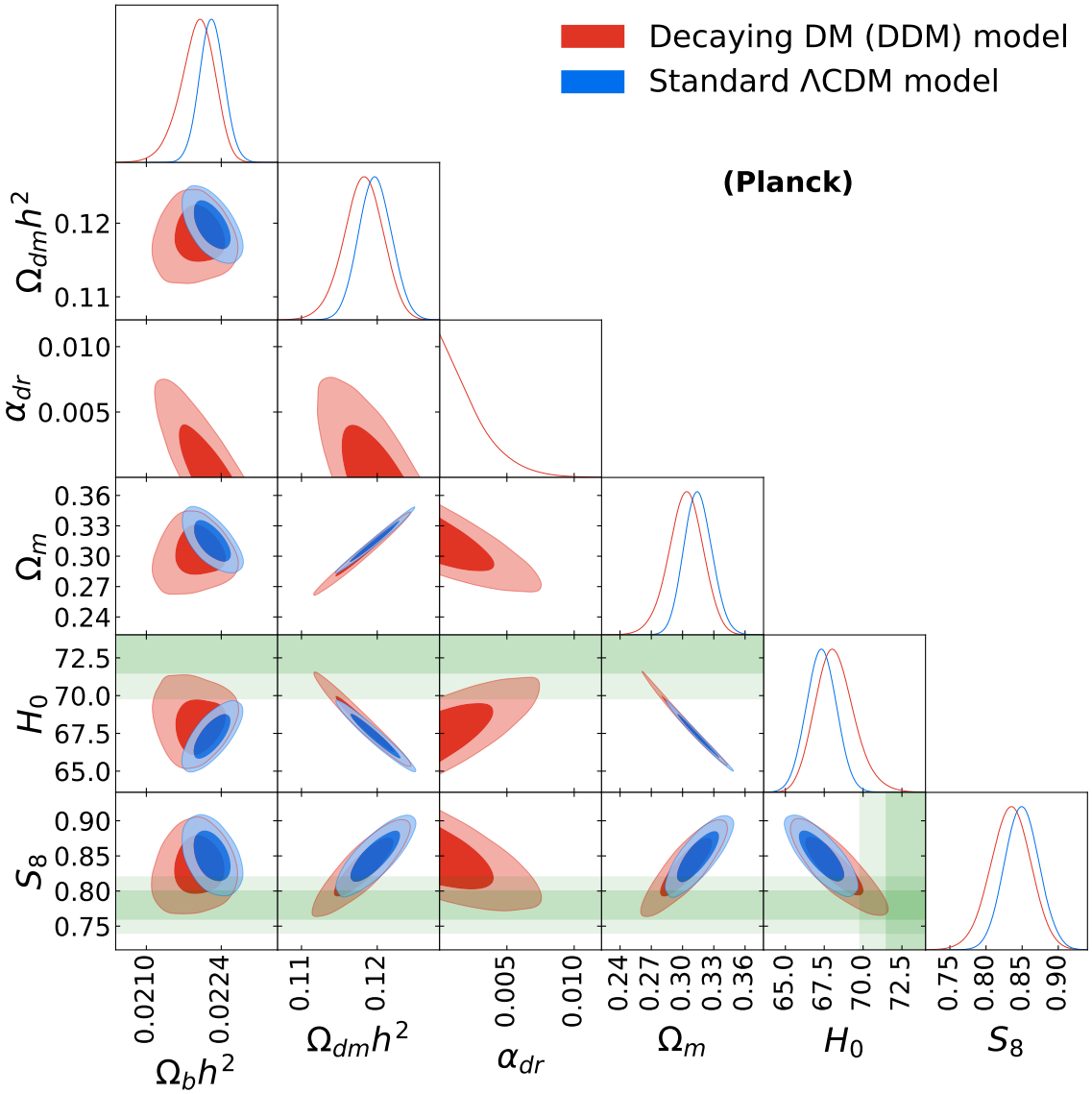

Figure 3.2: Comparison between the standard ΛCDM and the DDM models: Constraints on various cosmological parameters along with their covariances when tested against the Planck data. The green bands represent the constraints on H_0 and S_8 coming from [83, R18] and [34, DES-YI, 2017].

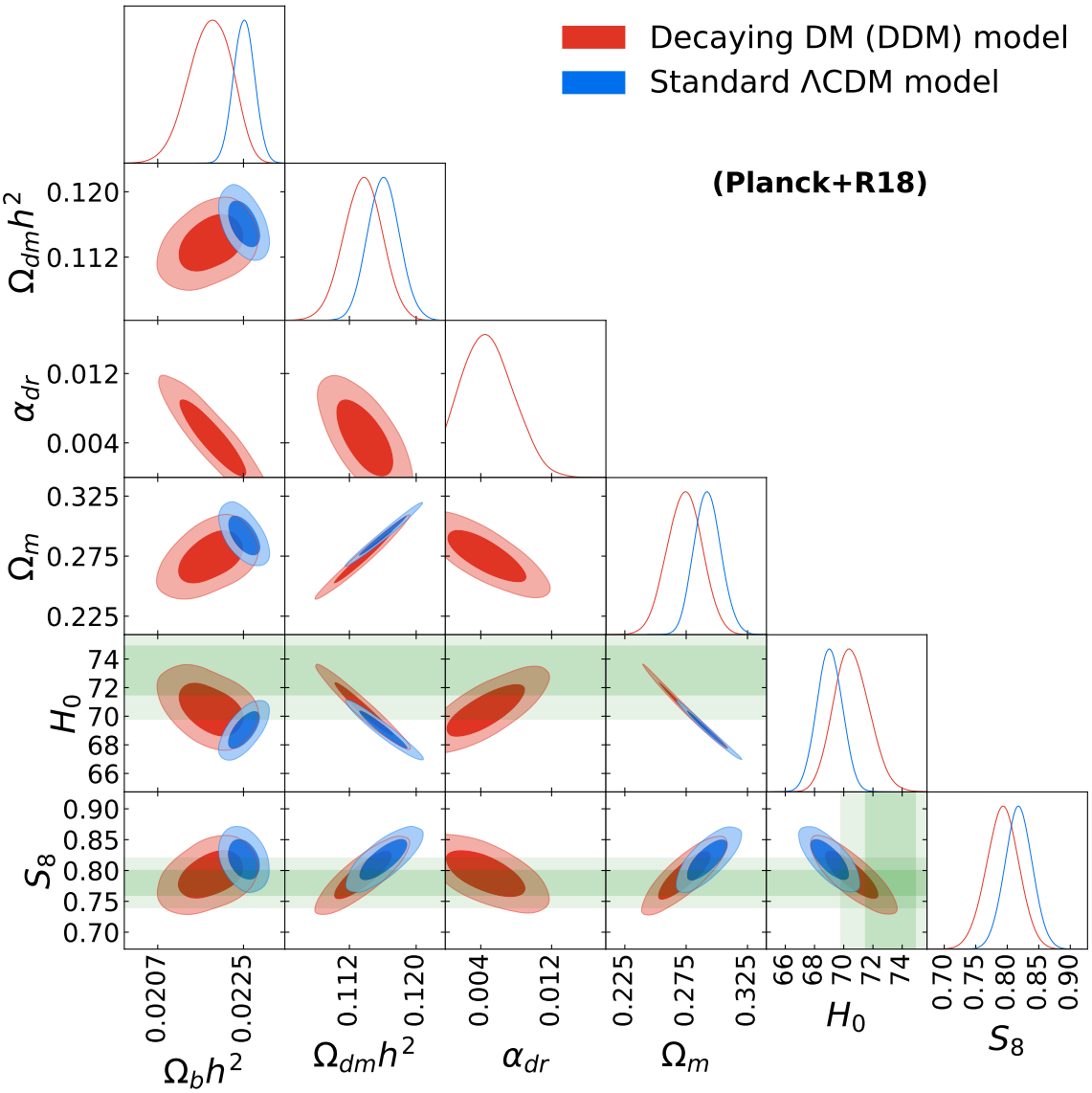

Figure 3.3: Comparison between the standard ΛCDM and the DDM models: Constraints on various cosmological parameters along with their covariances when tested against the Planck+R18. The green bands represent the constraints on H_0 and S_8 coming from [83, R18] and [34, DES-YI, 2017].

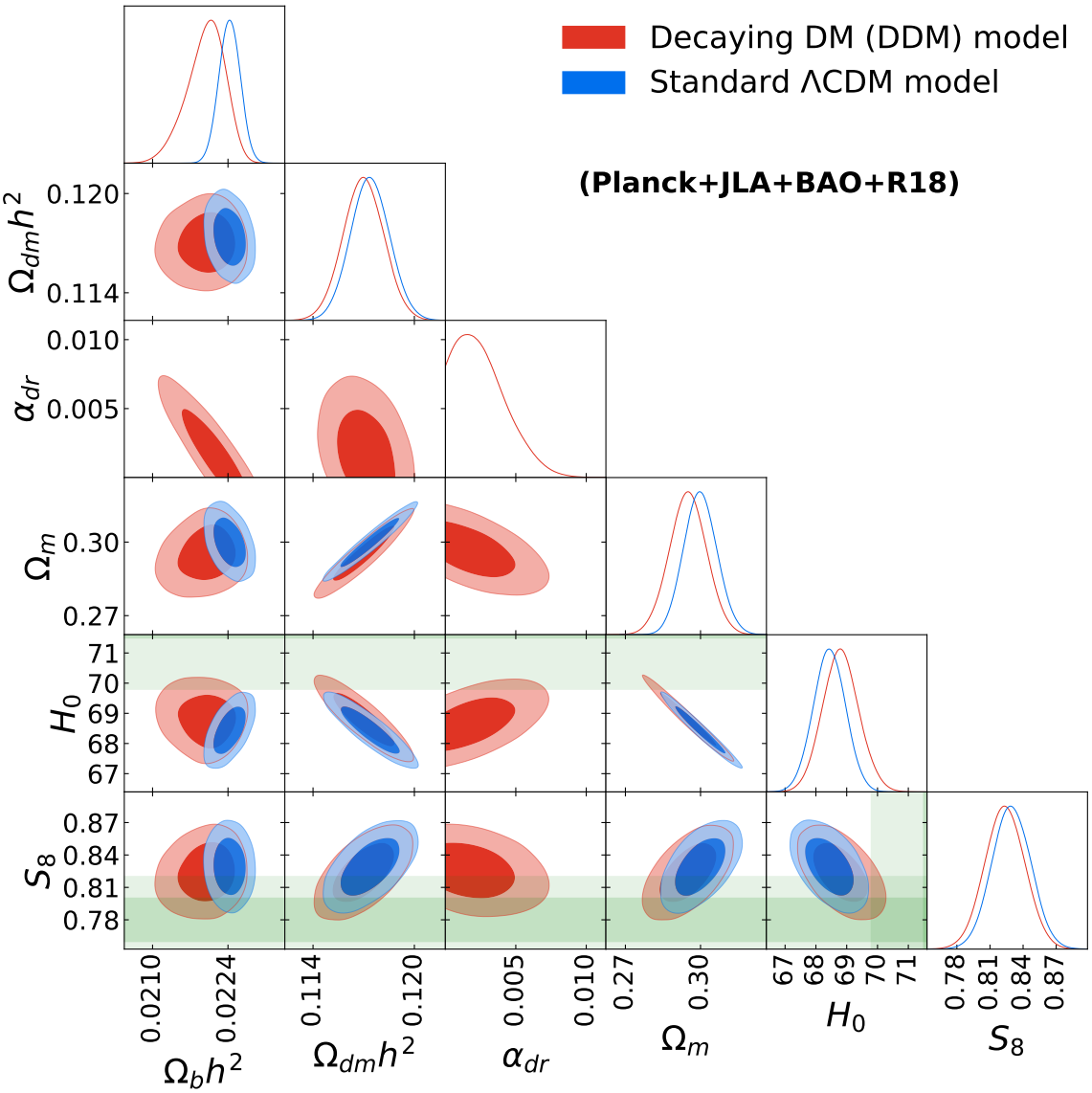

Figure 3.4: Comparison between the standard ΛCDM and the DDM models: Constraints on various cosmological parameters along with their covariances when tested against the Planck+JLA+BAO+R18. The green bands represent the constraints on H_0 and S_8 coming from [83, R18] and [34, DES-YI, 2017].

In Fig. 3.5, we show how the decay parameter $\alpha_{\rm dr}$ improves the H_0 and S_8 tensions. In the DDM scenario (red contours), $\alpha_{\rm dr}$ increases towards the bottom right. Considering just Planck+R18, the external prior on H_0 pushes the decay rate of dark matter to be $\sim 1\%$ of the Hubble rate. These large values of $\alpha_{\rm dr}$ alter expansion history enough for the model to predict a larger H_0 as well as predict a lower Ω_m and therefore lower S_8. Without data at intermediate redshifts, such large changes in cosmology are permitted. As seen from the top panel of Fig. 3.5, within the scope allowed by Planck+R18, the DDM contours intersect the 1σ local-measurement square (green). For these datasets, while the 1σ ΛCDM contour (blue) intersects the 1σ local measurement of S_8, the 2σ ΛCDM contour is beyond the 1σ local H_0 measurement. Therefore, the DDM model diminishes the H_0 and S_8 tensions.

Including data at intermediate redshifts, namely JLA and BAO, the tensions remain unresolved. As seen from the bottom panel of Fig. 3.5, while DDM nearly resolves the S_8 tension, the Hubble tension still exists. The combined datasets Planck+R18+JLA+BAO do not permit large deviations from ΛCDM cosmology. Moreover, smaller values of $\alpha_{\rm dr}$ are permitted, with the decay rate of dark matter constrained to be $\sim 0.5\%$ of the Hubble rate.

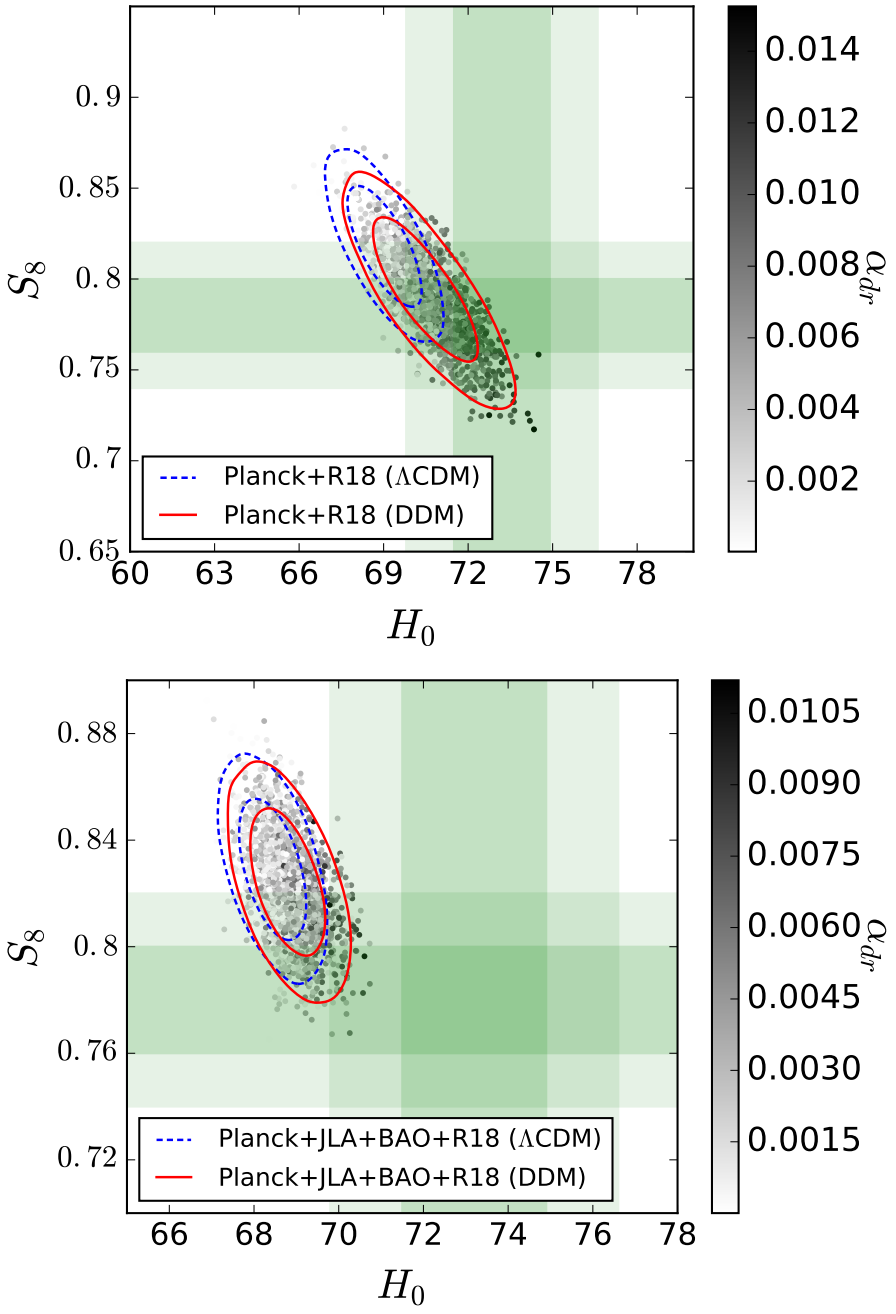

Figure 3.5: The figures show the ΛCDM (blue) and DDM (red) constraints on the $H_0 - S_8$ plane for two dataset combinations, Planck+R18 and Planck+R18+JLA+BAO. The green bands represent the 1 and 2 σ constraints on H_0 and S_8 coming from [83, R18] and [34, DES-YI, 2017]. The scattered points are for the DDM model representing values of $\alpha_{\rm dr}$.

	Planck+R18		Planck+JLA+BAO+R18	
Parameter	ΛCDM	DDM	ΛCDM	DDM
$\Omega_b h^2$	0.02251 ± 0.00022	$0.02180^{+0.00049}_{-0.00041}$	0.02243 ± 0.00020	$0.02199^{+0.00041}_{-0.00029}$
$\Omega_{dm} h^2$	0.1161 ± 0.0019	0.1136 ± 0.0023	0.1174 ± 0.0012	0.1170 ± 0.0012
$100\theta_{MC}$	1.04138 ± 0.00045	1.04118 ± 0.00045	1.04123 ± 0.00041	1.04098 ± 0.00044
τ	0.094 ± 0.019	0.089 ± 0.020	0.089 ± 0.018	0.082 ± 0.019
$\ln(10^{10} A_s)$	3.113 ± 0.037	3.107 ± 0.038	3.106 ± 0.035	3.096 ± 0.037
n_s	0.9748 ± 0.0058	0.9763 ± 0.0058	0.9715 ± 0.0043	0.9699 ± 0.0044
$\alpha_{\rm dr}$	$--$	$0.0050^{+0.0023}_{-0.0034}$	$--$	< 0.00332
Ω_m	0.293 ± 0.011	0.274 ± 0.014	0.3000 ± 0.0067	0.2950 ± 0.0074
Ω_Λ	$0.707^{+0.012}_{-0.010}$	0.725 ± 0.014	0.7000 ± 0.0067	0.7044 ± 0.0073
σ_8	0.829 ± 0.015	0.830 ± 0.015	0.830 ± 0.015	0.831 ± 0.015
S_8	0.818 ± 0.022	0.793 ± 0.026	0.829 ± 0.018	0.823 ± 0.018
H_0	69.03 ± 0.87	$70.6^{+1.1}_{-1.3}$	68.44 ± 0.52	68.81 ± 0.58

Table 3.2: Comparison between the standard ΛCDM and the DDM models showing 1σ constraints on parameters fitting to Planck+R18 and Planck+JLA+BAO+R18

	Plank+R18		Plank+JLA+BAO+R18	
Dataset	ΛCDM	DDM	ΛCDM	DDM
$\chi^2_{\mathrm{high}\ell\mathrm{TT}}$	768.352	771.684	767.395	767.154
χ^2_{lowTEB}	10498.3	10496.5	10497.3	10497.9
χ^2_{JLA}	$--$	$--$	695.377	695.299
χ^2_{6DF}	$--$	$--$	0.0402244	0.0793526
χ^2_{MGS}	$--$	$--$	2.34994	2.67358
$\chi^2_{\mathrm{DR12BAO}}$	$--$	$--$	3.57457	3.96993
$\chi^2_{\mathrm{nuisance}}$	1.50061	3.20412	3.11594	2.42671
χ^2_{R18}	7.59589	2.46971	9.11007	7.98282
$\sum \chi^2_{\mathrm{i}}$	11275.7	11273.8	11978.3	11977.5
$\Delta(\sum \chi^2_{\mathrm{i}})$	0	-1.9	0	-0.8

Table 3.3: Comparison between the standard ΛCDM and the DDM models: χ^2 values for various datasets from a combined fit to Planck+R18 and Planck+JLA+BAO+R18 are given, with the $\chi^2_{\mathrm{nuisance}}$ for expectations for the nuisance and foreground parameters.

3.4 Discussion and conclusions

While the ΛCDM model of cosmology fits numerous datasets well, its predictions based on the early and late universe disagree [30, 72]. The current expansion rate H_0 is underpredicted by ΛCDM when fit to the early universe [25]. Despite this, measurements of the late universe are in agreement with a ΛCDM expansion history, but with different parameter values [20]. This Hubble tension has persisted and worsened over the years and no systematic cause has yet been found [29]. Moreover, ΛCDM overpredicts the amplitude of matter fluctuations S_8 relative to direct measurements in the late universe [31, 32]. Although this is a milder tension, combined, these tensions might hint new physics beyond the standard model of cosmology.

Theories that address each tension often worsen the other. In this work, we explored a decaying dark matter model than can simultaneously improve both tensions. We considered

dark matter that decays into dark radiation, parameterised by a single new parameter [170,172]. The DDM model increases the expansion rate relative to ΛCDM, with the largest effect being close to recombination. This leads to a reduced sound horizon, to compensate for which H_0 increases, alleviating the Hubble tension. The DDM model also reduces the dark matter density in the late universe, suppressing structure formation and lowering the predicted value of S_8. Hence, it offers solutions to both tensions simultaneously.

Considering just data from the early and current universes, that is the Planck+R18 combination, we find that the Hubble tension is reduced below the 1.5σ level and the S_8 tension below 0.5σ. DDM not only significantly diminishes both tensions, but also provides a slightly better fit to these datasets with $\Delta\chi^2_{\rm tot} = -1.9$, as seen from Table 3.3. However, including measurements of the Universe at intermediate redshifts with Planck+R18+JLA+BAO, we find that the DDM model is strongly constrained and the H_0 and S_8 tensions persist at the $\sim 2.5\sigma$ and $\sim 1.5\sigma$ levels respectively. The DDM model alters expansion history relative to ΛCDM all through matter domination, as shown in Fig. 3.1. As found by numerous models that aim to resolve the Hubble tension through modifications of the late universe, late-universe datasets such as BAO and JLA strongly constrain expansion history and keep such models from fully resolving the Hubble tension [25,47]. In this case, the "new physics" we add is present not only in the early universe where it has maximal effect, but throughout cosmic history. Its presence in the late universe would spoil the fits to BAO and JLA, keeping it from diminishing the H_0 and S_8 tensions further. This can also be seen from the tilt of the H_0 and S_8 vs $\alpha_{\rm dr}$ contours in Figs. 3.3 and 3.4. Without BAO and JLA data, $\alpha_{\rm dr}$ has a stronger correlation with H_0 and anticorrelation with S_8 in Fig. 3.3. This relaxes

when intermediate-redshift datasets are added as in Fig. 3.4, implying that the addition of BAO and JLA data weakens the effectiveness of DDM at resolving both tensions.

Numerous models of dark matter interacting within the dark sector have been explored [184–187]. In these models, the interaction is effective only up to a certain scale and negligible at larger scales. This produces a cut-off-like feature in the matter power spectrum at small scales, keeping the power in scales $\sim$ 8Mpc the same as in ΛCDM. For decaying dark matter with a constant time-independent decay rate [168, 173], the constraints are driven by the change to the late ISW effect on the large-scale CMB data. To be consistent with it, the dark matter must decay very slowly which only allows a slight improvement in the S_8 tension. The DDM model considered here circumvents this by having a smaller decay rate in the early universe around decoupling which then increases with time. Models which introduce a time-dependent dark-matter drag force due to dark radiation which also shut-off at late times [175] have similar effects.

The S_8 and Hubble tensions are intriguing results in cosmology. They require careful investigation whether from a systematic or a new-physics perspective. Future data may shed further light on whether these anomalies are hints of physics beyond the standard model of cosmology after all.

Chapter 4

Generalised Dark Matter

The generalised dark matter (GDM) formalism generalizes dark matter and dark energy to fluids that have pressure, pressure waves and viscosity [53]. This phenomenological model describes the behaviour of dark matter by three parameters: the equation of state parameter $w_{\rm g}$, which relates the pressure of a species to its energy density; the effective sound speed $c^2_{\rm eff}$, which quantifies the speed of pressure waves in the fluid; and $c^2_{\rm vis}$, which quantifies the viscosity of the fluid and hence the damping of these pressure waves. CDM has no pressure, pressure waves or viscosity, i.e. $w_{\rm g} = 0, c^2_{\rm eff} = 0, c^2_{\rm vis} = 0$. The cosmological constant has negative pressure, but no perturbations, hence $w_{\rm g} = -1, c^2_{\rm eff} = 0, c^2_{\rm vis} = 0$. Evidently, the CDM and Λ descriptions of dark matter and dark energy are therefore too rigid to reflect our uncertainty about the dark sector. Too little is known about dark energy and dark matter to assume that their properties remain constant over time.

The GDM formalism expands on the basic ΛCDM model by permitting these three

parameters to differ from their fixed ΛCDM values and vary in time [188]. This evolution can be entirely unconstrained, such that GDM is model-independent and data-driven. Alternatively, the GDM properties can be fixed at certain constant values or fixed to evolve in a manner to track the effects of a particular particle-physics theory of the dark sector. In this way, cold, warm and hot dark matter, neutrinos and massive neutrinos, a cosmological constant and scalar fields like our EDE can all be modelled using GDM [38, 53]. Hence GDM is a flexible, and therefore, powerful formalism to investigate the behaviour of dark matter and dark energy over cosmic history. In this framework, dark matter and dark energy may alter their properties over time, changing how the Universe evolves and how matter clusters [53, 189]. It hence forms an interesting approach to the σ_8 problem. As for the Hubble tension, my research already employs the GDM formalism for the fluid approximation of the EDE scenario proposed in Ch. 2.

Lastly, constraints placed on models of dark energy or dark matter that arise from fundamental theory are specific to that particular model. A phenomenological approach like GDM places broader constraints on the behavior of dark energy and dark matter over time, and their effect on data. Multiple fundamental models can fit into phenomenological constraints, making this approach more powerful.

The GDM formalism is outlined in §4.1 for completeness. For a detailed explanation, see Ref. [53]. Future applications of this framework are briefly described in §4.2.

4.1 GDM Dynamics

4.1.1 Background dynamics

The energy density ρ_g of GDM can be determined as a function of time by integrating

$$\frac{\dot{\rho}_g}{\rho_g} = -3(1+w_g)\frac{\dot{a}}{a} \tag{4.1}$$

where dots represent derivatives with respect to conformal time. For CDM, $w_g = 0$. Increasing w_g would make the energy density of GDM dilute faster than CDM, while $w_g < 0$ would make this energy density dilute slower. Allowing w_g to vary alters the expansion history of the Universe, the effects being exaggerated during matter domination. At the background level, Eq. (4.1) captures the entire contribution of GDM to the Universe.

4.1.2 Perturbation evolution

GDM also develops density (δ_g) and velocity (θ_g) perturbations, as well as anisotropic stress perturbations (σ_g). In the notation of [190], in the synchronous gauge, these evolve as

$$\begin{aligned}
\dot{\delta}_g &= -(1+w_g)\left(\theta_g + \frac{\dot{h}}{2}\right) - 3\frac{\dot{a}}{a}(c_{eff}^2 - w_g)\delta_g \\
&\quad -9\left(\frac{\dot{a}}{a}\right)^2 (c_{eff}^2 - c_g^2)(1+w_g)\frac{\theta_g}{k^2} \\
\dot{\theta}_g &= -(1-3c_{eff}^2)\frac{\dot{a}}{a}\theta_g + \frac{c_{eff}^2}{1+w_g}k^2\delta_g - k^2\sigma_g \\
\dot{\sigma}_g &= \frac{\dot{w}_g}{w_g(1+w_g)}\sigma_g - 3\frac{\dot{a}}{a}\sigma_g + \frac{8}{3}\frac{c_{vis}^2}{1+w_g}(\theta_g + \frac{\dot{h}}{2} + \frac{\dot{\eta}}{3}) \ ,
\end{aligned} \tag{4.2}$$

where k is the wavenumber of the perturbation mode and h and η are the metric perturbations in the synchronous gauge. The adiabatic sound speed c_g^2 of GDM perturbations can be calculated as in Eq. (2.27),

$$c_g^2 = \frac{\dot{P}_g}{\dot{\rho}_g} = w_g - \frac{\dot{w}_g}{3(1+w_g)} \left(\frac{\dot{a}}{a}\right)^{-1} . \tag{4.3}$$

Finally, GDM perturbations need initial conditions, which we currently base on Ref. [135] as

$$\begin{aligned} \delta_g &= \frac{3}{4}(1+w_g)\delta_\gamma \\ \theta_g &= 3w_g\theta_\nu \\ \sigma_g &= 3w_g\sigma_\nu \ , \end{aligned} \tag{4.4}$$

where δ_γ is the initial photon density perturbation, θ_ν denotes the initial neutrino velocity perturbation and σ_ν the initial anisotropic neutrino stress.

These are the GDM dynamics I have implemented in the Boltzmann solver CLASS [54] which calculates expected CMB and matter power spectra as well as other observables given a cosmology, eg. ΛCDM. Functionality allows for the GDM parameters to be free functions of redshift. A similar implementation of GDM was used for the fluid approximation to ULAs and EDE in Chapter 2. For more details, see §2.2.1 and Ref. [38].

4.1.3 Effect on the CMB

Intuitively, it is easier to understand the effects of varying the GDM parameters on observables if they are constant. Any species with a constant equation of state parameter

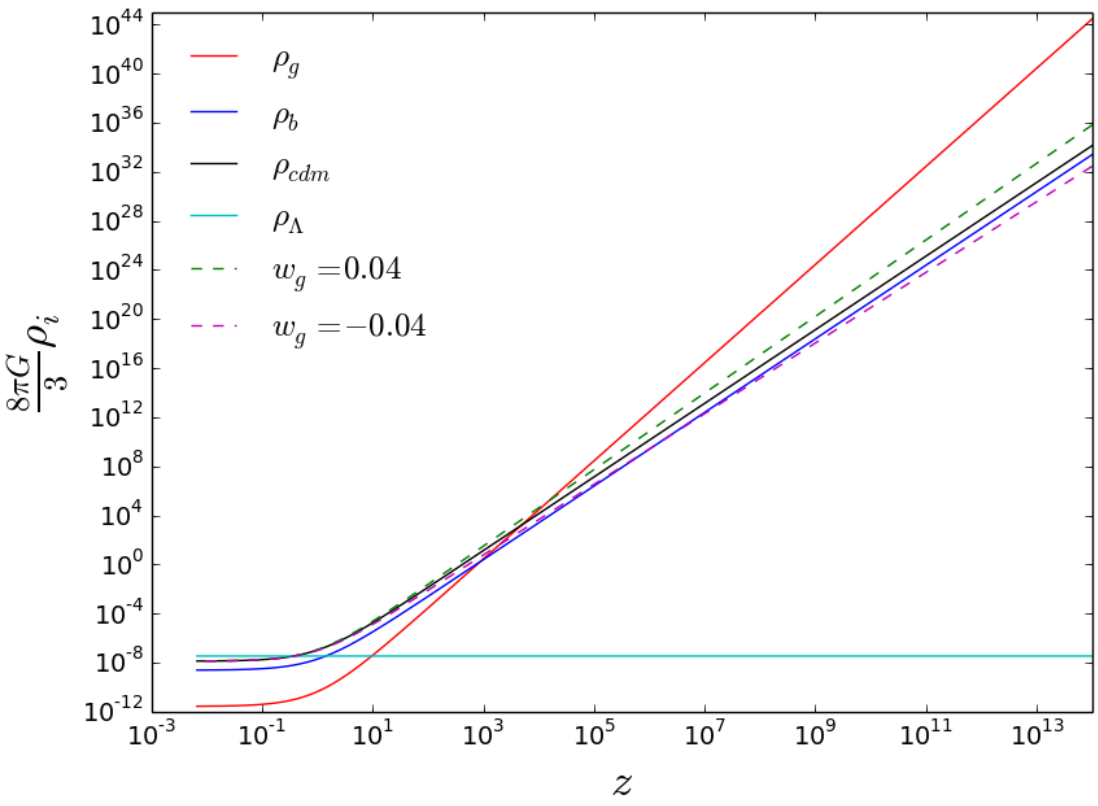

Figure 4.1: The plot shows the evolution of the energy densities of various species. If the fractional energy density in matter today is kept constant, altering $w_{\rm g}$ shifts the time of matter-radiation equality.

w has energy density which decays with respect to redshift z as $(1+z)^{3(1+w)}$. Hence, pressureless matter like CDM has $w_{\rm cdm} = 0$ and its energy density decays as $(1+z)^3$ as seen by the black line in Fig. 4.1. Altering $w_{\rm g}$ changes the relative abundance of radiation in the early universe and hence the time $\tau_{\rm eq}$ of matter radiation equality.

If $\tau_{\rm eq}$ is shifted to earlier (later), power in the higher CMB multipoles is suppressed (enhanced) through an effect know as acoustic driving, which only occurs in the radiation-dominated universe [180, 191]. Power in the first CMB peak can be suppressed (enhanced)

if the fractional energy density in radiation around the time of recombination is decreased (increased). This occurs through the early integrated Sachs-Wolfe (ISW) effect [180]. The ISW effect arises due to evolving gravitational potentials. Around the time of recombination, gravitational potentials evolve and decay due to radiation leaking from these wells. Photons travelling through these wells as recombination occurs, fall in to deeper wells than they climb out of, gaining energy. Similarly, photons travelling through voids lose some energy. If the relative energy density in radiation decreases (increases), the early ISW effect gives less (more) of a boost to the first CMB peak.

Sub-dominant effects of changing w_g include shifting the angular scales or multipoles of CMB peaks because the time of recombination is altered by approximately as much as $\tau_{\rm eq}$, and altering relative peak heights, which are sensitive to the baryon-dark matter ratio [180]. All of these effects can be seen in Fig. 4.2.

The above is for a constant w_g with a value close to zero [189]. If w_g is very different from zero, GDM pressure is appreciable and causes the decay of gravitational potentials and hence an ISW effect throughout matter domination, boosting the CMB peaks to values inconsistent with data. If w_g is time-dependent, the above effects will take place depending on the value of w_g and the era in cosmic history.

The effect of c^2_{eff} and c^2_{vis} on the CMB is degenerate, but can be distinguished with the matter power spectrum. For the CMB, as GDM is the dominant species during matter domination, its ability to have pressure waves and viscosity makes gravitational potentials decay, giving rise to a late-time ISW effect. This ISW effect adds power at the scales in

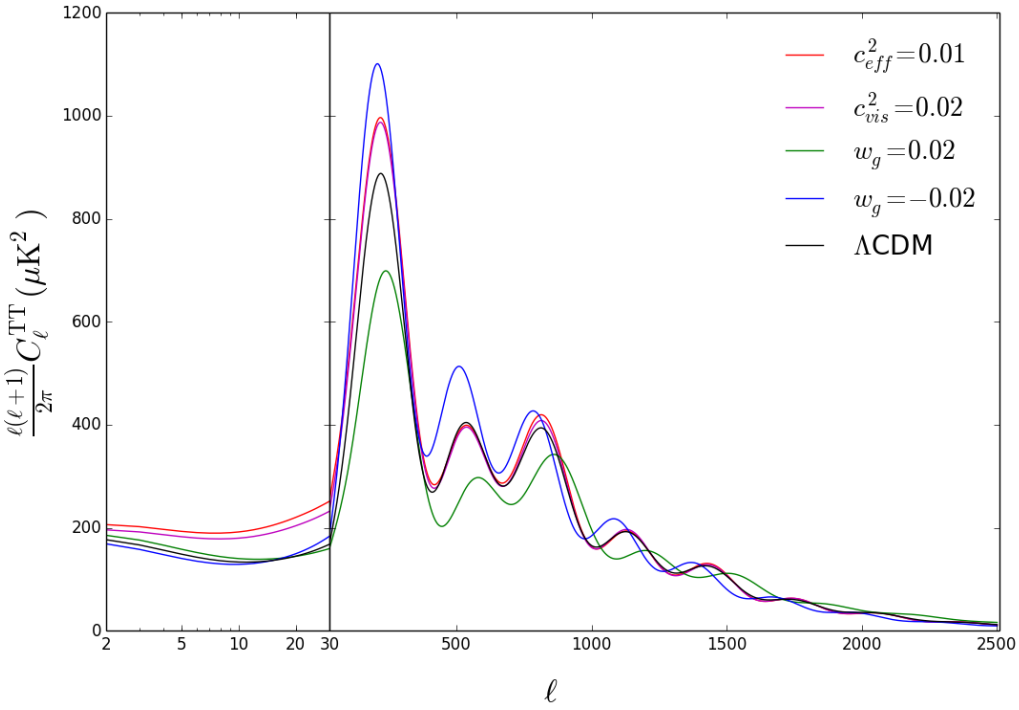

Figure 4.2: The CMB TT power spectrum is shown for various GDM scenarios alongside ΛCDM.

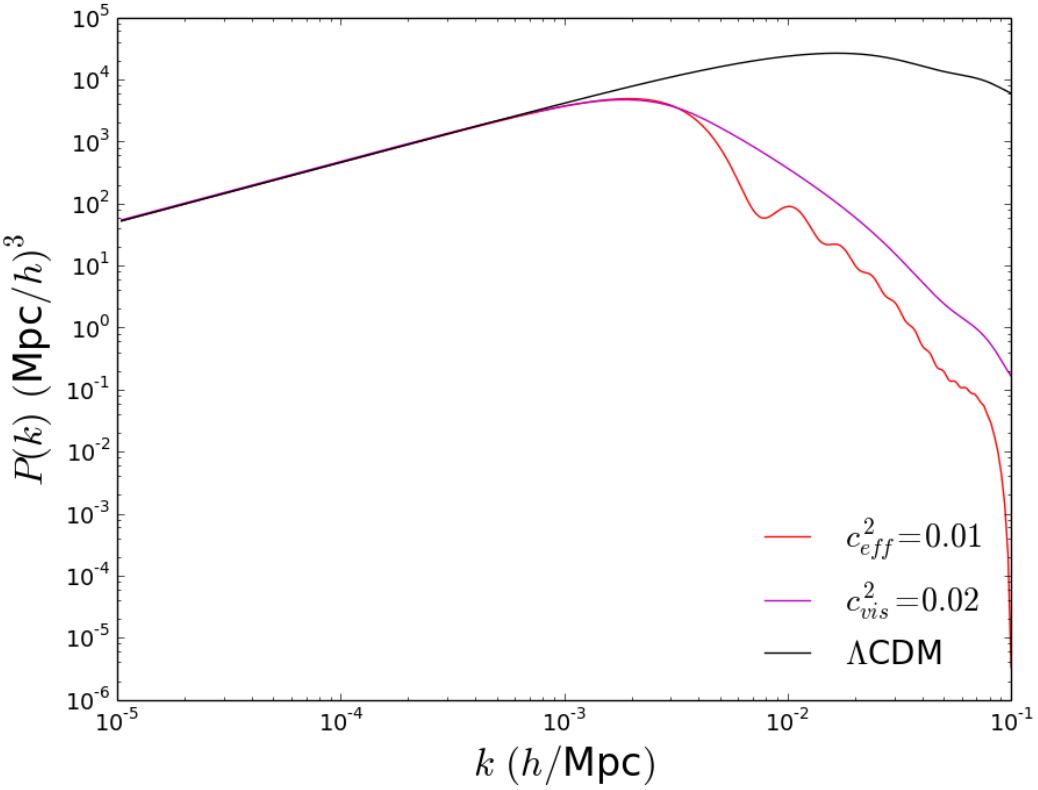

Figure 4.3: The matter power spectrum is shown here for various cosmologies including ΛCDM and two GDM scenarios.

the CMB that entered the horizon during matter domination $\ell \lesssim 500$. Their effect on the CMB can be seen in Fig. 4.2.

The matter power spectrum breaks this degeneracy as shown in Fig. 4.3. With non-zero c^2_{eff} or c^2_{vis}, gravitational potentials decay, reducing clustering on smaller scales and suppressing power in the matter power spectrum at small scales. Furthermore, if GDM has non-zero effective sound speed and small or no viscosity, there are oscillations in the matter power spectrum. For $c^2_{vis} \gtrsim c^2_{eff}$, these oscillations will be damped out.

4.2 Applications of the GDM formalism

4.2.1 Principal component analysis with GDM

To investigate the behaviour of dark matter and dark energy over time in a model-independent manner, I propose to use GDM to model the full dark sector and do a principal component analysis (PCA) [192–197] on the GDM parameters.

PCA is a sophisticated method capable of placing constraints on the time-dependence of GDM parameters in a model-independent way. The parameters can be described as linear combinations of N basis functions, for example,

$$w_g(z) = \sum_{i=1}^{N} A_i f_i(z) \tag{4.5}$$

where the functions $f_i(z)$ are a complete orthogonal set of functions of redshift. These can be anything from Fourier modes to simple redshift bins. The constants A_i are amplitudes of these basis functions. PCA then picks out the linear combinations of basis functions $f_i(z)$ that the data are most sensitive to, in this case, the CMB. In this example, the first principal component $\tilde{w}_g^1$ is the linear combination of basis functions that the data constrain most strongly. The second principal component $\tilde{w}_g^2$ is the linear combination of basis functions that the data are second most sensitive to and so on. As the basis functions can be anything, $w_g(z)$ becomes model-independent and data-driven. As the data are decreasingly sensitive to incrementing principal components, only the first few ($\sim k$) components need to be considered in subsequent analysis.

Once principal components $\tilde{w}_g(z)$ have been acquired, a Markov chain Monte Carlo analysis can constrain the amplitude $\tilde{A}^j$ of each principal component, mapping the time dependence of GDM parameters with a fully model-independent approach:

$$w_g(z) = \sum_{j=1}^{k} \tilde{A}^j \tilde{w}_g^j(z). \tag{4.6}$$

One way to extend my previous work with GDM and PCA would be to choose the basis functions $f_i(z)$ such that they imitate the early dark energy proposed therein. This would constrain the ensemble of early dark energies proposed (see §2.2). This analysis has far more potential, though. We can easily examine whether any kind of dark energy or dark matter can resolve the Hubble tension, not just the form studied in my previous work.

The powerful GDM formalism coupled with the sophisticated PCA can answer the key cosmological questions – what are dark energy and dark matter and how has the Universe has evolved? Even if the results simply confirm the ΛCDM descriptions of dark energy and dark matter, they will be groundbreaking as they would have been obtained using a completely model-independent approach.

4.2.2 The CMB low multipole tension

The CMB spectrum is well measured down to small scales, corresponding to multipoles of $\ell \simeq 2500$ [9, 22] and the ΛCDM model predicts the observed CMB to great accuracy [9,15,16,22]. At low multipoles of $\ell \lesssim 30$, however, there remains a discrepancy between the power expected in the CMB TT spectrum and the smaller power observed. This discrepancy

could arise due to cosmic variance, or, as speculated by [198,199], could be further indication for physics beyond the standard ΛCDM model.

In [199], it was demonstrated that if the expansion history of the Universe is altered, the late ISW effect could lead to suppression of low CMB multipoles. Changing the expansion history of the Universe in a manner that causes the decay of gravitational potentials induces an ISW effect. If this decay occurs at late times, it alters the larger scales, or low multipoles in the CMB. Ref. [199] demonstrated that this late ISW term could remove power from the low CMB multipoles and hence suppress them. The authors simply aimed to illuminate how the ISW effect could lead to suppression, and not just enhancement of power in CMB multipoles, as most cosmologists previously believed. Details of what physically causes the expansion history to change were not addressed.

In order to motivate the required change in the expansion history of the Universe and perhaps gain some physics insight from it into the nature of dark energy and dark matter, I will approach the low-ℓ tension using GDM. GDM can suppress low-ℓ power as it alters the expansion history of the Universe and can cause gravitational potentials to decay, both through non-zero w_g. Through this exercise, we may find that data does not disfavour dark matter behaving unlike its cold counterpart at intermediate redshifts. It will also expose the sensitivity of the CMB to cosmic history at $z \lesssim 50$ and the sensitivity of data to the Universe behaving very differently from a ΛCDM universe at intermediate redshifts.

Chapter 5

The Cosmic-Ray Positron Excess

In addition to the cosmic microwave background, cosmic rays provide another dark matter probe. Recently, satellite experiments detected more flux at high energies of cosmic-ray positrons than expected by conventional astrophysical models, indicating new local sources [55, 56, 200]. This was exciting as it could be a dark matter signal produced by dark matter particles annihilating into Standard Model particles. However, while there is no evidence that dark matter interacts with the Standard Model in this way, there is clear evidence that galactic pulsars can trap and accelerate positron at the observed energy levels [63–66]. My work explores how pulsars may explain this CR e^+ excess [61, 62]

By simulating unobserved pulsars in the galaxy and accounting for uncertainty in the astrophysical parameters relating to the production and propagation of these cosmic rays, we determined the positron flux expected from Milky Way pulsars. At high energies, the number of pulsars that can contribute cosmic-ray positrons drops to a few. This results

in spectral features in the positron fraction related to the individual contributing pulsars. Such spectral features would be absent if interacting dark matter sourced these positrons. My research developed a new technique for analyzing cosmic-ray data, which quantifies such fluctuations in cosmic-ray energy spectra. This chapter presents this research and is heavily based on Ref. [61] [1], work done in collaboration with Ilias Cholis and Marc Kamionkowski. It also contains excerpts from Ref. [62] [2].

At the current level of precision of the experiments and uncertainty in astrophysical parameters, dark matter cannot be ruled out as a potential source. However, with this technique, we may distinguish between the dark matter and pulsar scenarios for the production of cosmic-ray positrons in the future as cosmic-ray data improve. This is a novel approach to evaluate astrophysical and dark matter models based on cosmic rays and provides a deeper understanding of the data.

5.1 The CR positron excess and possible explanations

Cosmic-ray (CR) antimatter provides a probe of new phenomena at high energies. Most antimatter CRs are produced via inelastic collisions of regular high energy CR nuclei with the interstellar medium(ISM) gas. The resulting stable particles from these interactions are referred to as CR secondaries, and the observed fluxes are well described by astrophysical models [201–206]. However, the CR positron flux, and energy spectrum of the positron fraction $e^+/(e^+ + e^-)$, is under-predicted above $\sim$10GeV by these models. Since energy

[1] Ref. [61] was published in Physical Review D © 2018 American Physical Society.
[2] Ref. [62] was published in Physical Review D © 2018 American Physical Society.

losses from synchrotron emission and inverse Compton scattering are much more important for $e^{\pm}$ than nuclei, this discrepancy in the high-energy positron flux is expected to be local; associated with the propagation of CRs in the local $\sim$kpc^3 volume [207] or with characteristics of CR $e^{\pm}$ sources in the same volume. These sources could be local supernova remnants (SNRs) [208–217], local pulsars [218–228] or particle dark matter (DM) [57–60, 226, 229–242].

A number of observations suggest that SNRs are the primary source of Galactic CR nuclei with energies up to $O(100)$TeV. Yet, SNRs can explain the positron fraction only if the metallicities of environments of recent SNRs within $\simeq$kpc are different from those averaged within 10kpc [214, 215, 243, 244]. DM explanations for the CR positron excess are constrained by cosmic-microwave-background data [22, 173, 245–248] and γ-rays [249–251], but parts of the parameter space are still available. Pulsars are a natural source of hard CR $e^{\pm}$ injection into the ISM. However, at the highest observed energies, $\gtrsim$ 500GeV, only a few very local sources, including Geminga, Monogem, and Vela, would dominate the CR flux. With recent observations from HAWC [63, 252] and Milagro [253] of $\gtrsim$ 10TeV γ-ray halos at $O(10)$pc around Geminga and Monogem, we now have strong indications that CR $e^{\pm}$ exit the surrounding pulsar wind nebulae (PWNe) [64], with additional implications for both pulsar searches [65] and the TeV emission observed by HESS [254] towards the Galactic centre [66].

5.2 The pulsar explanation of the CR positron excess

Pulsars are born in the Milky Way at a rate of $\simeq$1 per century [255–258]. Thus only one new pulsar every 10^3 years is born within 4-kpc distance that $\gtrsim$ 10GeV positrons can travel. Moreover, since the energy-loss timescale is $\sim$ 10Myr for $E \gtrsim$GeV positrons, no more than $\sim 10^4$ pulsars can contribute positrons with energies above a few GeV. Above 100GeV the equivalent distance drops to 2 kpc and the maximum age to 2Myr, and above 500GeV to 1kpc and 400kyr. Thus, as we go to higher energies, the number of candidate pulsar sources decreases. Given the rough maximum $e^{\pm}$ energy $E_{\rm max} \sim 100\,{\rm GeV}(R/2\,{\rm kpc})^{-2}$ from a pulsar at a distance R, the discreteness of the source population shows up as spectral features in the CR spectra [222, 224]. This is illustrated schematically in Fig. 5.1. These, moreover, cannot be mimicked by DM (even if there are multiple DM particles) [238, 259].

The red-curve in Fig. 5.1 illustriates the type of spectral features induced by discreteness of the source population. Shown is the positron-fraction for a simulation of pulsars born within 4kpc from the Sun at a rate of 1kyr^{-1}. The amplitude of the wiggles increases as the number of contributing sources decreases. We show for comparison the prediction from an example DM model (green-line) from [226] typical of [59, 60, 239, 260]. Both the DM and pulsar models give good fits to the *AMS-02* measurement. Even with 20 years of data, given the combined statistical and systematic errors [55], *AMS-02* will not distinguish the DM model from the smoothed version of the red curve. The red curve may, however, be distinguished through the presence of the wiggles.

In this work, we suggest a power-spectrum technique to search for wiggles in the positron

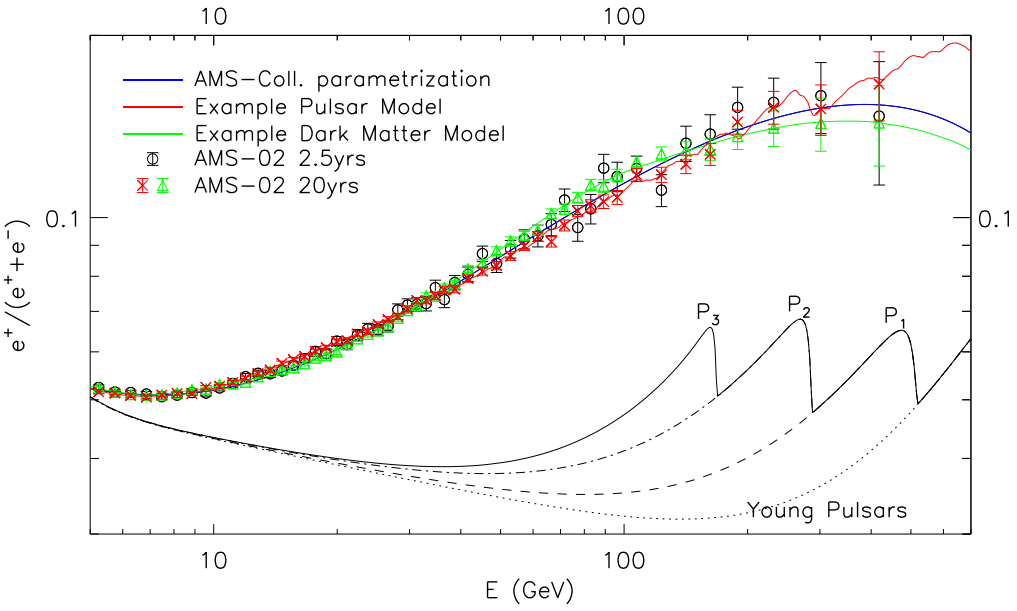

Figure 5.1: The *AMS-02* positron fraction measurement [55] and two examples of models that fit it well. The red line is from the contribution of many Milky Way pulsars, while the green line is from a sample DM model. The DM spectrum is smooth, while the pulsar spectrum shows evidence of contributions from individual sources at high energies. The curves labelled P_1, P_2 and P_3, illustrate schematically the contribution from individual pulsars, at distances of 0.66, 0.97 and 1.7 kpc and ages of 240, 430 and 740 kyrs, respectively. The dotted line shows the contribution from pulsars with ages $\leq$150kyrs. We include a measurement of each model after 20yr with *AMS-02*. We would not be able to separate them through a fit to the spectrum. We include the AMS-Collaboration parametrization [55].

energy spectrum induced by discreteness of the source population. We perform 900 simulations of the Milky Way pulsar population accounting for the astrophysical uncertainties in this population. We then evaluate the prospects to detect, with this power-spectrum analysis, pulsar-induced wiggles. While current data are unlikely to have sufficient sensitivity, we find that the prospects to detect wiggles with forthcoming data are good enough to warrant a careful analysis.

5.2.1 Data

We use published *AMS-02* data [55] that stem from 2.5 years of measurements from 5 GeV and up to 500 GeV. We also simulate for 20 yr assuming the same energy bins and percentage systematic errors. We also project three years of spectral measurements of the combined $e^{\pm}$ flux, up to 1 TeV, by *DAMPE*. Here, we work with binned data, but note that there may be benefits, in a realistic analysis, to working with the raw data; especially if the bin widths exceed the instrumental resolution.

5.2.2 Astrophysical uncertainties surrounding the pulsar explanation

The contribution of local pulsars to the measured CR spectra is influenced by uncertainties. These include uncertainties involving the neutron-star distribution in the Milky Way [256, 257, 261], their birth rate [255–258] and luminosities, the fraction of power that goes to CRs, the spectrum of the CRs injected into the ISM, and uncertainties regarding the CR diffusion, energy-losses and the impact of the time-evolving Heliosphere.

We model these uncertainties by producing astrophysical realizations spanning the rel-

evant multi-dimensional parameter space in a discrete manner. We call these *unique* points on this space *pulsar astrophysical realizations* or just *simulations*. An example of four such pulsar astrophysical realizations is shown in Fig. 5.2. The current data show that the positron fraction rises monotonically from 7 GeV to ∼300 GeV. We show several simulations that fit the data over the range that it is measured. These fitted simulations show that the spectrum can either continue to rise to a value $\gtrsim 0.20$ at an energy of a TeV or flatten to a value of $\simeq 0.16$, or even drop to $\simeq 0.1$ at that energy. *AMS-02* will have the sensitivity to eventually observe such values of the positron fraction. Moreover, different astrophysical realizations can predict a pulsar spectrum that is inherently smooth and featureless or one that has detectable features [61].

Neutron star birth distribution

The cosmic-ray $e^{\pm}$ observed are local and come from sources within a radius R from us where that radius is smaller at higher energies. Thus, the observed cosmic-ray $e^{\pm}$ flux is sensitive to the spatial distribution and birth rate of pulsars within this volume. The birth rate and spatial distribution of pulsars within the Milky have been subjects of extensive work [256, 257, 261, 262]. Yet there are great uncertainties in both, given the lack of a complete pulsar survey of the sky at radio wavelengths. Moreover, the pulsars' radio emission is highly anisotropic, beamed with an opening angle spanning about one tenth of the pulsars' 4π steradians. In fact, observations suggest that this ratio (typically referred to as the beaming fraction) is time-dependent, being larger at the earlier stages of the pulsar's evolution (as high as $\simeq 50\%$ during its first 10 kyr) and gradually decreasing. At gamma-ray wavelengths,

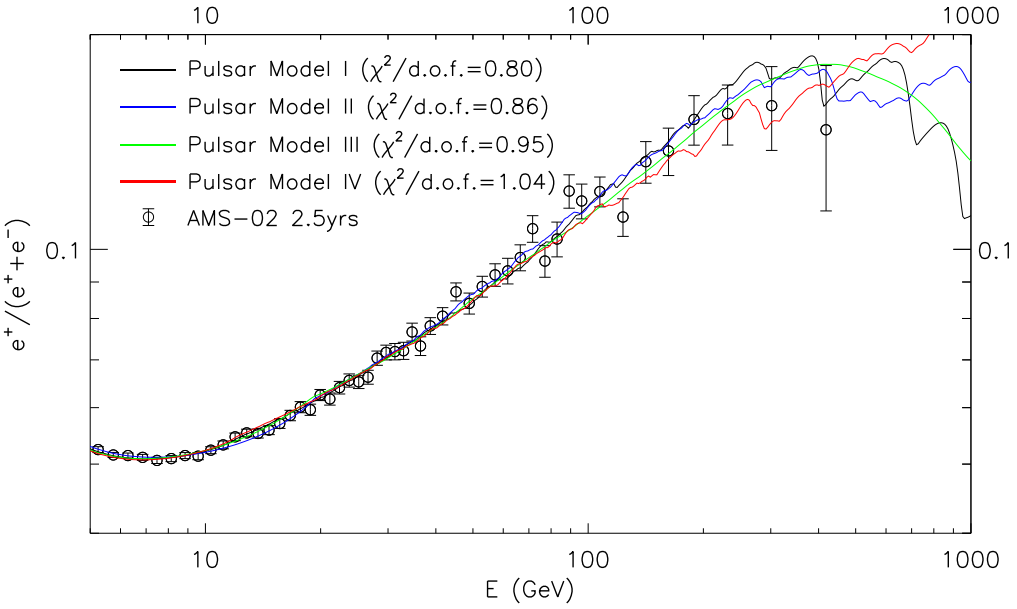

Figure 5.2: Four different pulsar astrophysical realizations. The predicted positron-fraction spectrum, which is observed to increase from 7 to ∼300 GeV, can either drop at higher energies (model I, in black line), flatten out (model II, in blue line), or keep rising up to a TeV (model IV, in red line). Also depending on the exact ISM assumptions, it can be smooth (green line) or have features associated with individual pulsars whose presence can potentially be detected [61].

the surveys do span the entirety of the sky but are sensitive only to the brightest sources, i.e., the most powerful, younger, and nearby members of the pulsar population.

The Milky Way pulsar birth rate has been estimated to be 1.4 ± 0.2 per century in Ref. [257], with alternative estimates that range between one and four per century at one σ [255, 256, 258]. In our analysis, the pulsar birth rate is degenerate with the fraction of spin-down power that goes to high energy $e^{\pm}$ and thus for simplicity we choose it to be one per century.

The spatial distribution of pulsars at birth is expected to follow the stellar distribution in the Milky Way's spiral arms. It has been modelled in Refs. [256, 257, 261] based on the Parkes multi-beam survey at 1.4 GHz [263]. We generate simulations of Milky Way pulsar populations. To generate these simulations, we follow both the parametrization of Ref. [261] and Ref. [257] taking the latter as the canonical distribution. More precisely, for the distribution of pulsars in galactocentric distance r we use the radial density profile,

$$\rho(r; B, C) = A \left(\frac{r}{R_\odot}\right)^B \exp\left(-C\left[\frac{r - R_\odot}{R_\odot}\right]\right), \tag{5.1}$$

where $B = 1.9$, $C = 5.0$, $R_\odot = 8.5$ kpc, and A is normalized to a pulsar birth rate of one per century. Using Eq. (5.1), we are led to the following probability distribution function for the radial distance r of a pulsar from galactic centre,

$$PDF(r, B, C) = \frac{C^{B+2}}{A e^C R_\odot^2} \frac{\rho(r) r}{\Gamma(B+2)}, \tag{5.2}$$

where $\Gamma(x)$ is a Gamma function. Our spatial simulations so produced are consistent with Ref. [261] as shown in Fig. 5.3.

Furthermore, in our generated simulations, pulsars have a distance z away from the disk that follows a Laplace distribution with a scale height of 50 pc and mean of 0 pc, in accordance with Ref. [256]. Finally, we do not try to simulate the spiral arms of the Galaxy, but simply assume a uniform distribution in Galactocentric angle.

Neutron star spin-down distribution properties

Neutron stars (NSs) are born from the core collapse of massive stars in the range of 8–25 $M_\odot$. Given their violent birth combined with supernova explosions not being perfectly spherically symmetric, neutron stars have large three-dimensional kick velocities (e.g. Ref. [264] find kick velocity to be 400 ± 40km/s) and also large ($\sim 10^{49}$ erg) initial rotational energies. They also have strong magnetic fields due to the contraction of the initial core, with large uncertainties in the magnetic-field strengths due to magnetohydrodynamic instabilities formed in the early stages of the NS birth. The strength of the initial magnetic fields at the poles ranges between $\sim 10^{12} - 10^{15}$ G. These rapidly rotating strong magnets will suffer the loss of rotational energy with initial spin-down powers that may also span orders of magnitude given the large uncertainties in the initial magnetic fields and rotational frequencies. This spin-down power evolves with time as,

$$\dot{E}(t) = \dot{E}_0 \left(1 + \frac{t}{\tau_0}\right)^{-\frac{\kappa+1}{\kappa-1}} . \tag{5.3}$$

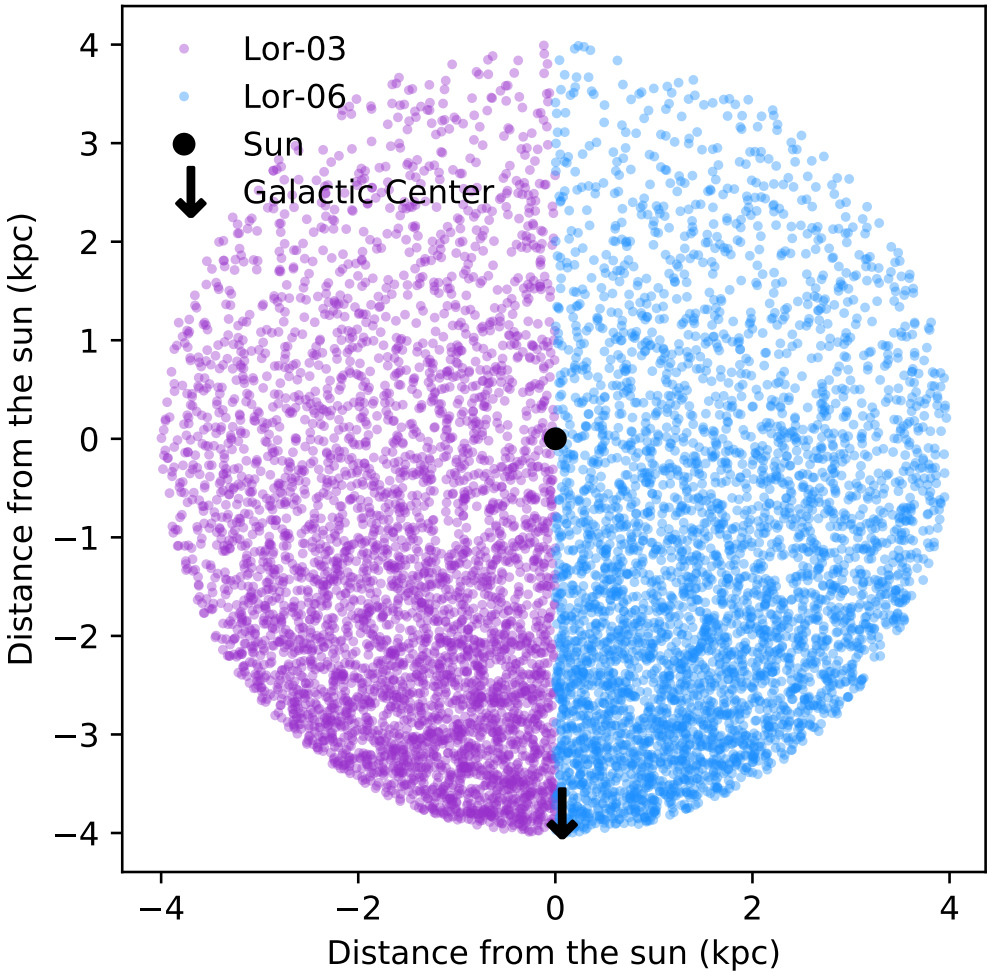

Figure 5.3: The pulsars simulated within 4 kpc of the Sun, projected onto the Galactic disk. The Galactic center is at $(0, -8.5)$ kpc. The Sun is the black dot at $(0, 0)$. The purple dots were simulated using the empirical pulsar radial distribution curve presented in Ref. [261]. The blue dots were simulated using the best-fit pulsar radial distribution curve given in Ref. [257]. Both produce very similar results. The number of pulsars in both simulations were normalized such that one per century is born in the Galaxy, showing pulsars up to 10 Myr in age.

Here, E_0 is the initial rotational energy (i.e. $E_0 = 1/2\ I_0\Omega_0^2$, with I_0 the neutron-star moment of inertia and Ω_0 its initial angular frequency),

$$\tau_0 = \frac{\dot{\Omega}}{(\kappa-1)\Omega}\left[1-\left(\frac{\Omega}{\Omega_0}\right)^{\kappa-1}\right] \tag{5.4}$$

is the characteristic timescale, or age, of a pulsar, and κ is the braking index describing the time evolution of the neutron stars' angular frequency Ω through $\dot{\Omega} \propto \Omega^{\kappa}$. Setting $\kappa = 3$ describes the spin-down due to magnetic-dipole radiation. Measurement of κ demands knowledge of Ω, $\dot{\Omega}$ and $\ddot{\Omega}$ ($\kappa \equiv \ddot{\Omega}\Omega/\dot{\Omega}^2$). This biases the measurement toward young pulsars where $\ddot{\Omega}$ is not too small to measure, and young pulsars may not be characteristic of the general distribution. Typical observed values give $\kappa \lesssim 3$ [67–69,265,266], but there are also recent measurements of young pulsars with higher braking-index values [267]. Moreover the pulsar braking index may evolve with time depending on the specific properties of the pulsar [268].

Given these uncertainties, our simulations test three different choices, $\kappa = 2.5$, 3.0, and 3.5 for the braking-index. For each choice, we also choose a value for the characteristic spin-down timescale τ_0. Finally, we account for pulsars not having a universal initial spin-down power given the wide ranges of observed magnetic fields for young pulsars ($\sim 10^{12} - 10^{14.5}$ G). We simulate pulsars with an initial spin-down power $\dot{E}_0$ given by

$$\begin{aligned} \dot{E}_0 &= 10^{x}\ \mathrm{erg/s} = 10^{x_{\mathrm{cutoff}}-y}\ \mathrm{erg/s},\ \text{with} \\ f(y) &= \frac{\mathrm{Exp}\left\{-\frac{[-\mu_y+ln(y)]^2}{2\sigma_y^2}\right\}}{\sqrt{2\pi}y\sigma_y}. \end{aligned} \tag{5.5}$$

The values for $x_{\rm cutoff}$ and μ_y are constrained by radio observations of rotation periods and modeled surface magnetic fields of Myr old pulsars [256]. Moreover observation of the Crab pulsar at $\simeq 1$ kyr imposes a hard cut-off on observed spin-down power of pulsars larger than $10^{38.7}$ erg/s [269]. In our simulations we take $\sigma_y = [0.25, 0.36, 0.5, 0.75]$. Those observational constraints result in pulsars with τ_0 values as small as 0.6 kyr for $\kappa = 2.5$ and as large as 30 kyr for $\kappa = 3.5$, with typical values of 6–10 kyr for breaking index of 3.0. In Fig. 5.4, we show normalized histograms of $\dot{E}$ for each value of σ_y for simulations that are allowed by the data. Table 5.1 we give all the spin-down power distribution properties for our pulsar simulations.

We allow for a wide range of assumptions regarding the true underlying current period of pulsars with ages $\leq$ 10 Myr, as well as their surface magnetic fields. Since we rely on observations of pulsars with ages of order 10^5-10^7 years, we probe predominantly that population and not the spin-down conditions in the very early stages. We then use the CR measurements to constrain the birth properties of the pulsar population.

We also note that neutron-star kick velocities of $\sim$ 100 km/s result in a displacement of $\sim$ 100 pc of the NSs from their birth location within 1 Myr, but only a few pc in their first $\sim$10 kyr ($\simeq \tau_0$) that is relevant for our work. We thus take their distribution in space to be their distribution at birth.

Injection properties of CR positrons

Electrons get accelerated inside the magnetosphere, produce ICS γ-rays, which in turn in the presence of strong magnetic fields pair produce $e^{\pm}$. These $e^{\pm}$ get further accelerated

Sim no.	τ_0 (kyr)	κ	$x_{\rm cutoff}$	y_μ	y_σ
30-59	3.3	3	38.8	0.25	0.5
120-149	6	3	38.8	0.25	0.5
150-179	3.3	3	38.8	0.25	0.5
180-209	10	3	38.8	0.25	0.5
210-239	3.3	3	39	0.1	0.5
240-269	1	2.5	38.8	0.25	0.5
270-299	20	3.5	39	0.1	0.5
300-329	0.7	2.5	38.8	0.25	0.5
330-359	20	3.5	39.1	0.0	0.25
360-389	0.6	2.5	39.0	0.1	0.25
390-419	6	3	39.0	0.1	0.25
420-449	6	3	38.7	0.5	0.75
450-479	30	3.5	38.8	0.25	0.5
480-509	0.85	2.5	38.5	0.6	0.75
510-539	18	3.5	39.0	0.0	0.75
540-569	10	3	38.7	0.5	0.75
570-599	4	3	39.0	0.0	0.36
600-629	1	2.5	38.7	0.5	0.75
630-659	9	3	38.2	0.4	0.36
660-689	0.8	2.5	38.2	0.4	0.36
690-719	0.6	2.5	38.2	0.4	0.36
720-749	30	3.5	38.2	0.4	0.36
750-779	7	3	39.0	0.1	0.75
780-809	30	3.5	38.0	0.5	0.36
810-839	30	3.5	38.7	0.5	0.75
840-869	6	3	38.9	0.18	0.36
870-899	4.5	3	39.3	0.0	0.25
900-929	9	3	38.5	0.5	0.25
930-959	27	3.5	38.5	0.3	0.25
960-989	33	3.5	38.0	0.5	0.25
990-1019	0.85	2.5	38.3	0.5	0.25

Table 5.1: The assumed pulsar-simulation spin-down power distributions and time evolution. Simulations $\#30-59$ are produced based on Ref. [261], while all others are on reference assumption of Ref. [257].

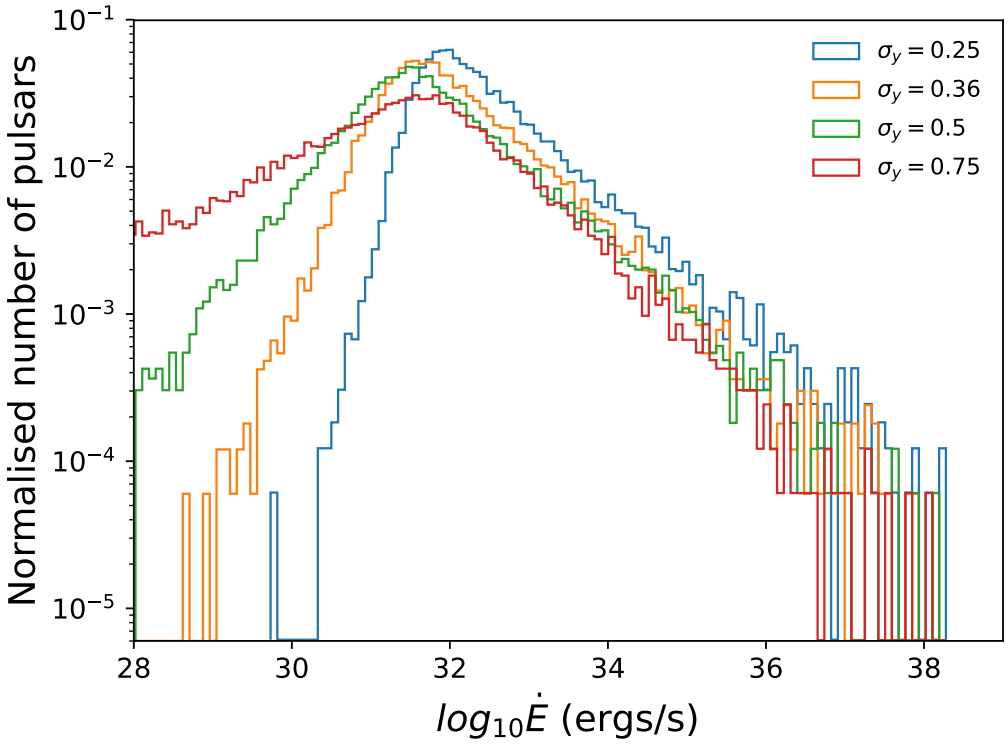

Figure 5.4: Shown here are normalized histograms of pulsar luminosities from various realizations. This is not their birth luminosity, but the luminosity evolved to today using Eq. (5.3). All simulations shown have a braking index of $\kappa = 3.0$. For the blue histogram, the surface magnetic fields of simulated pulsars and for the green, their periods agree well with Ref. [256]. At high luminosities one can notice the Poisson fluctuations that arise in each individual simulation. All distributions shown are associated with models that are allowed by the data.

inside the magnetosphere. In addition, electrons and positrons will then propagate outwards losing energy during adiabatic E-losses, but can also be accelerated in the termination shock of the pulsar(also of the SNR) and the ISM. There is also evidence for γ-rays towards Geminga and Monogem [63, 252, 253], suggesting the presence of CR $e^{\pm}$ at 100 TeV in energy, losing a significant fraction of their energy within $\simeq$ 10pc. Since the spin-down power drops with a time-scale of $\tau_0 \lesssim 10^4$ yrs, about half of the rotational energy will be lost before the SNR shock front stops being an efficient accelerator and well before the PWN stops having an effect on these CRs. Given that the time for CR $e^{\pm}$ to propagate to Earth is an order of magnitude larger than τ_0 we can consider their injection to the ISM instantaneous (see Ref. [222] for further details).

Only a small fraction η, of the spin-down power can go to CR $e^{\pm}$ injected into the ISM.

In this work we are agnostic about the fraction η of the spin-down power that goes into injected $e^{\pm}$. We assume a log-normal distribution for the η parameter,

$$g(\eta) = \frac{Exp\left\{-\frac{[-\mu+ln(-1+\eta)]^2}{2\sigma^2}\right\}}{\sqrt{2\pi}(\eta-1)\sigma}, \tag{5.6}$$

and take three different choices for μ and σ. These lead to three different choices for the combination of mean efficiency η, $\bar{\eta} = 1+\mathrm{Exp}\left\{\mu+\frac{\sigma^2}{2}\right\}$ and logarithmic standard deviation $\zeta = 10^{\sigma}$: $(\bar{\eta}, \zeta) = (4\times10^{-3}, 1.47)$ or $(10^{-3}, 2.85)$ or $(2\times10^{-2}, 1.29)$. In fitting the positron fraction, we allow for each astrophysical pulsar realization an overall normalization change in the pulsar component, that is absorbed into the specific values of $\bar{\eta}$. Our typical $\bar{\eta}$ is a few$\times10^{-2}$ with a range of $2\times10^{-3} - 2\times10^{-1}$.

For the injection CR $e^{\pm}$ spectra we assume,

$$\frac{dN}{dE} \propto E^{-n} Exp\left\{-\frac{E}{E_{\rm cut}}\right\}, \tag{5.7}$$

with n following a flat distribution $g(n)$ either in a narrow range of $n\epsilon\,[1.6, 1.7]$ or in a wider range of $n\epsilon\,[1.4, 1.9]$. The upper cutoff $E_{\rm cut}$ does not affect our fits to the observations, since the highest-energy CR $e^{\pm}$ quickly lose their energy before reaching us; we set it to $E_{\rm cut} = 10$ TeV.

CR propagation through the ISM and heliosphere

Finally as CR $e^{\pm}$ enter the ISM, they must propagate to the Earth where they are observed. From the moment CRs enter into the ISM they diffuse through the Milky Way magnetic field and suffer energy losses due to synchrotron radiation and inverse Compton scattering. There are uncertainties regarding the CR diffusion, energy-losses and the impact of the time-evolving Heliosphere. We have different assumptions to model the propagation through the ISM, using [222, 270]. We use five distinctive models for the ISM that agree with CR data including the B/C ratio, CR protons and He [270]. The characteristics of these five ISM models are given in Table 5.2. We account for the uncertainties of the propagation inside the Heliosphere (i.e. Solar Modulation [271]) by marginalizing over them following [270] and [243]. For the time-evolution of the heliospheric magnetic field we use information from the Ace Science Centre [3] and Wilcox Solar Observatory [4].

[3] http://www.srl.caltech.edu/ACE/ASC/
[4] http://wso.stanford.edu/Tilts.html

Model	b ($\times 10^{-6}$GeV^{-1}kyr^{-1})	D_0 (pc^2/kyr)	δ
A1	5.05	123.4	0.33
C1	5.05	92.1	0.40
C2	8.02	92.1	0.40
C3	2.97	92.1	0.40
E1	5.05	58.9	0.50

Table 5.2: The basic parameters that describe the propagations assumptions of cosmic rays in the Milky Way. Assuming isotropic and homogeneous diffusion, $D(R) = D_0(R/1GV)^{\delta}$. The energy losses due to synchrotron radiation and inverse Compton scattering are described by $dE/dt = -b\,E^2$.

The impact of these uncertainties on the morphology of the CR spectra is shown in Figure 5.5 for the positron fraction (coloured lines). Depending on the assumptions on the energy losses and diffusion time-scales, the spectral features can be more pronounced or suppressed.

Once exiting the ISM and entering the heliosphere, CRs will reach our detectors, after diffusing through the anisotropic magnetic-field structure of the fast evolving heliospheric magnetic field. During their propagation through the heliosphere, CRs also transfer via drift effects that impact how fast they will reach Earth, and the path they are most prone to follow through the Heliosphere. During that time CRs will also go through adiabatic energy losses. We account for these following Ref. [270].

Pulsar simulations

Given a spatial distribution and pulsar birth rate, a distribution $f(\dot{E}_0)$, choices for κ and τ_0, distributions on the fraction of spin-down power that goes into ISM CR $e^{\pm}$ $g(\eta)$, distribution $h(n)$ on the injection index n, and choice of ISM propagation models, we generate a population of Milky Way pulsars that are within 4 kpc. To understand the

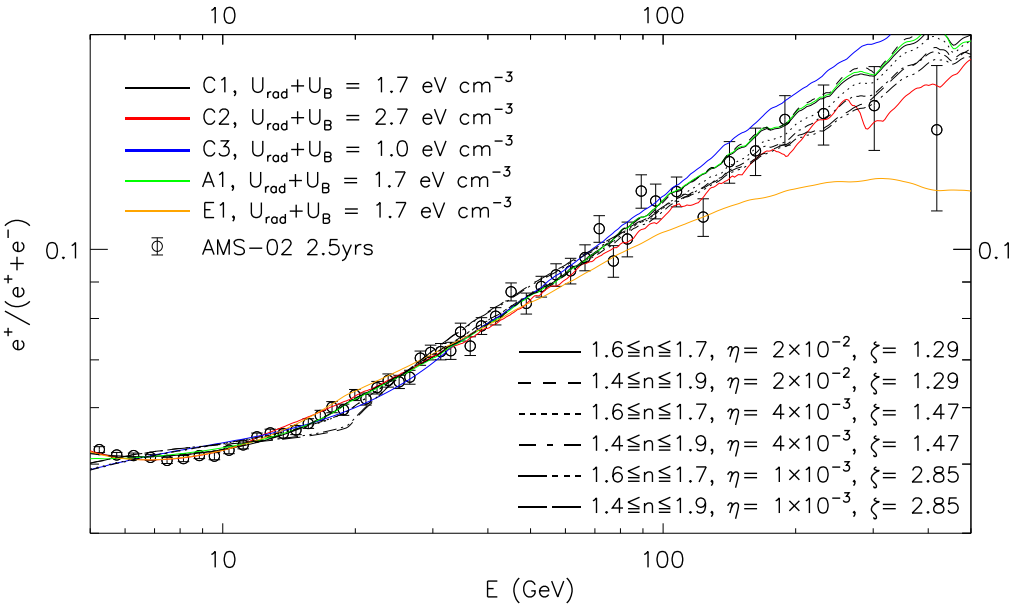

Figure 5.5: The positron fraction, assuming pulsars follow the same distribution in space and in their spin-down power and time evolution. We vary the ISM propagation conditions (different colours) as in Table 5.2, and the CR $e^{\pm}$ spectral properties and fraction of spin-down power into ISM injected $e^{\pm}$. $U_{\rm rad}+U_{\rm B}$ refer to the local energy density in the radiation and magnetic fields. Some of these lines are excluded in the positron fraction spectrum fit and are not used further in the PSD analysis.

impact of these uncertainties on the prospects to detect fluctuations in the positron energy spectrum, we produce 900 astrophysical realizations of expected CR e^+ spectra from pulsars. Each one has a unique combination of the above ingredients while still consistent with pulsar population studies [256] and data on CR propagation in the ISM and the Heliosphere [272].

5.2.3 Differentiating pulsars and dark matter with CRs

Power-spectrum analysis of the CR positron spectrum

We fit the pulsar contribution to the *AMS-02* positron-fraction (containing 51 data points between 5 and 500 GeV) [5] by allowing for an additional normalization on the $e^{\pm}$ pulsar flux and by marginalizing over the uncertainties of primary and secondary CRs and Solar Modulation (leading to five fitting parameters). That alone constrains a significant fraction of the pulsar astrophysical realizations, if they are to explain the positron fraction. This is further explored in subsequent work [62]. Of the 900 pulsar astrophysical realizations, only 172 fit the positron fraction within 3σ from a prediction of 1 per degree of freedom i.e. with a total $\chi^2 \leq 64.2$ for 51-5=46 d.o.f. . For the remainder of this analysis, we use those pulsar astrophysical realizations, one of which is shown in Fig. 5.1. Our results are not sensitive to the exact threshold that we place on the χ^2 of the fit.

For each of the remaining 172 pulsar astrophysical realizations, we generate 10 observational realizations (i.e. add noise following the binning and errors of Ref. [55]); this can

[5] In principle, the analysis may be done with the positron flux instead, since in the positron fraction, the fluctuation amplitude is suppressed given the fluctuations in the electron spectrum. Still, (a) most electrons in the relevant energy range are not from pulsars, so the suppression is small; (b) most publicly available current results are provided in terms of the positron fraction; and (c) some systematic effects that might introduce artificial fluctuations may be cancelled out by working with the positron fraction.

generate artificial fluctuations that mask the wiggles we seek. We then subtract from each observational realization the smoothed spectrum and evaluate the power-spectral density (PSD) of the residual spectrum. Since we do not know the true underlying astrophysical spectrum, we calculate for each realization the smoothed spectrum by convolving with a gaussian whose width increases with energy. This removes power in large scales in energy (low modes in the power spectrum) including contributions from instrument systematics as misestimates of the instrument efficiency or CR contamination. Yet, systematic artifacts in a small number of energy bins could still induce smaller-scale fluctuations that we seek.

To evaluate the PSD on the residual positron spectrum, we take the "time" parameter to be $ln(E/\mathrm{GeV})$ which we assume to be measured in equal intervals. This is to a very good approximation true in the energy range 5–150 GeV, with higher energies having energy bins at larger separations. In our calculations, we assume a logarithmic energy binning of $ln(E_i/\mathrm{GeV}) \equiv x_i = x_0 + a \cdot i$, with $x_0 = 1.6571$ (5.24 GeV) and $a = 0.063$. When comparing to current data, we go up to $i = 59$ (215 GeV) while in our 20-year forecast we go up to $i = 65$ (315 GeV). We calculate the PSDs for each of the 172×10 observational realizations. Given the noise, there is scatter on the PSDs of the 10 observational realizations coming from the same underlying astrophysical realization.

To model the effect of observational scatter on the PSD, we use the *AMS-02* smooth parametrization that fits the data well after 2.5 years and then produce 200 observational realizations of it. We then calculate the 200 PSDs on the residual. Those 200 observational realizations of the *AMS-02* smooth parametrization provide the scatter on the PSD due to noise. For every one of the 60 (66) modes for the current (20 yr) data, we rank the 200

coefficients. We do not expect any correlations between modes. We use the 68% ranges to derive the 1σ error-bars per mode. We then determine a χ^2 fit on each of the PSDs. Among the 200 observational realizations of the *AMS-02* smooth parametrization there is a median in terms of its χ^2 and 68%, 95% and 99% ranges. We use these ranges to *compare* the PSDs from physical models (pulsars or DM) and the PSD from noise. These ranges provide a measure of the scatter due to noise and whether pulsars can give a PSD signal above the noise.

Results

In the top panel of Fig. 5.6 we show the PSD of the measured *AMS-02* positron fraction from the *AMS-02* smooth parametrization (black line). The PSD of the noise realization with the median fit is given by the blue line. We also show the PSDs for the pulsar astrophysical realization and the DM model of Fig. 5.1 adding noise (red and green lines, respectively). As seen there, pulsars produce small-scale (small in $ln(E/\mathrm{GeV})$) variations that lead to extra power in the PSD at high modes (large $f = 1/ln(E/\mathrm{GeV})$). The exact DM phenomenology (i.e mass annihilation/decay channel) can only affect the lower modes. DM models with one very evident and sharp spectral feature that could add some power are already excluded in Ref. [273, 274]. The difference between the red and the green PSDs on the residual positron fraction is what we are interested in. With 20 years of data the situation improves, as shown in the bottom panel of Fig. 5.6, for a 10% chance to see these fluctuations if pulsars are responsible for high-energy CR positrons.

In Fig. 5.7 we show for all 172 pulsar astrophysical realizations and for each of the 10

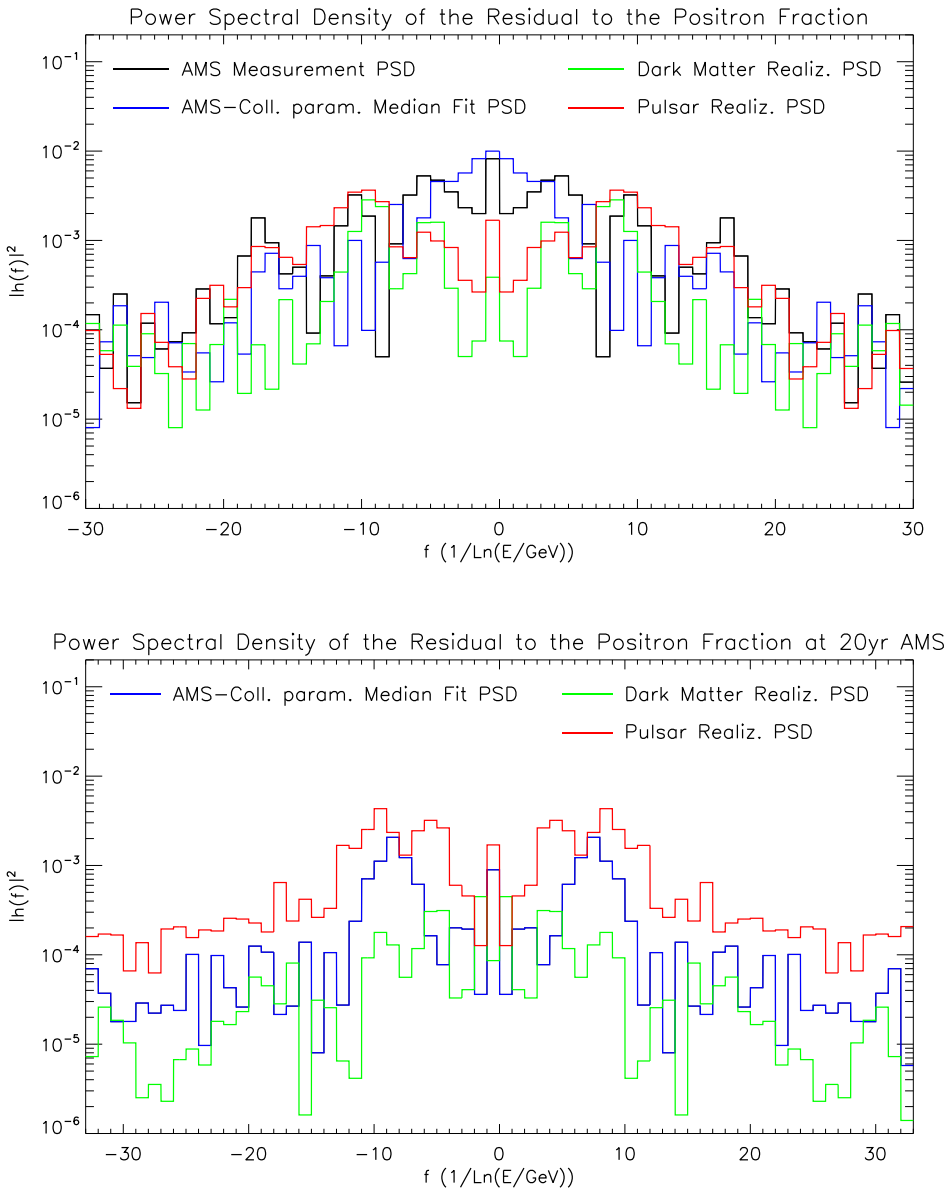

Figure 5.6: The PSD of the residual to the positron fraction from *AMS-02*. *Top*: current state with the black line giving the measurement, the blue line the noise realization with median fit and the red and green lines a pulsars and a DM realization. Since pulsars have spectral features (shown in Fig. 5.1), there is more power at the high modes of the PSD compared to the smooth DM realization. *Bottom*: Same after 20 yr of *AMS-02* observations. The red line is calculated from one pulsar realization that is among the ∼10% of all our observation realizations, which give a signal in the PSD detectable at $\geq 2\sigma$.

observational realizations the PSD χ^2-distribution (red diamonds along y-axis). Each pulsar astrophysical realization is in a different position on the x-axis; ranked starting with the model that fits best the positron fraction spectrum. Our calculation of the fit of the observed *AMS-02* PSD on the residual positron fraction is given by the black line. All diamonds, and the black line are to be compared to the three blue bands that represent the 68%, 95% and 99.7% ranges of the noise. We find that with current data 1.5% (12.5%) of the 172×10 observation realizations lie outside the 99.7% (95%) band (left panel of Figure 5.7). This information is also given in Table 5.3. Since we have ranked our astrophysical realization models on the x-axis by their fit to the positron fraction, Fig. 5.7 also shows that there is no clear correlation between models that provide a poor fit to the smoothed energy spectrum and models that provide a poor fit to the power-spectrum. Also since the data PSD sits well within the 68% band of the noise, there is no indication yet that there is a deviation from a smooth spectrum; however, this null result cannot yet distinguish between different scenarios.

Projections for future data

After 20 years of observations, and using information on the positron spectrum up to 315 GeV, the situation becomes more promising. Then, about 2.5% (10%) of the observational realizations sit within the 99.7% (95%) noise bands, as shown in the bottom panel of Fig. 5.7 and in Table 5.3.

DAMPE [275, 276] and *CALET* [277] are now measuring the total CR $e^+ + e^-$ flux up to several TeV. We forecast the prospects to probe a PSD signal from pulsars to higher

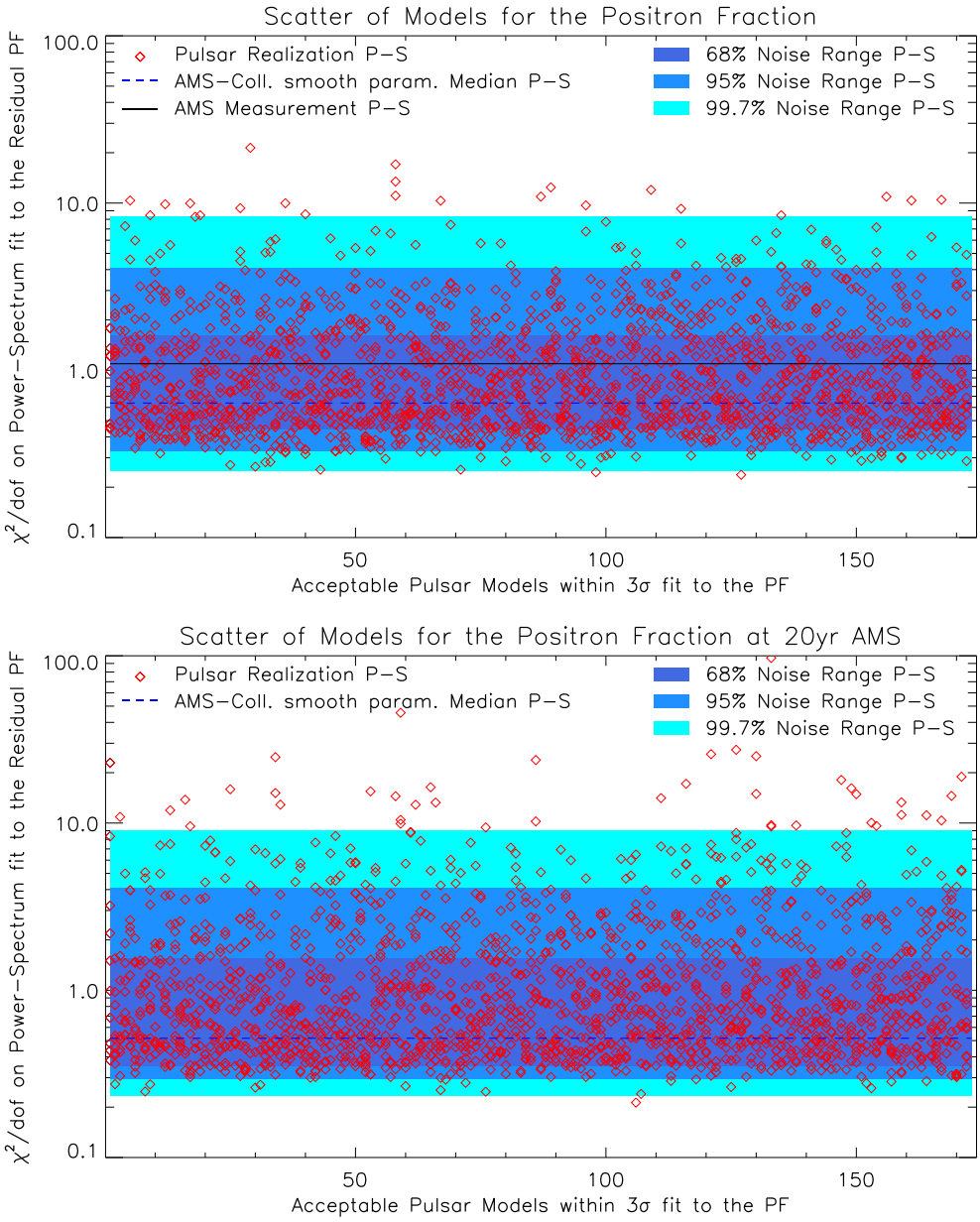

Figure 5.7: The scatter of 10 observational realizations in the PSD χ^2/dof for each of the 172 pulsar astrophysical realizations (red diamonds). The blue bands include the noise ranges for the PSD χ^2. *Top*: Current, with the black line giving the PSD of the measurement, showing no evidence for features. *Bottom*: After 20 years of data, $\sim 10\%$ of the pulsar realizations will provide (at 2σ) detectable fluctuations.

Experiment	E-range (GeV)	#frq. modes	%exc. f. (95%)	%exc. f. (99%)	%exc. f. (99.7%)
AMS-02 (2.5 yr)	5.2-215	±30	12.5	3.5	1.5
AMS-02 (20 yr)	5.2-315	±33	10	6	2.5
DAMPE (3 yr)	25-640	±19	12	7	4

Table 5.3: The potential to observe power from small-scale features to the residual positron fraction (for *AMS-02*) or $e^+ + e^-$ flux (for *DAMPE*). We give the relevant energy range to be used, the # of modes (± 1/2 the number of logarithmically spaced E-bins). " %exc. f." gives the % of realizations that fall outside the 95%, 99% and 99.7% noise ranges.

energies where fewer pulsars contribute to the signal. Using the expected flux measurement between 25 and 640 GeV we find that 38 logarithmically equally spaced energy bins provides us with a good sensitivity to the presence of features. [6] Of the 172 pulsars realizations, 53 include at least one pulsar that has similar power, age and distance as Geminga (PSR B0633+17) and one with similar properties for Monogem (PSR B0656+14). We use that subset, since these pulsars are relevant for that range of energies but not for the energy ranges used for the *AMS-02* data. Our findings are given in Table 5.3 suggesting that indeed going to higher energies is necessary.

5.3 Conclusions

In this work, we have proposed a power-spectrum analysis to identify wiggles in the positron energy spectrum that may arise from discreteness in the pulsar source population, in the event that pulsars are responsible for high-energy CR positrons. Our basic conclusions are that although such wiggles are likely too small to be detectable with current data, the prospects to see such wiggles with forthcoming data warrant the effort such an analysis

[6] Any further optimizations should be left to the collaborations.

would entail.

Our estimates of the detectability of the signal rely on a variety of uncertain ingredients in the modeling of the pulsar-population. To obtain some indication of these uncertainties, we constructed 900 simulated pulsar-population realizations each obtained with different assumptions about the neutron-star distribution, spin-down power characteristics and time-evolution, the injected CR $e^{\pm}$ spectra, and propagation through the ISM and the heliosphere, but requiring consistency with all observational constraints in each simulation used in the analysis. Thus, while our forecast of a $\sim$10% chance to detect these wiggles is uncertain, it is, we believe, based on realistic models. The takeaway message is therefore that the possibility to see something in a PSD analysis is significant enough to warrant a search. It is not, however, certain enough to ascribe any strong conclusions to a null result. With better understanding of the astrophysics in the next decade, the forecast may become more, or less optimistic, but almost certainly more robust. This analysis can be repeated for SNR sources.

The predictions of wiggles are statistical only. We ascribe significance to the presence of wiggles, but we do not make predictions about specific features at specific energies [7]. We also do not ascribe the signal to any specific pulsar (e.g., Geminga or Monogem), although our models are required to have pulsar-populations consistent with the existence of these pulsars. Also, we emphasize that we simply estimate the sensitivity of current measurements to a power-spectrum-based wiggle search. We do hope, however, that this work motivates collaborations like *AMS-02* and at higher energies *DAMPE* and *CALET* to perform their

[7] With a better understanding of the local ISM propagation conditions, by detecting a power-spectrum signal, we will be able to also constrain the number of sources within local distances.

own PSD analysis with their data.

Bibliography

[1] P. Breysse, personal communication.

[2] V. C. Rubin and W. K. Ford, Jr., "Rotation of the Andromeda Nebula from a Spectroscopic Survey of Emission Regions," *Astrophys. J.*, vol. 159, pp. 379–403, 1970.

[3] V. C. Rubin, N. Thonnard, and W. K. Ford, Jr., "Rotational properties of 21 SC galaxies with a large range of luminosities and radii, from NGC 4605 /R = 4kpc/ to UGC 2885 /R = 122 kpc/," *Astrophys. J.*, vol. 238, p. 471, 1980.

[4] M. Persic, P. Salucci, and F. Stel, "The Universal rotation curve of spiral galaxies: 1. The Dark matter connection," *Mon. Not. Roy. Astron. Soc.*, vol. 281, p. 27, 1996.

[5] F. Zwicky, "On the Masses of Nebulae and of Clusters of Nebulae," *Astrophys. J.*, vol. 86, pp. 217–246, 1937.

[6] J. C. Kapteyn, "First Attempt at a Theory of the Arrangement and Motion of the Sidereal System," *Astrophys. J.*, vol. 55, pp. 302–328, 1922.

[7] D. Lynden-Bell, "Statistical mechanics of violent relaxation in stellar systems," *Mon.*

Not. Roy. Astron. Soc., vol. 136, pp. 101–121, 1967.

[8] J. R. Primack, "Dark Matter and Galaxy Formation," *AIP Conf. Proc.*, vol. 1192, no. 1, pp. 101–137, 2009.

[9] P. A. R. Ade *et al.*, "Planck 2013 results. XVI. Cosmological parameters," *Astron. Astrophys.*, vol. 571, p. A16, 2014.

[10] S. Perlmutter *et al.*, "Measurements of Omega and Lambda from 42 high redshift supernovae," *Astrophys. J.*, vol. 517, pp. 565–586, 1999.

[11] A. G. Riess *et al.*, "Observational evidence from supernovae for an accelerating universe and a cosmological constant," *Astron. J.*, vol. 116, pp. 1009–1038, 1998.

[12] R. R. Caldwell and M. Kamionkowski, "The Physics of Cosmic Acceleration," *Ann. Rev. Nucl. Part. Sci.*, vol. 59, pp. 397–429, 2009.

[13] J. Martin, "Everything You Always Wanted To Know About The Cosmological Constant Problem (But Were Afraid To Ask)," *Comptes Rendus Physique*, vol. 13, pp. 566–665, 2012.

[14] D. J. Eisenstein *et al.*, "Detection of the Baryon Acoustic Peak in the Large-Scale Correlation Function of SDSS Luminous Red Galaxies," *Astrophys. J.*, vol. 633, pp. 560–574, 2005.

[15] G. Hinshaw *et al.*, "Five-Year Wilkinson Microwave Anisotropy Probe (WMAP) Observations: Data Processing, Sky Maps, and Basic Results," *Astrophys. J. Suppl.*, vol. 180, pp. 225–245, 2009.

[16] C. L. Bennett *et al.*, "Nine-Year Wilkinson Microwave Anisotropy Probe (WMAP) Observations: Final Maps and Results," *Astrophys. J. Suppl.*, vol. 208, p. 20, 2013.

[17] F. Beutler, C. Blake, M. Colless, D. H. Jones, L. Staveley-Smith, L. Campbell, Q. Parker, W. Saunders, and F. Watson, "The 6dF Galaxy Survey: Baryon Acoustic Oscillations and the Local Hubble Constant," *Mon. Not. Roy. Astron. Soc.*, vol. 416, pp. 3017–3032, 2011.

[18] C. Blake *et al.*, "The WiggleZ Dark Energy Survey: mapping the distance-redshift relation with baryon acoustic oscillations," *Mon. Not. Roy. Astron. Soc.*, vol. 418, pp. 1707–1724, 2011.

[19] L. Anderson *et al.*, "The clustering of galaxies in the SDSS-III Baryon Oscillation Spectroscopic Survey: Baryon Acoustic Oscillations in the Data Release 9 Spectroscopic Galaxy Sample," *Mon. Not. Roy. Astron. Soc.*, vol. 427, no. 4, pp. 3435–3467, 2013.

[20] A. G. Riess *et al.*, "A 2.4% Determination of the Local Value of the Hubble Constant," *Astrophys. J.*, vol. 826, no. 1, p. 56, 2016.

[21] V. Bonvin *et al.*, "H0LiCOW – V. New COSMOGRAIL time delays of HE 0435-1223: H_0 to 3.8 per cent precision from strong lensing in a flat ΛCDM model," *Mon. Not. Roy. Astron. Soc.*, vol. 465, no. 4, pp. 4914–4930, 2017.

[22] P. A. R. Ade *et al.*, "Planck 2015 results. XIII. Cosmological parameters," *Astron. Astrophys.*, vol. 594, p. A13, 2016.

[23] B. D. Sherwin *et al.*, "Evidence for dark energy from the cosmic microwave background alone using the Atacama Cosmology Telescope lensing measurements," *Phys. Rev. Lett.*, vol. 107, p. 021302, 2011.

[24] A. Aghamousa, J. Hamann, and A. Shafieloo, "A non-parametric consistency test of the ΛCDM model with Planck CMB data," *JCAP*, vol. 1709, no. 09, p. 031, 2017.

[25] N. Aghanim *et al.*, "Planck 2018 results. VI. Cosmological parameters," 2018.

[26] M. Raveri and W. Hu, "Concordance and Discordance in Cosmology," *Phys. Rev.*, vol. D99, no. 4, p. 043506, 2019.

[27] J. L. Bernal, L. Verde, and A. G. Riess, "The trouble with H_0," *JCAP*, vol. 1610, no. 10, p. 019, 2016.

[28] J. Evslin, A. A. Sen, and Ruchika, "Price of shifting the Hubble constant," *Phys. Rev.*, vol. D97, no. 10, p. 103511, 2018.

[29] W. L. Freedman, "Cosmology at a Crossroads," *Nat. Astron.*, vol. 1, p. 0121, 2017.

[30] G. E. Addison, D. J. Watts, C. L. Bennett, M. Halpern, G. Hinshaw, and J. L. Weiland, "Elucidating ΛCDM: Impact of Baryon Acoustic Oscillation Measurements on the Hubble Constant Discrepancy," *Astrophys. J.*, vol. 853, no. 2, p. 119, 2018.

[31] R. A. Battye, T. Charnock, and A. Moss, "Tension between the power spectrum of density perturbations measured on large and small scales," *Phys. Rev.*, vol. D91, no. 10, p. 103508, 2015.

[32] I. G. Mccarthy, S. Bird, J. Schaye, J. Harnois-Deraps, A. S. Font, and L. Van Waerbeke, "The BAHAMAS project: the CMB–large-scale structure tension and the roles of massive neutrinos and galaxy formation," *Mon. Not. Roy. Astron. Soc.*, vol. 476, no. 3, pp. 2999–3030, 2018.

[33] P. A. R. Ade *et al.*, "Planck 2013 results. XX. Cosmology from Sunyaev–Zeldovich cluster counts," *Astron. Astrophys.*, vol. 571, p. A20, 2014.

[34] T. M. C. Abbott *et al.*, "Dark Energy Survey year 1 results: Cosmological constraints from galaxy clustering and weak lensing," *Phys. Rev.*, vol. D98, no. 4, p. 043526, 2018.

[35] H. Hildebrandt *et al.*, "KiDS-450: Cosmological parameter constraints from tomographic weak gravitational lensing," *Mon. Not. Roy. Astron. Soc.*, vol. 465, p. 1454, 2017.

[36] S. Joudaki *et al.*, "KiDS-450: Testing extensions to the standard cosmological model," *Mon. Not. Roy. Astron. Soc.*, vol. 471, no. 2, pp. 1259–1279, 2017.

[37] T. Karwal and M. Kamionkowski, "Dark energy at early times, the Hubble parameter, and the string axiverse," *Phys. Rev.*, vol. D94, no. 10, p. 103523, 2016.

[38] V. Poulin, T. L. Smith, D. Grin, T. Karwal, and M. Kamionkowski, "Cosmological implications of ultralight axionlike fields," *Phys. Rev.*, vol. D98, no. 8, p. 083525, 2018.

[39] V. Poulin, T. L. Smith, T. Karwal, and M. Kamionkowski, "Early Dark Energy Can Resolve The Hubble Tension," 2018.

[40] K. L. Pandey, T. Karwal, and S. Das, "Alleviating the H_0 and σ_8 anomalies with a decaying dark matter model," 2019.

[41] A. G. Riess, S. Casertano, W. Yuan, L. M. Macri, and D. Scolnic, "Large Magellanic Cloud Cepheid Standards Provide a 1% Foundation for the Determination of the Hubble Constant and Stronger Evidence for Physics Beyond LambdaCDM," 2019.

[42] G. E. Addison, Y. Huang, D. J. Watts, C. L. Bennett, M. Halpern, G. Hinshaw, and J. L. Weiland, "Quantifying discordance in the 2015 Planck CMB spectrum," *Astrophys. J.*, vol. 818, no. 2, p. 132, 2016.

[43] N. Aghanim *et al.*, "Planck intermediate results. LI. Features in the cosmic microwave background temperature power spectrum and shifts in cosmological parameters," *Astron. Astrophys.*, vol. 607, p. A95, 2017.

[44] T. Shanks, L. Hogarth, and N. Metcalfe, "GAIA Cepheid parallaxes and 'Local Hole' relieve H_0 tension," *Mon. Not. Roy. Astron. Soc.*, vol. 484, no. 1, pp. L64–L68, 2019.

[45] A. G. Riess, S. Casertano, D. Kenworthy, D. Scolnic, and L. Macri, "Seven Problems with the Claims Related to the Hubble Tension in arXiv:1810.02595," 2018.

[46] J. Soltis, A. Farahi, D. Huterer, and C. M. Liberato, "Percent-Level Test of Isotropic Expansion Using Type Ia Supernovae," *Phys. Rev. Lett.*, vol. 122, no. 9, p. 091301, 2019.

[47] E. Di Valentino, A. Melchiorri, and J. Silk, "Reconciling Planck with the local value of H_0 in extended parameter space," *Phys. Lett.*, vol. B761, pp. 242–246, 2016.

[48] V. Poulin, K. K. Boddy, S. Bird, and M. Kamionkowski, "Implications of an extended dark energy cosmology with massive neutrinos for cosmological tensions," *Phys. Rev.*, vol. D97, no. 12, p. 123504, 2018.

[49] G. Hinshaw *et al.*, "Nine-Year Wilkinson Microwave Anisotropy Probe (WMAP) Observations: Cosmological Parameter Results," *Astrophys. J. Suppl.*, vol. 208, p. 19, 2013.

[50] C. L. Bennett *et al.*, "Seven-Year Wilkinson Microwave Anisotropy Probe (WMAP) Observations: Are There Cosmic Microwave Background Anomalies?" *Astrophys. J. Suppl.*, vol. 192, p. 17, 2011.

[51] P. A. R. Ade *et al.*, "Planck 2013 results. XXIII. Isotropy and statistics of the CMB," *Astron. Astrophys.*, vol. 571, p. A23, 2014.

[52] ——, "Planck 2015 results. XVI. Isotropy and statistics of the CMB," *Astron. Astrophys.*, vol. 594, p. A16, 2016.

[53] W. Hu, "Structure formation with generalized dark matter," *Astrophys. J.*, vol. 506, pp. 485–494, 1998.

[54] D. Blas, J. Lesgourgues, and T. Tram, "The Cosmic Linear Anisotropy Solving System (CLASS) II: Approximation schemes," *JCAP*, vol. 1107, p. 034, 2011.

[55] L. Accardo *et al.*, "High Statistics Measurement of the Positron Fraction in Primary Cosmic Rays of 0.5–500 GeV with the Alpha Magnetic Spectrometer on the International Space Station," *Phys. Rev. Lett.*, vol. 113, p. 121101, 2014.

[56] O. Adriani *et al.*, "An anomalous positron abundance in cosmic rays with energies 1.5-100 GeV," *Nature*, vol. 458, pp. 607–609, 2009.

[57] I. Cholis, G. Dobler, D. P. Finkbeiner, L. Goodenough, and N. Weiner, "The Case for a 700+ GeV WIMP: Cosmic Ray Spectra from ATIC and PAMELA," *Phys. Rev.*, vol. D80, p. 123518, 2009.

[58] I. Cholis, L. Goodenough, D. Hooper, M. Simet, and N. Weiner, "High Energy Positrons From Annihilating Dark Matter," *Phys. Rev.*, vol. D80, p. 123511, 2009.

[59] N. Arkani-Hamed, D. P. Finkbeiner, T. R. Slatyer, and N. Weiner, "A Theory of Dark Matter," *Phys. Rev.*, vol. D79, p. 015014, 2009.

[60] I. Cholis, D. P. Finkbeiner, L. Goodenough, and N. Weiner, "The PAMELA Positron Excess from Annihilations into a Light Boson," *JCAP*, vol. 0912, p. 007, 2009.

[61] I. Cholis, T. Karwal, and M. Kamionkowski, "Features in the Spectrum of Cosmic-Ray Positrons from Pulsars," *Phys. Rev.*, vol. D97, no. 12, p. 123011, 2018.

[62] ——, "Studying the Milky Way pulsar population with cosmic-ray leptons," *Phys. Rev.*, vol. D98, no. 6, p. 063008, 2018.

[63] A. U. Abeysekara *et al.*, "Extended gamma-ray sources around pulsars constrain the origin of the positron flux at Earth," *Science*, vol. 358, no. 6365, pp. 911–914, 2017.

[64] D. Hooper, I. Cholis, T. Linden, and K. Fang, "HAWC Observations Strongly Favor Pulsar Interpretations of the Cosmic-Ray Positron Excess," *Phys. Rev.*, vol. D96, no. 10, p. 103013, 2017.

[65] T. Linden, K. Auchettl, J. Bramante, I. Cholis, K. Fang, D. Hooper, T. Karwal, and S. W. Li, "Using HAWC to discover invisible pulsars," *Phys. Rev.*, vol. D96, no. 10, p. 103016, 2017.

[66] D. Hooper, I. Cholis, and T. Linden, "TeV Gamma Rays From Galactic Center Pulsars," *Phys. Dark Univ.*, vol. 21, pp. 40–46, 2018.

[67] M. A. Livingstone, V. M. Kaspi, and F. P. Gavriil, "Long-term phase-coherent x-ray timing of PSR B0540-69," *Astrophys. J.*, vol. 633, pp. 1095–1100, 2005.

[68] F. Camilo, V. M. Kaspi, A. G. Lyne, R. N. Manchester, J. F. Bell, N. D'Amico, N. P. F. McKay, and F. Crawford, "Discovery of two high-magnetic-field radio pulsars," *Astrophys. J.*, vol. 541, p. 367, 2000.

[69] M. A. Livingstone, V. M. Kaspi, F. P. Gavriil, and R. N. Manchester, "21 years of timing PSR B1509-58," *Astrophys. J.*, vol. 619, pp. 1046–1053, 2005.

[70] S. Birrer *et al.*, "H0LiCOW - IX. Cosmographic analysis of the doubly imaged quasar SDSS 1206+4332 and a new measurement of the Hubble constant," *Mon. Not. Roy. Astron. Soc.*, vol. 484, p. 4726, 2019.

[71] G. Efstathiou, "H0 Revisited," *Mon. Not. Roy. Astron. Soc.*, vol. 440, no. 2, pp. 1138–1152, 2014.

[72] K. Aylor, M. Joy, L. Knox, M. Millea, S. Raghunathan, and W. L. K. Wu, "Sounds Discordant: Classical Distance Ladder & ΛCDM -based Determinations of the Cosmological Sound Horizon," *Astrophys. J.*, vol. 874, no. 1, p. 4, 2019.

[73] S. M. Feeney, D. J. Mortlock, and N. Dalmasso, "Clarifying the Hubble constant tension with a Bayesian hierarchical model of the local distance ladder," *Mon. Not. Roy. Astron. Soc.*, vol. 476, no. 3, pp. 3861–3882, 2018.

[74] E. Di Valentino, A. Melchiorri, E. V. Linder, and J. Silk, "Constraining Dark Energy Dynamics in Extended Parameter Space," *Phys. Rev.*, vol. D96, no. 2, p. 023523, 2017.

[75] E. Di Valentino, E. V. Linder, and A. Melchiorri, "Vacuum phase transition solves the H_0 tension," *Phys. Rev.*, vol. D97, no. 4, p. 043528, 2018.

[76] N. Khosravi, S. Baghram, N. Afshordi, and N. Altamirano, "üΛCDM: H_0 tension as a hint for Über-Gravity," 2017.

[77] A. Banihashemi, N. Khosravi, and A. H. Shirazi, "Ginzburg-Landau Theory of Dark Energy: A Framework to Study Both Temporal and Spatial Cosmological Tensions Simultaneously," *Phys. Rev.*, vol. D99, no. 8, p. 083509, 2019.

[78] S. Kumar and R. C. Nunes, "Probing the interaction between dark matter and dark energy in the presence of massive neutrinos," *Phys. Rev.*, vol. D94, no. 12, p. 123511, 2016.

[79] E. Di Valentino, A. Melchiorri, and O. Mena, "Can interacting dark energy solve the H_0 tension?" *Phys. Rev.*, vol. D96, no. 4, p. 043503, 2017.

[80] A. J. Ross, L. Samushia, C. Howlett, W. J. Percival, A. Burden, and M. Manera, "The

clustering of the SDSS DR7 main Galaxy sample – I. A 4 per cent distance measure at $z = 0.15$," *Mon. Not. Roy. Astron. Soc.*, vol. 449, no. 1, pp. 835–847, 2015.

[81] S. Alam *et al.*, "The clustering of galaxies in the completed SDSS-III Baryon Oscillation Spectroscopic Survey: cosmological analysis of the DR12 galaxy sample," *Mon. Not. Roy. Astron. Soc.*, vol. 470, no. 3, pp. 2617–2652, 2017.

[82] G.-B. Zhao *et al.*, "Dynamical dark energy in light of the latest observations," *Nat. Astron.*, vol. 1, no. 9, pp. 627–632, 2017.

[83] A. G. Riess *et al.*, "Milky Way Cepheid Standards for Measuring Cosmic Distances and Application to Gaia DR2: Implications for the Hubble Constant," *Astrophys. J.*, vol. 861, no. 2, p. 126, 2018.

[84] A. Barreira, B. Li, C. Baugh, and S. Pascoli, "The observational status of Galileon gravity after Planck," *JCAP*, vol. 1408, p. 059, 2014.

[85] C. Umiltà, M. Ballardini, F. Finelli, and D. Paoletti, "CMB and BAO constraints for an induced gravity dark energy model with a quartic potential," *JCAP*, vol. 1508, p. 017, 2015.

[86] M. Ballardini, F. Finelli, C. Umiltà, and D. Paoletti, "Cosmological constraints on induced gravity dark energy models," *JCAP*, vol. 1605, no. 05, p. 067, 2016.

[87] J. Renk, M. Zumalacárregui, F. Montanari, and A. Barreira, "Galileon gravity in light of ISW, CMB, BAO and H_0 data," *JCAP*, vol. 1710, no. 10, p. 020, 2017.

[88] E. Belgacem, Y. Dirian, S. Foffa, and M. Maggiore, "Nonlocal gravity. Conceptual aspects and cosmological predictions," *JCAP*, vol. 1803, no. 03, p. 002, 2018.

[89] R. C. Nunes, "Structure formation in $f(T)$ gravity and a solution for H_0 tension," *JCAP*, vol. 1805, no. 05, p. 052, 2018.

[90] M.-X. Lin, M. Raveri, and W. Hu, "Phenomenology of Modified Gravity at Recombination," *Phys. Rev.*, vol. D99, no. 4, p. 043514, 2019.

[91] P. Svrcek and E. Witten, "Axions In String Theory," *JHEP*, vol. 06, p. 051, 2006.

[92] P. Svrcek, "Cosmological Constant and Axions in String Theory," *Submitted to: JHEP*, 2006.

[93] A. Arvanitaki, S. Dimopoulos, S. Dubovsky, N. Kaloper, and J. March-Russell, "String Axiverse," *Phys. Rev.*, vol. D81, p. 123530, 2010.

[94] D. J. E. Marsh, "The Axiverse Extended: Vacuum Destabilisation, Early Dark Energy and Cosmological Collapse," *Phys. Rev.*, vol. D83, p. 123526, 2011.

[95] M. Kamionkowski, J. Pradler, and D. G. E. Walker, "Dark energy from the string axiverse," *Phys. Rev. Lett.*, vol. 113, no. 25, p. 251302, 2014.

[96] E. Mörtsell and S. Dhawan, "Does the Hubble constant tension call for new physics?" *JCAP*, vol. 1809, no. 09, p. 025, 2018.

[97] N. Aghanim *et al.*, "Planck intermediate results. XLVI. Reduction of large-scale sys-

tematic effects in HFI polarization maps and estimation of the reionization optical depth," *Astron. Astrophys.*, vol. 596, p. A107, 2016.

[98] M. Doran and G. Robbers, "Early dark energy cosmologies," *JCAP*, vol. 0606, p. 026, 2006.

[99] V. Pettorino, L. Amendola, and C. Wetterich, "How early is early dark energy?" *Phys. Rev.*, vol. D87, p. 083009, 2013.

[100] E. Calabrese, D. Huterer, E. V. Linder, A. Melchiorri, and L. Pagano, "Limits on Dark Radiation, Early Dark Energy, and Relativistic Degrees of Freedom," *Phys. Rev.*, vol. D83, p. 123504, 2011.

[101] R. R. Caldwell, R. Dave, and P. J. Steinhardt, "Cosmological imprint of an energy component with general equation of state," *Phys. Rev. Lett.*, vol. 80, pp. 1582–1585, 1998.

[102] G. Jungman, M. Kamionkowski, A. Kosowsky, and D. N. Spergel, "Cosmological parameter determination with microwave background maps," *Phys. Rev.*, vol. D54, pp. 1332–1344, 1996.

[103] M. Tegmark, A. Taylor, and A. Heavens, "Karhunen-Loeve eigenvalue problems in cosmology: How should we tackle large data sets?" *Astrophys. J.*, vol. 480, p. 22, 1997.

[104] S. Galli, K. Benabed, F. Bouchet, J.-F. Cardoso, F. Elsner, E. Hivon, A. Mangilli,

S. Prunet, and B. Wandelt, "CMB Polarization can constrain cosmology better than CMB temperature," *Phys. Rev.*, vol. D90, no. 6, p. 063504, 2014.

[105] J. B. Muñoz, D. Grin, L. Dai, M. Kamionkowski, and E. D. Kovetz, "Search for Compensated Isocurvature Perturbations with Planck Power Spectra," *Phys. Rev.*, vol. D93, no. 4, p. 043008, 2016.

[106] M. Zaldarriaga, "Polarization of the microwave background in reionized models," *Phys. Rev.*, vol. D55, pp. 1822–1829, 1997.

[107] D. Coe, "Fisher Matrices and Confidence Ellipses: A Quick-Start Guide and Software," 2009.

[108] P. A. R. Ade *et al.*, "Planck 2013 results. XV. CMB power spectra and likelihood," *Astron. Astrophys.*, vol. 571, p. A15, 2014.

[109] S. Grandis, D. Rapetti, A. Saro, J. J. Mohr, and J. P. Dietrich, "Quantifying tensions between CMB and distance data sets in models with free curvature or lensing amplitude," *Mon. Not. Roy. Astron. Soc.*, vol. 463, no. 2, pp. 1416–1430, 2016.

[110] M. Archidiacono, S. Gariazzo, C. Giunti, S. Hannestad, R. Hansen, M. Laveder, and T. Tram, "Pseudoscalar—sterile neutrino interactions: reconciling the cosmos with neutrino oscillations," *JCAP*, vol. 1608, no. 08, p. 067, 2016.

[111] Z. Huang, "Observational effects of a running Planck mass," *Phys. Rev.*, vol. D93, no. 4, p. 043538, 2016.

[112] P. A. R. Ade *et al.*, "Planck 2015 results. XIV. Dark energy and modified gravity," *Astron. Astrophys.*, vol. 594, p. A14, 2016.

[113] D. J. E. Marsh, "Axion Cosmology," *Phys. Rept.*, vol. 643, pp. 1–79, 2016.

[114] R. Kappl, H. P. Nilles, and M. W. Winkler, "Modulated Natural Inflation," *Phys. Lett.*, vol. B753, pp. 653–659, 2016.

[115] M. S. Turner, "Coherent Scalar Field Oscillations in an Expanding Universe," *Phys. Rev.*, vol. D28, p. 1243, 1983.

[116] K. Griest, "Toward a possible solution to the cosmic coincidence problem," *Phys. Rev.*, vol. D66, p. 123501, 2002.

[117] E. V. Linder and T. L. Smith, "Dark Before Light: Testing the Cosmic Expansion History through the Cosmic Microwave Background," *JCAP*, vol. 1104, p. 001, 2011.

[118] R. Emami, D. Grin, J. Pradler, A. Raccanelli, and M. Kamionkowski, "Cosmological tests of an axiverse-inspired quintessence field," *Phys. Rev.*, vol. D93, no. 12, p. 123005, 2016.

[119] J. C. Hill and E. J. Baxter, "Can Early Dark Energy Explain EDGES?" *JCAP*, vol. 1808, no. 08, p. 037, 2018.

[120] J. D. Bowman, A. E. E. Rogers, R. A. Monsalve, T. J. Mozdzen, and N. Mahesh, "An absorption profile centred at 78 megahertz in the sky-averaged spectrum," *Nature*, vol. 555, no. 7694, pp. 67–70, 2018.

[121] R. Hills, G. Kulkarni, P. D. Meerburg, and E. Puchwein, "Concerns about modelling of the EDGES data," *Nature*, vol. 564, no. 7736, pp. E32–E34, 2018.

[122] M. J. Stott, D. J. E. Marsh, C. Pongkitivanichkul, L. C. Price, and B. S. Acharya, "Spectrum of the axion dark sector," *Phys. Rev.*, vol. D96, no. 8, p. 083510, 2017.

[123] R. Hlozek, D. Grin, D. J. E. Marsh, and P. G. Ferreira, "A search for ultralight axions using precision cosmological data," *Phys. Rev.*, vol. D91, no. 10, p. 103512, 2015.

[124] S. Mukherjee, R. Khatri, and B. D. Wandelt, "Polarized anisotropic spectral distortions of the CMB: Galactic and extragalactic constraints on photon-axion conversion," *JCAP*, vol. 1804, p. 045, 2018.

[125] W. Hu, R. Barkana, and A. Gruzinov, "Cold and fuzzy dark matter," *Phys. Rev. Lett.*, vol. 85, pp. 1158–1161, 2000.

[126] J.-c. Hwang and H. Noh, "Axion as a Cold Dark Matter candidate," *Phys. Lett.*, vol. B680, pp. 1–3, 2009.

[127] D. J. E. Marsh and P. G. Ferreira, "Ultra-Light Scalar Fields and the Growth of Structure in the Universe," *Phys. Rev.*, vol. D82, p. 103528, 2010.

[128] C.-G. Park, J.-c. Hwang, and H. Noh, "Axion as a cold dark matter candidate: low-mass case," *Phys. Rev.*, vol. D86, p. 083535, 2012.

[129] H. Noh, J.-c. Hwang, and C.-G. Park, "Axion as a cold dark matter candidate: Proof to fully nonlinear order," *Astrophys. J.*, vol. 846, no. 1, p. 1, 2017.

[130] M. Betoule *et al.*, "Improved cosmological constraints from a joint analysis of the SDSS-II and SNLS supernova samples," *Astron. Astrophys.*, vol. 568, p. A22, 2014.

[131] J. Lesgourgues, "The Cosmic Linear Anisotropy Solving System (CLASS) I: Overview," 2011.

[132] ——, "The Cosmic Linear Anisotropy Solving System (CLASS) III: Comparision with CAMB for LambdaCDM," 2011.

[133] J. Lesgourgues and T. Tram, "The Cosmic Linear Anisotropy Solving System (CLASS) IV: efficient implementation of non-cold relics," *JCAP*, vol. 1109, p. 032, 2011.

[134] B. Audren, J. Lesgourgues, K. Benabed, and S. Prunet, "Conservative Constraints on Early Cosmology: an illustration of the Monte Python cosmological parameter inference code," *JCAP*, vol. 1302, p. 001, 2013.

[135] G. Ballesteros and J. Lesgourgues, "Dark energy with non-adiabatic sound speed: initial conditions and detectability," *JCAP*, vol. 1010, p. 014, 2010.

[136] E. Aubourg *et al.*, "Cosmological implications of baryon acoustic oscillation measurements," *Phys. Rev.*, vol. D92, no. 12, p. 123516, 2015.

[137] C. Dvorkin, M. Wyman, D. H. Rudd, and W. Hu, "Neutrinos help reconcile Planck measurements with both the early and local Universe," *Phys. Rev.*, vol. D90, no. 8, p. 083503, 2014.

[138] M. Wyman, D. H. Rudd, R. A. Vanderveld, and W. Hu, "Neutrinos Help Reconcile

Planck Measurements with the Local Universe," *Phys. Rev. Lett.*, vol. 112, no. 5, p. 051302, 2014.

[139] B. Leistedt, H. V. Peiris, and L. Verde, "No new cosmological concordance with massive sterile neutrinos," *Phys. Rev. Lett.*, vol. 113, p. 041301, 2014.

[140] A. Ewall-Wice, T. C. Chang, J. Lazio, O. Dore, M. Seiffert, and R. A. Monsalve, "Modeling the Radio Background from the First Black Holes at Cosmic Dawn: Implications for the 21 cm Absorption Amplitude," *Astrophys. J.*, vol. 868, no. 1, p. 63, 2018.

[141] J. Mirocha and S. R. Furlanetto, "What does the first highly-redshifted 21-cm detection tell us about early galaxies?" *Mon. Not. Roy. Astron. Soc.*, vol. 483, no. 2, pp. 1980–1992, 2019.

[142] M. Pospelov, J. Pradler, J. T. Ruderman, and A. Urbano, "Room for New Physics in the Rayleigh-Jeans Tail of the Cosmic Microwave Background," *Phys. Rev. Lett.*, vol. 121, no. 3, p. 031103, 2018.

[143] R. Barkana, "Possible interaction between baryons and dark-matter particles revealed by the first stars," *Nature*, vol. 555, no. 7694, pp. 71–74, 2018.

[144] A. A. Costa, R. C. G. Landim, B. Wang, and E. Abdalla, "Interacting Dark Energy: Possible Explanation for 21-cm Absorption at Cosmic Dawn," *Eur. Phys. J.*, vol. C78, no. 9, p. 746, 2018.

[145] S. Seager, D. D. Sasselov, and D. Scott, "How exactly did the universe become neu-

tral?" *Astrophys. J. Suppl.*, vol. 128, pp. 407–430, 2000.

[146] ——, "A new calculation of the recombination epoch," *Astrophys. J.*, vol. 523, pp. L1–L5, 1999.

[147] Y. Ali-Haimoud and C. M. Hirata, "HyRec: A fast and highly accurate primordial hydrogen and helium recombination code," *Phys. Rev.*, vol. D83, p. 043513, 2011.

[148] D. M. Scolnic *et al.*, "The Complete Light-curve Sample of Spectroscopically Confirmed SNe Ia from Pan-STARRS1 and Cosmological Constraints from the Combined Pantheon Sample," *Astrophys. J.*, vol. 859, no. 2, p. 101, 2018.

[149] A. Hojjati, E. V. Linder, and J. Samsing, "New Constraints on the Early Expansion History of the Universe," *Phys. Rev. Lett.*, vol. 111, no. 4, p. 041301, 2013.

[150] M. S. Turner and A. G. Riess, "Do SNe Ia provide direct evidence for past deceleration of the universe?" *Astrophys. J.*, vol. 569, p. 18, 2002.

[151] T. Brinckmann and J. Lesgourgues, "MontePython 3: boosted MCMC sampler and other features," 2018.

[152] J. Aguirre *et al.*, "The Simons Observatory: Science goals and forecasts," *JCAP*, vol. 1902, p. 056, 2019.

[153] N. Aghanim *et al.*, "Planck 2015 results. XI. CMB power spectra, likelihoods, and robustness of parameters," *Astron. Astrophys.*, vol. 594, p. A11, 2016.

[154] A. Lewis, "Efficient sampling of fast and slow cosmological parameters," *Phys. Rev.*,

vol. D87, no. 10, p. 103529, 2013.

[155] A. Gelman and D. B. Rubin, "Inference from Iterative Simulation Using Multiple Sequences," *Statist. Sci.*, vol. 7, pp. 457–472, 1992.

[156] W. Hu, M. Fukugita, M. Zaldarriaga, and M. Tegmark, "CMB observables and their cosmological implications," *Astrophys. J.*, vol. 549, p. 669, 2001.

[157] Z. Hou, R. Keisler, L. Knox, M. Millea, and C. Reichardt, "How Massless Neutrinos Affect the Cosmic Microwave Background Damping Tail," *Phys. Rev.*, vol. D87, p. 083008, 2013.

[158] K. N. Abazajian *et al.*, "CMB-S4 Science Book, First Edition," 2016.

[159] E. Di Valentino *et al.*, "Exploring cosmic origins with CORE: Cosmological parameters," *JCAP*, vol. 1804, p. 017, 2018.

[160] T. Essinger-Hileman *et al.*, "CLASS: The Cosmology Large Angular Scale Surveyor," *Proc. SPIE Int. Soc. Opt. Eng.*, vol. 9153, p. 91531I, 2014.

[161] A. Suzuki *et al.*, "The LiteBIRD Satellite Mission - Sub-Kelvin Instrument," *J. Low. Temp. Phys.*, vol. 193, no. 5-6, pp. 1048–1056, 2018.

[162] B. A. Reid *et al.*, "Cosmological Constraints from the Clustering of the Sloan Digital Sky Survey DR7 Luminous Red Galaxies," *Mon. Not. Roy. Astron. Soc.*, vol. 404, pp. 60–85, 2010.

[163] F. Köhlinger *et al.*, "KiDS-450: The tomographic weak lensing power spectrum and

constraints on cosmological parameters," *Mon. Not. Roy. Astron. Soc.*, vol. 471, no. 4, pp. 4412–4435, 2017.

[164] M. Cicoli, M. Goodsell, and A. Ringwald, "The type IIB string axiverse and its low-energy phenomenology," *JHEP*, vol. 10, p. 146, 2012.

[165] S. Dodelson, M. Kaplinghat, and E. Stewart, "Solving the coincidence problem : Tracking oscillating energy," *Phys. Rev. Lett.*, vol. 85, pp. 5276–5279, 2000.

[166] M. Ata *et al.*, "The clustering of the SDSS-IV extended Baryon Oscillation Spectroscopic Survey DR14 quasar sample: first measurement of baryon acoustic oscillations between redshift 0.8 and 2.2," *Mon. Not. Roy. Astron. Soc.*, vol. 473, no. 4, pp. 4773–4794, 2018.

[167] S. Joudaki *et al.*, "CFHTLenS revisited: assessing concordance with Planck including astrophysical systematics," *Mon. Not. Roy. Astron. Soc.*, vol. 465, no. 2, pp. 2033–2052, 2017.

[168] K. Enqvist, S. Nadathur, T. Sekiguchi, and T. Takahashi, "Decaying dark matter and the tension in σ_8," *JCAP*, vol. 1509, no. 09, p. 067, 2015.

[169] E. Di Valentino and S. Bridle, "Exploring the Tension between Current Cosmic Microwave Background and Cosmic Shear Data," *Symmetry*, vol. 10, no. 11, p. 585, 2018.

[170] O. Eggers Bjaelde, S. Das, and A. Moss, "Origin of ΔN_{eff} as a result of an interaction

between dark radiation and dark matter," *Journal of Cosmology and Astro-Particle Physics*, vol. 2012, no. 10, p. 017, Oct 2012.

[171] M. G. Aartsen *et al.*, "Searches for Sterile Neutrinos with the IceCube Detector," *Phys. Rev. Lett.*, vol. 117, no. 7, p. 071801, 2016.

[172] J. Valiviita, E. Majerotto, and R. Maartens, "Instability in interacting dark energy and dark matter fluids," *JCAP*, vol. 0807, p. 020, 2008.

[173] V. Poulin, P. D. Serpico, and J. Lesgourgues, "A fresh look at linear cosmological constraints on a decaying dark matter component," *JCAP*, vol. 1608, no. 08, p. 036, 2016.

[174] J. Lesgourgues, G. Marques-Tavares, and M. Schmaltz, "Evidence for dark matter interactions in cosmological precision data?" *JCAP*, vol. 1602, no. 02, p. 037, 2016.

[175] M. A. Buen-Abad, M. Schmaltz, J. Lesgourgues, and T. Brinckmann, "Interacting Dark Sector and Precision Cosmology," *JCAP*, vol. 1801, no. 01, p. 008, 2018.

[176] Z. Chacko, Y. Cui, S. Hong, T. Okui, and Y. Tsai, "Partially Acoustic Dark Matter, Interacting Dark Radiation, and Large Scale Structure," *JHEP*, vol. 12, p. 108, 2016.

[177] T. Bringmann, F. Kahlhoefer, K. Schmidt-Hoberg, and P. Walia, "Converting non-relativistic dark matter to radiation," *Phys. Rev.*, vol. D98, no. 2, p. 023543, 2018.

[178] M.-Y. Wang and A. R. Zentner, "Effects of Unstable Dark Matter on Large-Scale Structure and Constraints from Future Surveys," *Phys. Rev.*, vol. D85, p. 043514, 2012.

[179] G. Mangano, G. Miele, S. Pastor, and M. Peloso, "A Precision calculation of the effective number of cosmological neutrinos," *Phys. Lett.*, vol. B534, pp. 8–16, 2002.

[180] W. Hu, N. Sugiyama, and J. Silk, "The Physics of microwave background anisotropies," *Nature*, vol. 386, pp. 37–43, 1997.

[181] J. Lesgourgues and S. Pastor, "Massive neutrinos and cosmology," *Phys. Rept.*, vol. 429, pp. 307–379, 2006.

[182] A. Lewis, A. Challinor, and A. Lasenby, "Efficient computation of CMB anisotropies in closed FRW models," *Astrophys. J.*, vol. 538, pp. 473–476, 2000.

[183] A. Lewis and S. Bridle, "Cosmological parameters from CMB and other data: A Monte Carlo approach," *Phys. Rev.*, vol. D66, p. 103511, 2002.

[184] P. Serra, F. Zalamea, A. Cooray, G. Mangano, and A. Melchiorri, "Constraints on neutrino – dark matter interactions from cosmic microwave background and large scale structure data," *Phys. Rev.*, vol. D81, p. 043507, 2010.

[185] F.-Y. Cyr-Racine, R. de Putter, A. Raccanelli, and K. Sigurdson, "Constraints on Large-Scale Dark Acoustic Oscillations from Cosmology," *Phys. Rev.*, vol. D89, no. 6, p. 063517, 2014.

[186] S. Das, R. Mondal, V. Rentala, and S. Suresh, "On dark matter - dark radiation interaction and cosmic reionization," *JCAP*, vol. 1808, no. 08, p. 045, 2018.

[187] R. J. Wilkinson, C. Boehm, and J. Lesgourgues, "Constraining Dark Matter-Neutrino

Interactions using the CMB and Large-Scale Structure," *JCAP*, vol. 1405, p. 011, 2014.

[188] M. Kunz, S. Nesseris, and I. Sawicki, "Constraints on dark-matter properties from large-scale structure," *Phys. Rev.*, vol. D94, no. 2, p. 023510, 2016.

[189] M. Kopp, C. Skordis, and D. B. Thomas, "Extensive investigation of the generalized dark matter model," *Phys. Rev.*, vol. D94, no. 4, p. 043512, 2016.

[190] C.-P. Ma and E. Bertschinger, "Cosmological perturbation theory in the synchronous and conformal Newtonian gauges," *Astrophys. J.*, vol. 455, pp. 7–25, 1995.

[191] W. Hu, D. Scott, N. Sugiyama, and M. J. White, "The Effect of physical assumptions on the calculation of microwave background anisotropies," *Phys. Rev.*, vol. D52, pp. 5498–5515, 1995.

[192] G. Efstathiou, "Principal component analysis of the cosmic microwave background anisotropies: revealing the tensor degeneracy," *Mon. Not. Roy. Astron. Soc.*, vol. 332, p. 193, 2002.

[193] W.-M. Dai, Z.-K. Guo, and R.-G. Cai, "Principal component analysis of the reionization history from Planck 2015 data," *Phys. Rev.*, vol. D92, no. 12, p. 123521, 2015.

[194] S. M. Leach, "Measuring the primordial power spectrum: Principal component analysis of the cosmic microwave background," *Mon. Not. Roy. Astron. Soc.*, vol. 372, pp. 646–654, 2006.

[195] S. Mitra, T. R. Choudhury, and A. Ferrara, "Reionization constraints using Principal Component Analysis," *Mon. Not. Roy. Astron. Soc.*, vol. 413, p. 1569, 2011.

[196] M. J. Mortonson and W. Hu, "Model-independent constraints on reionization from large-scale CMB polarization," *Astrophys. J.*, vol. 672, pp. 737–751, 2008.

[197] C. H. Heinrich, V. Miranda, and W. Hu, "Complete Reionization Constraints from Planck 2015 Polarization," *Phys. Rev.*, vol. D95, no. 2, p. 023513, 2017.

[198] C. R. Contaldi, M. Peloso, L. Kofman, and A. D. Linde, "Suppressing the lower multipoles in the CMB anisotropies," *JCAP*, vol. 0307, p. 002, 2003.

[199] S. Das and T. Souradeep, "Suppressing CMB low multipoles with ISW effect," *JCAP*, vol. 1402, p. 002, 2014.

[200] M. Aguilar *et al.*, "Towards Understanding the Origin of Cosmic-Ray Positrons," *Phys. Rev. Lett.*, vol. 122, no. 4, p. 041102, 2019.

[201] I. V. Moskalenko, A. W. Strong, J. F. Ormes, and M. S. Potgieter, "Secondary antiprotons and propagation of cosmic rays in the galaxy and heliosphere," *Astrophys. J.*, vol. 565, pp. 280–296, 2002.

[202] M. Kachelriess, I. V. Moskalenko, and S. S. Ostapchenko, "New calculation of antiproton production by cosmic ray protons and nuclei," *Astrophys. J.*, vol. 803, no. 2, p. 54, 2015.

[203] A. W. Strong, "Recent extensions to GALPROP," vol. 34, p. 506, 2015.

[204] C. Evoli, D. Gaggero, D. Grasso, and L. Maccione, "Cosmic-Ray Nuclei, Antiprotons and Gamma-rays in the Galaxy: a New Diffusion Model," *JCAP*, vol. 0810, p. 018, 2008, [Erratum: JCAP1604,no.04,E01(2016)].

[205] C. Evoli, I. Cholis, D. Grasso, L. Maccione, and P. Ullio, "Antiprotons from dark matter annihilation in the Galaxy: astrophysical uncertainties," *Phys. Rev.*, vol. D85, p. 123511, 2012.

[206] M. Pato, D. Hooper, and M. Simet, "Pinpointing Cosmic Ray Propagation With The AMS-02 Experiment," *JCAP*, vol. 1006, p. 022, 2010.

[207] G. Di Bernardo, C. Evoli, D. Gaggero, D. Grasso, L. Maccione, and M. N. Mazziotta, "Implications of the Cosmic Ray Electron Spectrum and Anisotropy measured with Fermi-LAT," *Astropart. Phys.*, vol. 34, pp. 528–538, 2011.

[208] P. Blasi, "The origin of the positron excess in cosmic rays," *Phys. Rev. Lett.*, vol. 103, p. 051104, 2009.

[209] P. Mertsch and S. Sarkar, "Testing astrophysical models for the PAMELA positron excess with cosmic ray nuclei," *Phys. Rev. Lett.*, vol. 103, p. 081104, 2009.

[210] M. Ahlers, P. Mertsch, and S. Sarkar, "On cosmic ray acceleration in supernova remnants and the FERMI/PAMELA data," *Phys. Rev.*, vol. D80, p. 123017, 2009.

[211] P. Blasi and P. D. Serpico, "High-energy antiprotons from old supernova remnants," *Phys. Rev. Lett.*, vol. 103, p. 081103, 2009.

[212] N. Kawanaka, K. Ioka, Y. Ohira, and K. Kashiyama, "TeV Electron Spectrum for

Probing Cosmic-Ray Escape from a Supernova Remnant," *Astrophys. J.*, vol. 729, p. 93, 2011.

[213] Y. Fujita, K. Kohri, R. Yamazaki, and K. Ioka, "Is the PAMELA anomaly caused by the supernova explosions near the Earth?" *Phys. Rev.*, vol. D80, p. 063003, 2009.

[214] I. Cholis and D. Hooper, "Constraining the origin of the rising cosmic ray positron fraction with the boron-to-carbon ratio," *Phys. Rev.*, vol. D89, no. 4, p. 043013, 2014.

[215] P. Mertsch and S. Sarkar, "AMS-02 data confront acceleration of cosmic ray secondaries in nearby sources," *Phys. Rev.*, vol. D90, p. 061301, 2014.

[216] M. Di Mauro, F. Donato, N. Fornengo, R. Lineros, and A. Vittino, "Interpretation of AMS-02 electrons and positrons data," *JCAP*, vol. 1404, p. 006, 2014.

[217] K. Kohri, K. Ioka, Y. Fujita, and R. Yamazaki, "Can we explain AMS-02 antiproton and positron excesses simultaneously by nearby supernovae without pulsars or dark matter?" *PTEP*, vol. 2016, no. 2, p. 021E01, 2016.

[218] A. M. Atoian, F. A. Aharonian, and H. J. Volk, "Electrons and positrons in the galactic cosmic rays," *Phys. Rev.*, vol. D52, pp. 3265–3275, 1995.

[219] D. Hooper, P. Blasi, and P. D. Serpico, "Pulsars as the Sources of High Energy Cosmic Ray Positrons," *JCAP*, vol. 0901, p. 025, 2009.

[220] H. Yuksel, M. D. Kistler, and T. Stanev, "TeV Gamma Rays from Geminga and the Origin of the GeV Positron Excess," *Phys. Rev. Lett.*, vol. 103, p. 051101, 2009.

[221] S. Profumo, "Dissecting cosmic-ray electron-positron data with Occam's Razor: the role of known Pulsars," *Central Eur. J. Phys.*, vol. 10, pp. 1–31, 2011.

[222] D. Malyshev, I. Cholis, and J. Gelfand, "Pulsars versus Dark Matter Interpretation of ATIC/PAMELA," *Phys. Rev.*, vol. D80, p. 063005, 2009.

[223] N. Kawanaka, K. Ioka, and M. M. Nojiri, "Cosmic-Ray Electron Excess from Pulsars is Spiky or Smooth?: Continuous and Multiple Electron/Positron injections," *Astrophys. J.*, vol. 710, pp. 958–963, 2010.

[224] D. Grasso *et al.*, "On possible interpretations of the high energy electron-positron spectrum measured by the Fermi Large Area Telescope," *Astropart. Phys.*, vol. 32, pp. 140–151, 2009.

[225] T. Linden and S. Profumo, "Probing the Pulsar Origin of the Anomalous Positron Fraction with AMS-02 and Atmospheric Cherenkov Telescopes," *Astrophys. J.*, vol. 772, p. 18, 2013.

[226] I. Cholis and D. Hooper, "Dark Matter and Pulsar Origins of the Rising Cosmic Ray Positron Fraction in Light of New Data From AMS," *Phys. Rev.*, vol. D88, p. 023013, 2013.

[227] Q. Yuan, X.-J. Bi, G.-M. Chen, Y.-Q. Guo, S.-J. Lin, and X. Zhang, "Implications of the AMS-02 positron fraction in cosmic rays," *Astropart. Phys.*, vol. 60, pp. 1–12, 2015.

[228] P.-F. Yin, Z.-H. Yu, Q. Yuan, and X.-J. Bi, "Pulsar interpretation for the AMS-02

result," *Phys. Rev.*, vol. D88, no. 2, p. 023001, 2013.

[229] L. Bergstrom, T. Bringmann, and J. Edsjo, "New Positron Spectral Features from Supersymmetric Dark Matter - a Way to Explain the PAMELA Data?" *Phys. Rev.*, vol. D78, p. 103520, 2008.

[230] M. Cirelli and A. Strumia, "Minimal Dark Matter predictions and the PAMELA positron excess," *PoS*, vol. IDM2008, p. 089, 2008.

[231] M. Cirelli, M. Kadastik, M. Raidal, and A. Strumia, "Model-independent implications of the e+-, anti-proton cosmic ray spectra on properties of Dark Matter," *Nucl. Phys.*, vol. B813, pp. 1–21, 2009, [Addendum: Nucl. Phys.B873,530(2013)].

[232] A. E. Nelson and C. Spitzer, "Slightly Non-Minimal Dark Matter in PAMELA and ATIC," *JHEP*, vol. 10, p. 066, 2010.

[233] R. Harnik and G. D. Kribs, "An Effective Theory of Dirac Dark Matter," *Phys. Rev.*, vol. D79, p. 095007, 2009.

[234] P. J. Fox and E. Poppitz, "Leptophilic Dark Matter," *Phys. Rev.*, vol. D79, p. 083528, 2009.

[235] M. Pospelov and A. Ritz, "Astrophysical Signatures of Secluded Dark Matter," *Phys. Lett.*, vol. B671, pp. 391–397, 2009.

[236] J. D. March-Russell and S. M. West, "WIMPonium and Boost Factors for Indirect Dark Matter Detection," *Phys. Lett.*, vol. B676, pp. 133–139, 2009.

[237] S. Chang and L. Goodenough, "Charge Asymmetric Cosmic Ray Signals From Dark Matter Decay," *Phys. Rev.*, vol. D84, p. 023524, 2011.

[238] K. R. Dienes, J. Kumar, and B. Thomas, "Dynamical Dark Matter and the positron excess in light of AMS results," *Phys. Rev.*, vol. D88, no. 10, p. 103509, 2013.

[239] D. P. Finkbeiner and N. Weiner, "Exciting Dark Matter and the INTEGRAL/SPI 511 keV signal," *Phys. Rev.*, vol. D76, p. 083519, 2007.

[240] J. Kopp, "Constraints on dark matter annihilation from AMS-02 results," *Phys. Rev.*, vol. D88, p. 076013, 2013.

[241] M. Di Mauro, S. Manconi, and F. Donato, "Detection of a γ-ray halo around Geminga with the Fermi-LAT and implications for the positron flux," 2019.

[242] P. S. B. Dev, D. K. Ghosh, N. Okada, and I. Saha, "Neutrino Mass and Dark Matter in light of recent AMS-02 results," *Phys. Rev.*, vol. D89, p. 095001, 2014.

[243] I. Cholis, D. Hooper, and T. Linden, "Possible Evidence for the Stochastic Acceleration of Secondary Antiprotons by Supernova Remnants," *Phys. Rev.*, vol. D95, no. 12, p. 123007, 2017.

[244] N. Tomassetti and A. Oliva, "Production and acceleration of antinuclei in supernova shockwaves," *Astrophys. J. Lett.*, vol. 844, p. L26, 2017, [Astrophys. J.844,no.2,L26(2017)].

[245] T. R. Slatyer, N. Padmanabhan, and D. P. Finkbeiner, "CMB Constraints on WIMP

Annihilation: Energy Absorption During the Recombination Epoch," *Phys. Rev.*, vol. D80, p. 043526, 2009.

[246] C. Evoli, M. Valdes, A. Ferrara, and N. Yoshida, "Energy deposition by weakly interacting massive particles: a comprehensiv e study," *Mon. Not. Roy. Astron. Soc.*, vol. 422, pp. 420–433, 2012.

[247] M. S. Madhavacheril, N. Sehgal, and T. R. Slatyer, "Current Dark Matter Annihilation Constraints from CMB and Low-Redshift Data," *Phys. Rev.*, vol. D89, p. 103508, 2014.

[248] T. R. Slatyer, "Indirect dark matter signatures in the cosmic dark ages. I. Generalizing the bound on s-wave dark matter annihilation from Planck results," *Phys. Rev.*, vol. D93, no. 2, p. 023527, 2016.

[249] M. Tavakoli, I. Cholis, C. Evoli, and P. Ullio, "Constraints on Dark Matter Annihilations from Diffuse Gamma-Ray Emission in the Galaxy," *JCAP*, vol. 1401, p. 017, 2014.

[250] A. Geringer-Sameth, S. M. Koushiappas, and M. G. Walker, "Comprehensive search for dark matter annihilation in dwarf galaxies," *Phys. Rev.*, vol. D91, no. 8, p. 083535, 2015.

[251] M. Ackermann *et al.*, "Searching for Dark Matter Annihilation from Milky Way Dwarf Spheroidal Galaxies with Six Years of Fermi Large Area Telescope Data," *Phys. Rev. Lett.*, vol. 115, no. 23, p. 231301, 2015.

[252] A. U. Abeysekara *et al.*, "The 2HWC HAWC Observatory Gamma Ray Catalog," *Astrophys. J.*, vol. 843, no. 1, p. 40, 2017.

[253] A. A. Abdo *et al.*, "Milagro Observations of TeV Emission from Galactic Sources in the Fermi Bright Source List," *Astrophys. J.*, vol. 700, pp. L127–L131, 2009, [Erratum: Astrophys. J.703,L185(2009)].

[254] A. Abramowski *et al.*, "Acceleration of petaelectronvolt protons in the Galactic Centre," *Nature*, vol. 531, p. 476, 2016.

[255] N. Vranesevic *et al.*, "Pulsar birthrate from Parkes multi-beam survey," *Astrophys. J.*, vol. 617, pp. L139–L142, 2004.

[256] C.-A. Faucher-Giguere and V. M. Kaspi, "Birth and evolution of isolated radio pulsars," *Astrophys. J.*, vol. 643, pp. 332–355, 2006.

[257] D. R. Lorimer *et al.*, "The Parkes multibeam pulsar survey: VI. Discovery and timing of 142 pulsars and a Galactic population analysis," *Mon. Not. Roy. Astron. Soc.*, vol. 372, pp. 777–800, 2006.

[258] E. F. Keane and M. Kramer, "On the birthrates of Galactic neutron stars," *Mon. Not. Roy. Astron. Soc.*, vol. 391, p. 2009, 2008.

[259] I. Cholis and N. Weiner, "MiXDM: Cosmic Ray Signals from Multiple States of Dark Matter," 2009.

[260] I. Cholis, L. Goodenough, and N. Weiner, "High Energy Positrons and the WMAP Haze from Exciting Dark Matter," *Phys. Rev.*, vol. D79, p. 123505, 2009.

[261] D. R. Lorimer, "The galactic population and birth rate of radio pulsars," 2003, [IAU Symp.218,105(2004)].

[262] I. Yusifov and I. Kucuk, "Revisiting the radial distribution of pulsars in the galaxy," *Astron. Astrophys.*, vol. 422, pp. 545–553, 2004.

[263] R. N. Manchester *et al.*, "The Parkes Multibeam Pulsar Survey. 1. Observing and data analysis systems, discovery and timing of 100 pulsars," *Mon. Not. Roy. Astron. Soc.*, vol. 328, p. 17, 2001.

[264] G. Hobbs, D. R. Lorimer, A. G. Lyne, and M. Kramer, "A Statistical study of 233 pulsar proper motions," *Mon. Not. Roy. Astron. Soc.*, vol. 360, pp. 974–992, 2005.

[265] C. M. Espinoza, A. G. Lyne, and B. W. Stappers, "New long-term braking index measurements for glitching pulsars using a glitch-template method," *Mon. Not. Roy. Astron. Soc.*, vol. 466, no. 1, pp. 147–162, 2017.

[266] F. E. Marshall, L. Guillemot, A. K. Harding, P. Martin, and D. A. Smith, "A New, low Braking Index for the lmc Pulsar B0540–69," *Astrophys. J.*, vol. 827, no. 2, p. L39, 2016.

[267] R. F. Archibald *et al.*, "A High Braking Index for a Pulsar," *Astrophys. J.*, vol. 819, no. 1, p. L16, 2016.

[268] S. Johnston and A. Karastergiou, "Pulsar braking and the P–$\dot{P}$ diagram," *Mon. Not. Roy. Astron. Soc.*, vol. 467, no. 3, pp. 3493–3499, 2017.

[269] R. N. Manchester, G. B. Hobbs, A. Teoh, and M. Hobbs, "The Australia Telescope National Facility pulsar catalogue," *Astron. J.*, vol. 129, p. 1993, 2005.

[270] I. Cholis, D. Hooper, and T. Linden, "A Predictive Analytic Model for the Solar Modulation of Cosmic Rays," *Phys. Rev.*, vol. D93, no. 4, p. 043016, 2016.

[271] L. J. Gleeson and W. I. Axford, "Solar Modulation of Galactic Cosmic Rays," *Astrophys. J.*, vol. 154, p. 1011, 1968.

[272] R. Trotta, G. Jóhannesson, I. V. Moskalenko, T. A. Porter, R. R. d. Austri, and A. W. Strong, "Constraints on cosmic-ray propagation models from a global Bayesian analysis," *Astrophys. J.*, vol. 729, p. 106, 2011.

[273] L. Bergstrom, T. Bringmann, I. Cholis, D. Hooper, and C. Weniger, "New Limits on Dark Matter Annihilation from AMS Cosmic Ray Positron Data," *Phys. Rev. Lett.*, vol. 111, p. 171101, 2013.

[274] A. Ibarra, A. S. Lamperstorfer, and J. Silk, "Dark matter annihilations and decays after the AMS-02 positron measurements," *Phys. Rev.*, vol. D89, no. 6, p. 063539, 2014.

[275] J. Chang *et al.*, "The DArk Matter Particle Explorer mission," *Astropart. Phys.*, vol. 95, pp. 6–24, 2017.

[276] G. Ambrosi *et al.*, "Direct detection of a break in the teraelectronvolt cosmic-ray spectrum of electrons and positrons," *Nature*, vol. 552, pp. 63–66, 2017.

[277] O. Adriani *et al.*, "Energy Spectrum of Cosmic-Ray Electron and Positron from 10

BIBLIOGRAPHY

GeV to 3 TeV Observed with the Calorimetric Electron Telescope on the International Space Station," *Phys. Rev. Lett.*, vol. 119, no. 18, p. 181101, 2017.

Vita

Tanvi Karwal was born in Valsad, India on October 5th, 1993. In 2011, she began a bachelors in Physics Honours at at the University of Delhi, Miranda House College, during which she received the Meera Singla Memorial Award for excellence in Mathematical Physics. Doing summer research with Dr. Subhendra Mohanty at the Physical Research Laboratory, Ahmedabad, she became interested in cosmology. She joined the Department of Physics & Astronomy at Johns Hopkins University in 2014 to continue research in cosmology under the advisement of Prof. Marc Kamionkowski. An enthusiastic teaching assistant, she was awarded the Rowland Prize for Innovation and Excellence in Teaching in 2016. Completing her PhD studies in 2019, she will move to the University of Pennsylvania on a postdoctoral fellowship to continue her research.